Quantitative Post-Processing Techniques for Angiographic Imaging

by

Carson Anthony Hoffman

A dissertation submitted in partial fulfillment of the requirements for the degree of

Doctor of Philosophy (Medical Physics)

at the

UNIVERSITY OF WISCONSIN-MADISON 2020

Date of the final oral examination: 07/27/2020

The dissertation is approved by the following members of the Final Oral Committee:
Oliver Wieben, Professor, Medical Physics
Michael A. Speidel, Associate Professor, Medical Physics
Kevin M. Johnson, Assistant Professor, Medical Physics
Christopher J. Francois, Associate Professor, Radiology
Paul Laeseke, Assistant Professor, Radiology
E. Jason Abel, Surgeon, Urology

Quantitative Post-Processing Techniques for Angiographic Imaging

Carson Anthony Hoffman

Under the supervision of Professor Oliver Wieben At the University of Wisconsin-Madison

Abstract

The vascular system gives life to body as its function is to transport oxygen and nutrients via blood circulation. When the normal function of the vascular system is altered secondary to a myriad of vascular diseases, it can have catastrophic consequences. There are different types of pathologies that can affect the vascular system such as aneurysms, thrombosis, varicose veins, stenosis, and peripheral artery disease, which are encountered the most frequently. In addition to these, cancers can also manipulate the vascular system through angiogenesis, disruption of normal flow, and invasion of vascular networks. Angiographic imaging has become a powerful diagnostic tool that is crucial for identifying vascular abnormalities and tailoring of optimal treatment strategies. Magnetic resonance angiography and computed tomography angiography are the most widely used angiographic imaging techniques, both of which can provide detailed three-dimensional vascular anatomy throughout the body for investigation and diagnosis of vascular pathologies. While functional information, such as blood flow and velocity, can be complimentary to the diagnosis and treatment of vascular diseases, it is less commonly utilized due to additional complexity involved with the acquisition and post processing.

Quantitative angiographic imaging techniques have been developed for ultrasound, x-ray, and magnetic resonance methods. In vivo flow quantification is commonly performed with Doppler ultrasound as it can provide quick and non-invasive hemodynamic parameters at a relatively lower cost. However, analysis with Doppler ultrasound can be limited by vessel depth and a relatively small field of view, leading to lengthy examinations for analysis of complex vascular networks. Quantitative x-ray methods can provide hemodynamic information through the analysis of temporal contrast kinetics of

injected agents. Clinically available software packages can provide indirect quantitative measures related to blood flow, such as time of arrival, time to peak, and area under the curve. It has been shown that direct measures of blood velocity and flow can be computed with x-ray-based techniques, but limitations exist with repeatability and complexity of analysis. Quantitative magnetic resonance imaging techniques can provide meticulous information on functional hemodynamics throughout the body non-invasively. In fact, 4D flow MRI provides time resolved three-dimensional velocity maps over a large imaging volume, allowing for the computation of parameters such as flow, velocity, kinetic energy, and pressure within a vascular network. Majority of the clinically available post processing software packages are focused on the analysis of the aorta, limiting quantitative 4D flow analysis of complex vascular networks.

This body of work explores the development and application of quantitative angiographic tools for 4D flow MRI and 2D-digital subtraction angiography (DSA). A novel quantitative tool was created to calculate blood velocities using time resolved 2D DSA acquisitions in the abdomen. The application of the quantitative DSA tool was used to assess intra-procedural blood velocity changes during transarterial embolization, which is frequently utilized to interrupt blood flow to an organ or lesion, including the treatment of liver tumors. In addition to quantitative DSA, 4D flow MRI was utilized to evaluate blood flow and velocity changes in a porcine liver model before and after transarterial embolization. Beyond the abdominal applications, a cranial 4D flow MRI post processing tool was developed to simplify and automate the analysis steps required for quantitative hemodynamic imaging within the brain, which is important for patients with cognitive diseases. Another area that 4D flow MRI could prove useful was in the realm of renal cell carcinoma to provide quantitative hemodynamic information for presurgical planning with potential implications on patient outcomes. Through rigorous theoretical analysis, phantom studies, and, in vivo testing, strides were taken forward to provide quantitative hemodynamic information that can complement anatomical angiographic imaging.

Acknowledgements

The work completed in this dissertation was only possible due to the constant support from a long list of friends, family, and colleagues.

First off, I would like to thank Dr. Oliver Wieben who was an excellent advisor throughout my graduate school experience. I was lucky enough to meet Oliver during my undergraduate internship with Dr. Rupak Das at the University of Wisconsin Madison in the Radiation Oncology department. From our first chat in the halls of WIMR I was immediately hooked by the amazing research being completed in his lab. I kept in contact with him during the completion of my senior year of undergraduate studies and made sure to get an interview with him during the medical physics graduate school interviews. From this point I had enjoyed different aspects of medical physics but had yet to experience the world of angiographic imaging. During the interview he presented different applications and tools that were commonly used in his group and my mind start spinning with all the endless fun projects. Addition to all the scientific accomplishments, Oliver was always very personable and made graduate school an easy choice for me. It was clear to me that the combination of social and scientific skills made him the perfect advisor for me and I was lucky enough to join his lab. From day one Oliver provided a research environment in which I could explore my own ideas while providing guidance in how to hone my research skills. Over the years he created opportunities for me to collaborate with a variety of different research groups and get experience with many different imaging modalities. He was always willing to chat about new ideas and his depth of research experience always lead to solutions that made the research more impactful. Not only did Oliver help with my academic career, he made sure to balance the workload with social activities and provide outlets for me to create lasting friendships. I will always be grateful for his guidance throughout my graduate studies and look forward to our continued relationship post-graduation.

I would like to thank two people whom without I would not be here, my parents Dave and Leslie Hoffman. Both have been nothing but supportive from day one. They taught me the importance of

balancing a family and work life by always taking the time to be involved in my life. In times where I was extremely busy, they could always find a way to brighten my day even 2000 miles away. I would like to thank them for teaching me how to think outside the box and find creative solutions to problems. In addition to this, anyone who has met me can thank them for my excellent jokes and sense of humor. I would like to thank my grandma Marge Hoffman for teaching me how to live your life to the fullest no matter what age you are. She was a constant presence in my life and helped teach me how to dance, cook, and was ever vigilant on making sure my hair never got out of control. I want to thank both of my sisters, Sierra and McKayla Hoffman, for all the amazing conversations, road trips, and experiences throughout my life. Their continued support and hilarious conversations helped to provide an always enjoyable escape from the technical research world. Even with the variety of travels completed during my graduate studies they made sure to keep in contact and keep our friendship strong. I would like to thank all my extended family for all the great parties and family reunions over the years. Everyone was extremely supportive, and it was always a blast to catch up at the family events.

I would like to thank all my friends for their support during my time in graduate school. Rafael Medero and Karina Lugo always provided a welcomed place to stop on my long walks home. We had tons of great parties filled with laughter along with late nights full of research and brain storming. Christie and Bryan Haddon were my family away from home and provided a place to celebrate holidays when I couldn't make it home. It was an honor to be Christie's Sherpa and walking buddy throughout graduate school and value all the great times we chatted about life and research. Dakota Morgan was always there to explore the city of Madison and celebrate after a long work week. Thanks to him I will continue to be a Michigan State fan as long as they aren't playing against the Badgers. John Hayes was always available to chat about any random question, which I had no shortage of. His enthusiasm, thoroughness, and friendship were invaluable to have present during the completion of my graduate studies. I would like to give a special thanks to Ece Meram who was constantly supportive of my research and would make time to listen to new ideas even at the busiest of times. Her insight for the clinical applications of the work

helped to further improve the quality of my research. She was not only supportive of my academic career but was an excellent friend to have at my side on our many adventures. No matter the activity, eating Babcocks ice cream at the terrace, kayaking in Door County, hiking around the giant sequoias, or exploring the world of Harry Potter, it was always a pleasure to have her there with me. I look forward to our continued academic and personal relationship over the year post graduate studies.

I would like to thank all the past and present Wieben lab members who helped to make my research into the finished product presented in this dissertation. I would like to give my appreciation to the past members Jacob MacDonald, Leonardo Rivera, Mike Loecher, and Eric Schrauben, for passing on their MRI expertise to the spring chicken. I would additionally like to thank the current members of the lab, Phil Corrado, Grant Roberts, Dan Seiter, and Ruiming Chen. Thanks for your feedback on all the random projects I became involved in, lending a helping hand on the experimental studies, exploring the world with me when conferences took us around the globe, and for the great times shared at the terrace relaxing post work. A special thanks to Phil, for bringing his TV so we could watch sports on four different TV's at once and Grant for chilling at the BlueMoon after a long day of research.

Lastly, thank you to all the people who I have met during my time in Madison. I appreciate your contributions to my work and it would not have been possible without the constant support and great input over the past 6 years.

Table of Contents

List of Tables

List of Figures

Chapter 1: Introduction

The first angiographic images were generated using 2D x-ray projections shortly after Roentgen's foundational paper was published (2,3). The potential for medical applications was quickly recognized by many and work was completed to develop 2D angiography into a diagnostic tool(4,5). The majority of angiographic images were acquired with invasive or minimal invasive procedures, with arterial or venous injections respectively, until less invasive techniques were developed utilizing ultrasound (US), magnetic resonance angiography (MRA), and computed tomography angiography (CTA). These new techniques allowed for a smaller risk of patient complications, an increase in diagnostic capabilities, a reduction in cost, and the ability to provide structural information outside of the vascular territories of interest. This led to the application of 3D cross-sectional imaging techniques, such as MRA and CTA, to become the mainstay of diagnostic angiography. The traditional 2D angiographic x-ray imaging techniques could provide real time selective vascular information; thus, it evolved and became a critical imaging modality for intra-procedural use. Digital subtraction angiography (DSA) was developed at the University of Wisconsin Madison and has become a standard imaging technique for many vascular procedures (6–8). As all angiographic imaging modalities continue to develop, they provide additional structural and functional vascular information in the assessment of vascular disease.

Vascular disease encompasses a variety of arterial and venous vessel abnormalities that can affect the normal circulation of blood flow throughout the body. Some of the most prevalent vascular diseases include: stroke, peripheral artery disease, coronary artery disease, artheriosclerosis, thrombus formation, arteriovenous malformation, varicose veins, pulmonary embolism, and critical limb ischemia. The complexity of the arterial and venous vascular network can lead to the development of irregular blood flow, which occurs commonly in the coronary arteries, iliac arteries, renal arteries, circle of Willis, and the aorta. Angiographic imaging techniques are commonly used in the assessment, treatment, and follow

up of patients that have vascular disease complications (9–12). There is continued development to provide structural and functional vascular information throughout the body, while utilizing minimally invasive to non-invasive imaging techniques. MRA and CTA have become the most commonly used angiographic imaging techniques for structural vascular assessment. Functional vascular analysis is possible using doppler ultrasound, which can provide an inexpensive way to non-invasively measure blood velocities and flow. As doppler ultrasound can be limited by operator dependence and imaging depths, alternative functional angiographic methods, using MRI and x-ray based techniques (13,14), have been developed. In addition to quantitative angiographic imaging techniques, flow wires and pressure wires can be used to measure functional hemodynamic information with minimally invasive procedures.

As angiographic imaging techniques continue to evolve, the amount of data being acquired and post-processed is increasing. Methods that have started as 2D imaging techniques have moved to 4D methods, drastically increasing the complexity of data analysis. 4D methods can provide time-resolved imaging volumes, with three spatial and one temporal dimensions. Visualization of vascular anatomy has become a key component for the determination and diagnosis of vascular diseases. Cross-sectional imaging techniques utilizing MRA and CTA can be acquired as 3D or 4D volume data sets; however, they are commonly reconstructed and viewed as 2D slices for diagnosis (15,16). As the majority of medical images are display on 2D screens, techniques that can provide 3D information in a single image, such as volumetric rendering and maximum intensity projection, have been developed. Volume renderings of a cranial arteriovenous malformation imaged with 3D MRA and 3D DSA techniques can be seen in Figure 1-1. As hemodynamic properties (blood flow, velocity, perfusion, pulsatility index, vessel area, etc.) become quantifiable through multidimensional non-invasive imaging techniques, software development is needed to allow for quick and robust analysis of the data. There are plenty of software tools (FDA approved) to help with basic angiographic analysis: vessel diameter, stenosis percentage, area stenosis, etc. However, there is a lack of advanced post processing tools that can provide hemodynamic analysis for vessel networks that can be obtained with the new generation of imaging tools such as 4D

flow and 4D DSA.

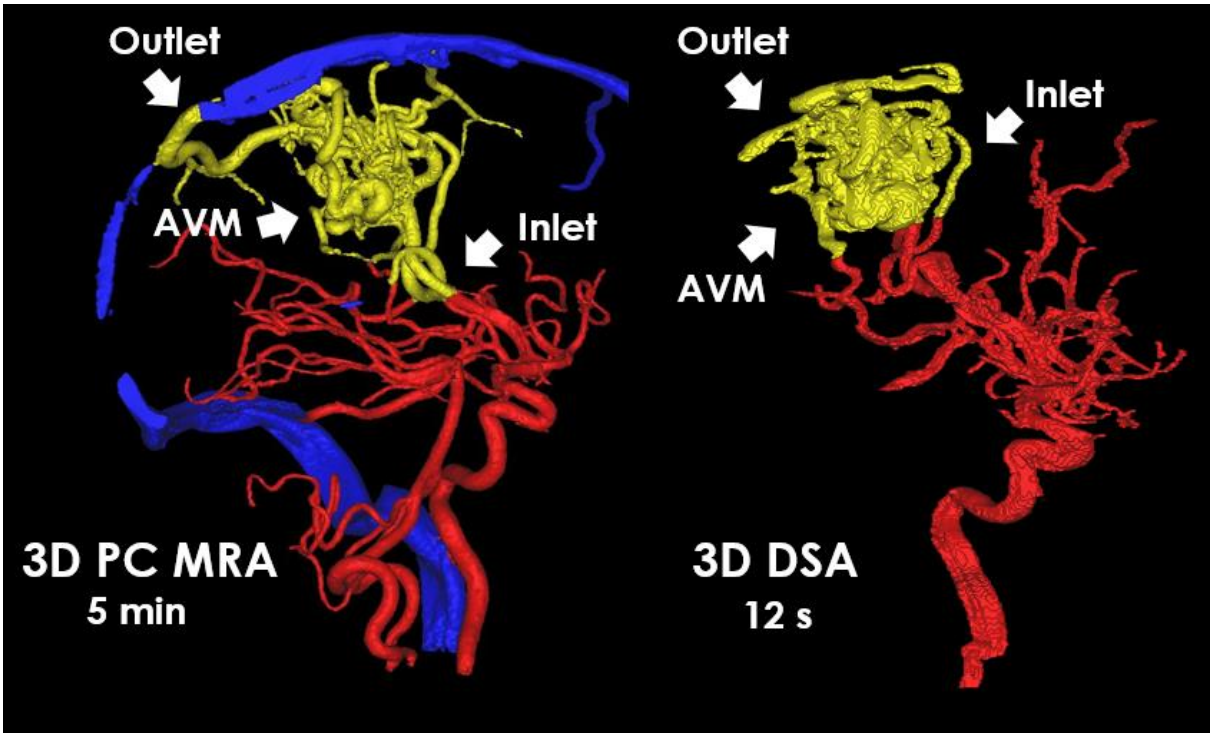

Figure 1-1: 3D vascular displays for phase contrast magnetic resonance angiography (PC MRA) and digital subtraction angiography (DSA) of a patient with an arteriovenous malformation (AVM) in the brain. The arteries (red) and veins (blue) are present in the MRA while only arteries are visible in the DSA. The acquisition time was on the order of seconds while the MRA was completed in a few minutes. The AVM (yellow) inlet and outlet are visible with both angiographic imaging technique.

The purpose of the work completed in this dissertation was the development, implementation, and validation of quantitative post-processing tools for angiographic imaging techniques with the goal to improve diagnostic workflows and capabilities. Specifically, two independent tools were developed to allow quantitative post-processing of 2D digital subtraction angiography (DSA) abdominal images and 4D flow MRI cranial images. The tools were first validated using a controlled experimental setup, in which a flow pump generated realistic pulsatile cardiac waveforms that progressed through 3D printed vascular models. The quantitative DSA tool validation was completed by replicating an arterial catheter injection in a carotid bifurcation model. The image acquisition parameters such as magnification, projection angle, injection rate, and baseline flow rate were tested and compared to a calibrated flow sensor. After validating the 2D DSA tool in a phantom, it was tested in an in vivo animal study for a

variety of abdominal arterial vessel locations (Iliac, Renal, Hepatic, Splenic). Finally, the 2D DSA tool was used to assess intra-procedural changes in relative blood velocity, as a trans-arterial embolization of the left or right hepatic artery was performed. The tool was developed to deliver near-real time quantitative velocity measurements, as the application was designed as a method to quantitatively inform interventional procedural endpoints. The quantitative 4D flow MRI post-processing tool was validated with a realistic arterial vasculature brain phantom. The accuracy of flow and area were compared to established ground truths. The tool was then applied in healthy volunteers using internal consistency of flow and manual segmentation as the standard reference. This tool provided a statistically significant decrease in post processing time need to complete the analysis of a cranial 4D flow MRI. This work was completed with the intention of improving upon current post-processing tools utilized by the Alzheimer's Diseases Research Center, which has processed 1000s of cranial 4D flow cases. The final part of this dissertation applied quantitative 4D flow MRI techniques to the pre-operative assessment of renal cell carcinoma patients. An investigation of arterial renal blood flow asymmetry, inferior vena cava cancer invasion, and collateral vessel development was completed. It is thought that the breadth of quantitative and qualitative information provided by a single 4D flow MRI could aid in surgical planning and may improve patient treatments. The remaining chapters of this dissertation are organized as follows:

Chapter 2: Principles of Magnetic Resonance and X-ray Angiographic Imaging provides an overview of the underlying basics of magnetic resonance and x-ray angiographic imaging. This chapter will focus on the phase contrast (PC) technique for MR and digital subtraction angiography (DSA) for the x-ray modality. First, the mechanisms for signal generation for both MR and x-ray are discussed, with the mention of a few key hardware components. A more in-depth explanation of techniques and principles used specifically for PC MRI are presented with the discussion progressing from 2D to 4D applications. The basics of DSA image generation will be discussed with some of the methods limitations. Finally, advance DSA applications including 4D and quantitative methods will be presented.

Chapter 3: A Technique for 2D DSA Intra-Procedural Blood Velocity Quantitation explores the

feasibility of using quantitative 2D DSA for the assessment of in vivo blood velocities. Phantom experiments and in vivo applications, in a swine model, were used to validate the developed post-processing technique. The phantom experiments varied a variety of imaging parameters and compared quantitative DSA velocities to an external flow probe sensor. The in vivo swine studies compared triplicate DSA velocity measurement with 4D flow MRI velocities. For both the experimental and in vivo studies a strong linear correlation was shown with a slope near unity. This clearly demonstrated the ability to calculate average blood velocities from a 2D DSA. This material was presented as poster presentations at CIRSE 2019 (17), and, SIR 2020 (18), an oral presentation at RSNA 2019 (19), and is under revision for publication in academic radiology.

Chapter 4: Characterizing Hepatic Arterial Velocity Changes from TAE reviews the application of quantitative angiographic imaging techniques before, during and after trans-arterial embolization. 4D flow MRI was used to assess hepatic flow distributions before treatment using second order branches. A pre- and post- TAE flow analysis was completed utilizing 4D flow, which was compared to an invasive doppler wire measurement. Quantitative DSA was used to monitor velocity changes during TAE treatment and was compared to a clinically available parametric processing software. The quantitative techniques were able to detect blood velocity and flow changes in the hepatic vasculature. The work presented in this chapter was presented as a poster presentation at ISMRM 2018 (20), and SIR 2020 (21), an oral presentations at SMRA 2019 (22), and is currently under consideration for publication CVIR.

Chapter 5: Automated Post-Processing of Cranial 4D Flow MRI reviews the development of a 4D flow post-processing tool for quantitative cranial analysis. Validation of the tools ability to assess flow and area was completed in a phantom and in vivo with a healthy human cohort. A new sliding threshold segmentation method was proposed and tested against the currently used k-means segmentation. The tool allowed for strong correlations between reference standards and automated techniques. Additional automation resulted in a robust analysis tool that reduced the post-processing times need for a comprehensive cranial analysis. This material was presented as poster presentations at SMRA 2019 (23),

an oral presentation at SMRA 2019 (24), and is under revision for publication in magnetic resonance in medicine.

Chapter 6: Preoperative 4D Flow Analysis of Renal Cell Carcinoma presents the results from a study that utilized 4D flow MRI (PC VIPR) for the preoperative assessment of renal cell carcinoma (RCC). This work investigated the arterial flow distribution between left and right kidneys in the presence of RCC. An asymmetry was found to be present in all RCC patients while symmetric flow distribution was common for healthy individuals. The RCC invasion in the venous vasculature was assessed in relation to collateral lumbar flow enhancement. The arterial to venous flow ratio was used as a metric for quantitatively grouping patients and seemed to be related to venous invasion. The material in this chapter was presented in poster presentations at GRC 2016 (25), GRC 2018 (26), and SMRA 2016 (27), and as a talk at SMRA 2018 (28).

Chapter 7: Summary and Recommendations will discuss the novelty of the research presented throughout this dissertation. This will be followed with recommendation for potential future work that could be completed to build upon the presented work. The presented ideas will be relevant to quantitative angiographic imaging that utilizes x-ray and MR techniques.

Chapter 2: Principles of Magnetic Resonance and X-ray Angiographic Imaging

This chapter presents a brief overview of the basic principles related to magnetic resonance and x-ray angiographic imaging techniques. It is meant to introduce provide a basic introduction into how signals are generated and acquired in each modality. For a more comprehensive introduction, the reader is referred to the following resources (16,29–33). It then further explores the use of these modalities specifically for angiographic applications. Next a range of qualitative and quantitative imaging techniques will be discussed, all of which allow for hemodynamic assessment throughout the body, from minimally-invasive to non-invasive procedures.

2.1 Magnetic Resonance Imaging

2.1.1 Spin and Net Magnetization

Atomic and subatomic particles such as protons, neutrons, and electrons possess a fundamental property known as spin or spin angular momentum. Spin is a quantized variable that is measured in positive or negative full or half-integer form and is the property that allows a particle to interact with magnetic fields. Due to the Heisenberg uncertainty principle, we cannot know the exact direction of a particle's spin but we instead measure limited properties such as angular momentum, giving insight into the number of spin states for a nucleus. The number of spin states is calculated by multiplying the spin by 2 and adding 1. For a Hydrogen nucleus, this leads to the development of 2 spin states, typically referred to as spin-up (+1/2) or spin-down (-1/2). For all elements that have a non-zero spin, a magnetic dipole moment is generated and magnetic resonance can occur. A constant variable that relates the spin to magnetic moment is known as the gyromagnetic ratio (γ) and is often given in MHz/T. Hydrogen, the most commonly imaged nucleus, has a γ = 42.58 MHz/T. When there is no magnetic field present the spin state energy differences in a material are unobservable. However, in the application of an external magnetic field (B_0), the energy difference in spin states can be measured and is a function of magnetic field strength

given by the Zeeman equation.

$$\Delta E = \gamma \hbar B_0 \quad \text{Eq 2.1}$$

Where ɣ is the gyromagnetic ratio for the nucleus of interest (H = 42.58 MHz/T), ħ is the reduced Planck's constant ($1.055 * 10^{-34}$ J·s), and B_0 is the external magnetic field (T). The presence of an external magnetic field causes a torque to be applied to the nucleus's magnetic moment, which tries to align it with the main magnetic field. Due to constraints of quantum mechanics, the expectation behavior of the spin angular momentum vector has a continuous torque applied to it and will precess about the external magnetic field's direction. The rate of precession of the magnetic moment is known as the Larmor frequency. Relating Eq 2.1 to the Planck relation, the Larmor frequency (34) can be derived as a function of ɣ and B_0.

$$\Delta E = \hbar\omega \text{ (Planck relation)}$$

$$\omega = \gamma B_0 \text{ (Larmor Frequency)} \quad \text{Eq 2.2}$$

Eq 2.2 equation shows that the precession of a specific nuclear magnetic moment is proportional to the applied magnetic field. It can also be shown that when a magnetic field is applied, there is a preference for spin states to be aligned with the field (spin-up) rather than against it (spin-down). At body temperature in a B_0 field equal to 1.5T, this leads to about 4 extra spins out of a million to be aligned in the spin-up direction. The small preference toward the spin-up state gives a vector sum, exactly aligned with B_0, known as the net magnetization (M_0) which is the measurable signal that is collected to generate MRI images. A simplistic animation of how the M_0 is generated can be seen in Figure 2-1. M_0 can be calculated using the following equation:

$$M_0 = \frac{\rho \gamma^2 h^2 B_0}{4 K_b T} \quad \text{Eq 2.3}$$

where ρ is proton density, K_b is the Boltzmann constant (1.38×10^{-23}J/K), and T is temperature (K). This leads to a signal of approximately 20 μT for an average human head. The M_0 signal cannot be measured when aligned with the main magnetic field and requires it to be tipped to the transverse plan prior to being

recorded. To tip the M_0 away from the B_0 field direction, a radiofrequency (RF) pulse is applied at the Larmor frequency. The application of an RF pulse creates a magnetic field that is perpendicular to B_0 and oscillating at the Larmor frequency. This is known as the B_1 field and, in a rotating reference frame matched to the Larmor frequency, appears as a static magnetic field perpendicular to B_0. The M_0 will continue to be tipped for the duration of RF application, with the tip angle (α) calculated as follows.

$$\alpha = \gamma B_1 t_{rf} \qquad \text{Eq 2.4}$$

where α is the final tip angle, B_1 is the strength of the RF pulse being applied, and t_{rf} is the time of RF pulse application. During the RF application, M_0 spirals away from the B_0 field direction and towards the transverse plane. Once the M_0 vector has been rotated away from the B_0 direction, it can be measured by detecting voltage changes induced in coils perpendicular to the B_0 field (30). The tipping of M_0 into the transverse plane, through B_1 application, can be seen in the stationary and rotating reference frames in Figure 2-2.

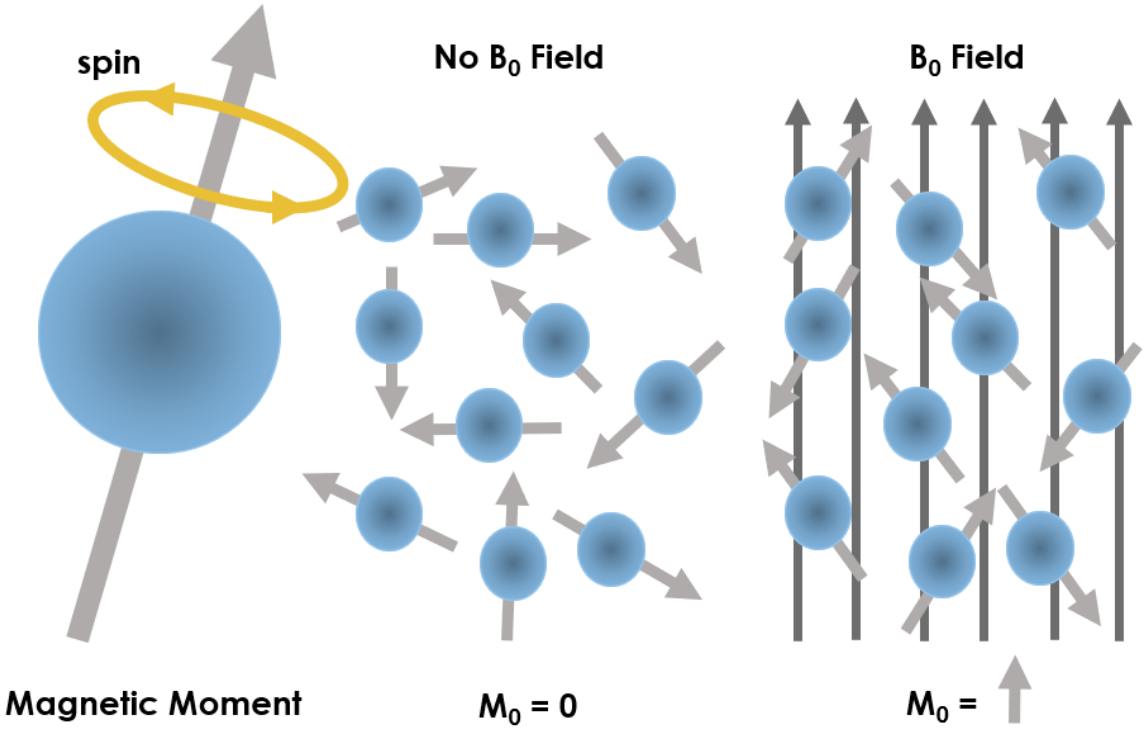

Figure 2-1: In the presence of a magnetic field magnetic moments align with or against the main magnetic field direction. There is a slight preference to align with the main field direction creating a net magnetization vector (M_0). The net magnetization vector is used to generate the signal which is acquired for MRI image generation. The representation of spins in the B_0 field is exaggerated to show a M_0 is generated. In reality there is only slight preference which is visually harder to represent. A spin that is shown as neither up nor down is a visual representation of a spin that lives in a superposition of the up and down states

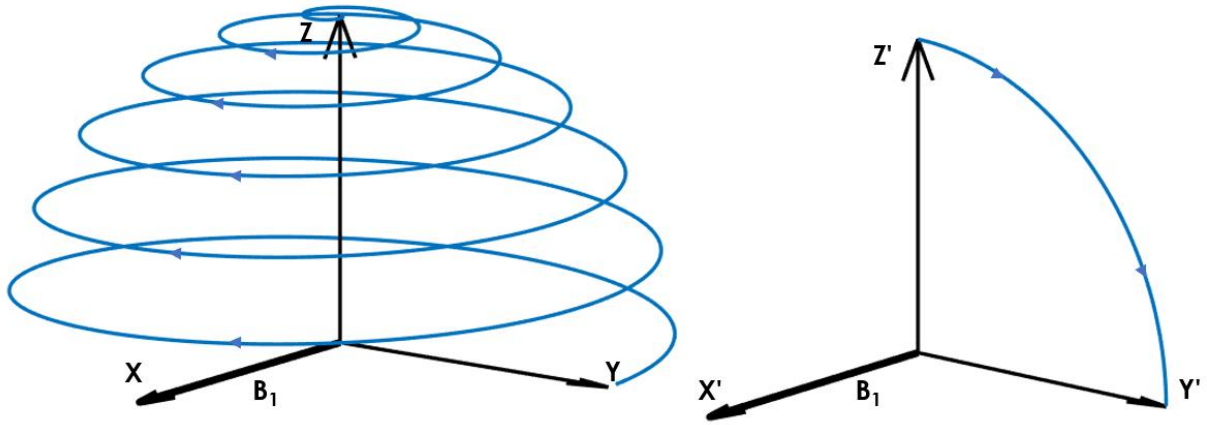

Figure 2-2: The net magnetization is tipped toward the transverse plane as an orthogonal magnetic field is applied (B_1). As the magnetization vector is tipped, it continues to precess about the main magnetic field. This results as a spiral path (left) or a tip occurring along a single direction for a rotating reference frame at the Larmor frequency (right).

2.1.2 Signal Decay and Relaxation

Immediately following the net magnetization tipping, interactions will occur between protons and their environment which will lead to transverse and longitudinal relaxation. It is through these processes that our image contrast in MRI is derived. Longitudinal relaxation, also known as T1 relaxation, is the process that causes the net magnetization to regrow in the B_0 direction until it is equal to the initial M_0 value. Felix Bloch modeled this idea using a simple exponential formula:

$$M_z(t) = M_0(1 - e^{-t/T1}) \qquad \text{Eq 2.5}$$

where M_0 is the initial net magnetization, t is the time point immediately following RF pulse, and T1 is the time required for $M_z(t)$ to reach approximately 63% its max value. T1 values can range from a few tenths of a second up to multiple seconds. Throughout the process of longitudinal relaxation, energy from the spins is transferred into the external environment as more and more spins return to a lower energy state. Transverse relaxation, also known as T2 relaxation, is the process in which the transverse magnetization decrease due to spin components dephasing. This process was also described by Felix Bloch and was found to follow a simple exponential decay:

$$M_{xy}(t) = M_0(e^{-t/T2}) \qquad \text{Eq 2.6}$$

where T2 is the time required for $M_{xy}(t)$ to decay to approximately 37% of its initial value. The transverse magnetization (M_{xy}) will precess about the B_0 field direction (in the transverse plane) and will induce a current in receiver coils, in turn, generating the MR signal. The transverse signal will decay away as the magnetic moments begin to interact with neighboring protons. Each proton resides in a slightly different chemical environment and thus experiences a slightly different magnetic field. The variations in magnetic field cause the precessional frequencies to vary and leads to a decrease in phase coherence. The decrease in phase coherence can arise from either intrinsic or extrinsic field inhomogeneities. This process does not result in a loss of energy and occurs simultaneously with longitudinal relaxation. The application of a 180 degree RF pulse (spin echo) or a refocusing gradient (gradient echo) are used to generate an echo that will

be acquired as the MRI signal. The echo represents the refocusing of spins that have lost their phase coherence. T1 relaxation will always be larger than T2 relaxation as longitudinal losses will affect phase coherence but not vice versa. An example plot of both T1 and T2 relaxation over time can be found in Figure 2-3.

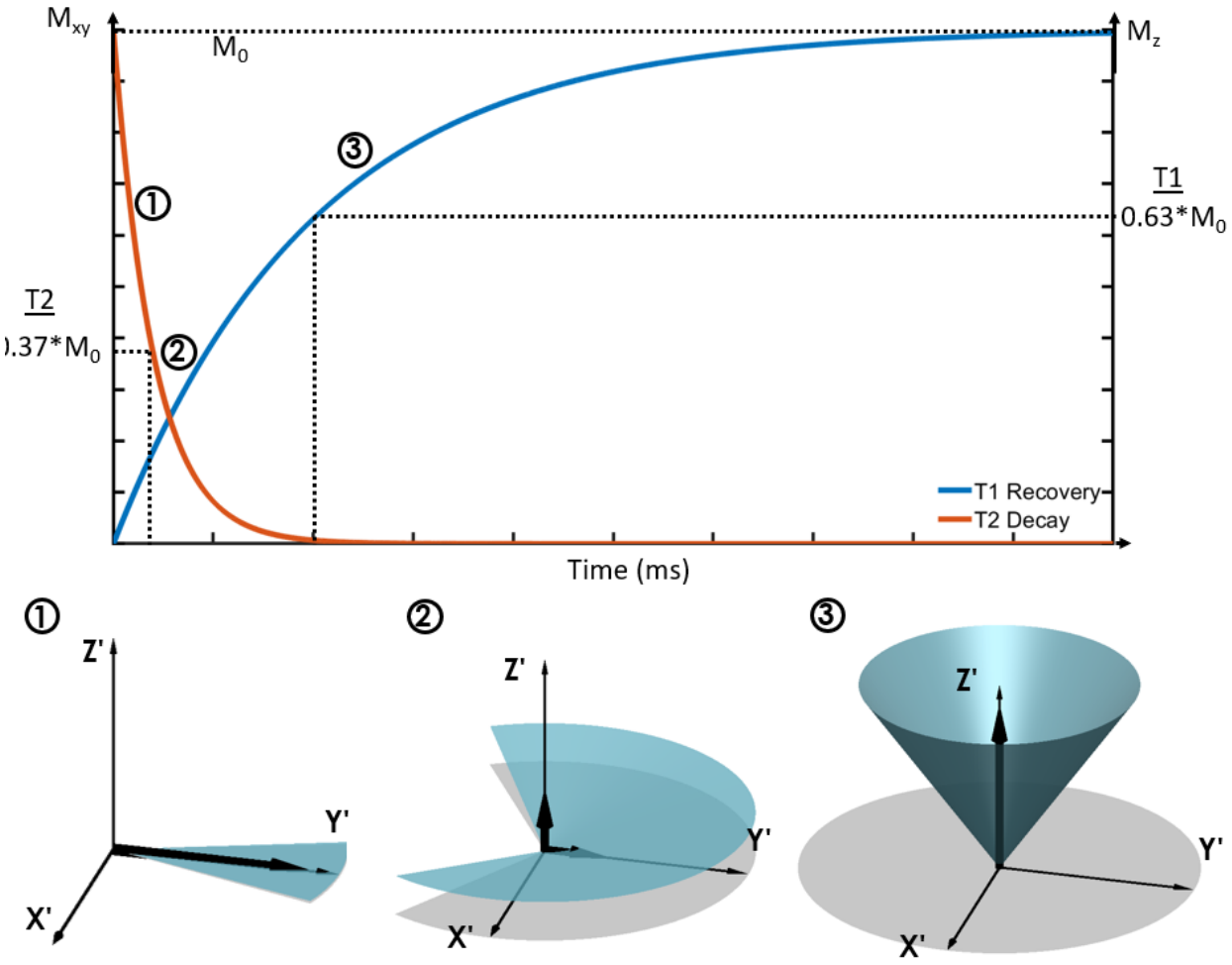

Figure 2-3: T1 and T2 relaxation occur simultaneously with T2 being shorter than T1. T1 relaxation is related to the regrowth of the net magnetization vector while the T2 relaxation is associated with the signal dephasing in the transverse plane. 1) A short amount of time has passed resulting in primarily T2 signal effects. 2) Both T1 and T2 effects are present with magnetization vectors in the transverse plane and along the main magnetic field axis. 3) The transverse signal is completely out of phase, but signal regrowth is still possible showing primarily T1 effects.

MRI is known for its ability to provide a variety of different contrast mechanisms for image generation as well as its superior detail of soft tissues. The contrast present in an MRI image depends

upon T1 relaxation, T2 relaxation and proton density (PD) of the tissue, along with the selected imaging parameters. Two of the most important image parameters that will directly affect image contrast are repetition time (TR) and echo time (TE). TR is the time between the initial signal excitation and the corresponding subsequent signal excitation. TE is the time between initial RF pulse application and the signal echo. A basic gradient-echo pulse sequence can be viewed in Figure 2-4. Multiple excitations are needed to acquire enough information to produce a complete image. By selecting these parameters in specific combinations, different contrasts can be achieved for a single imaging slice. As previously mentioned, the T1 and T2 relaxation processes are occurring simultaneously, but by adjusting TR and TE times, one can reduce the effects of each process in an image. An example of a T1-, T2-, and PD-weighted images of the brain are seen in Figure 2-5.

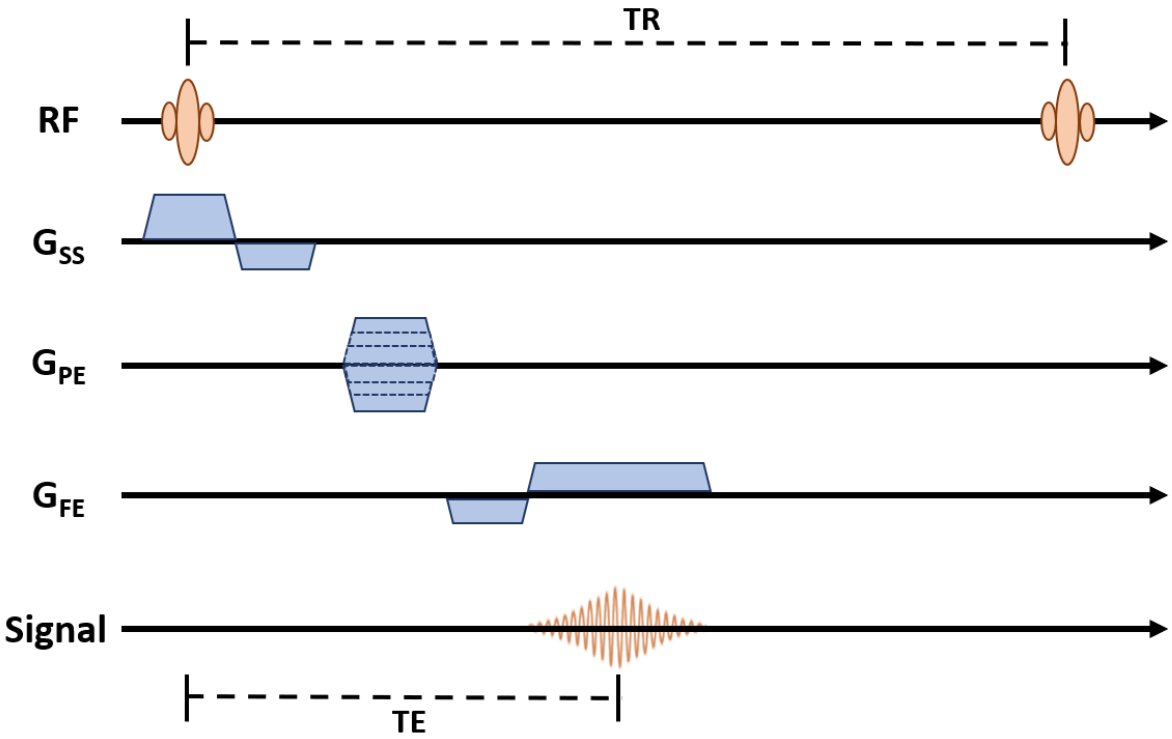

Figure 2-4: A basic gradient-echo sequence with amplitude represented as the vertical axis and time on the horizontal axis. The first line is the radiofrequency (RF) pulse used to rotate the spins into the transverse plane. The slice selective gradient (G_{SS}) is applied simultaneously with the RF pulse to restrict the spin excitation to a specific slice or slab. The phase (G_{PE}) and frequency (G_{FE}) are encoded by applying gradients in the transverse plane. The final line represented the acquired signal.

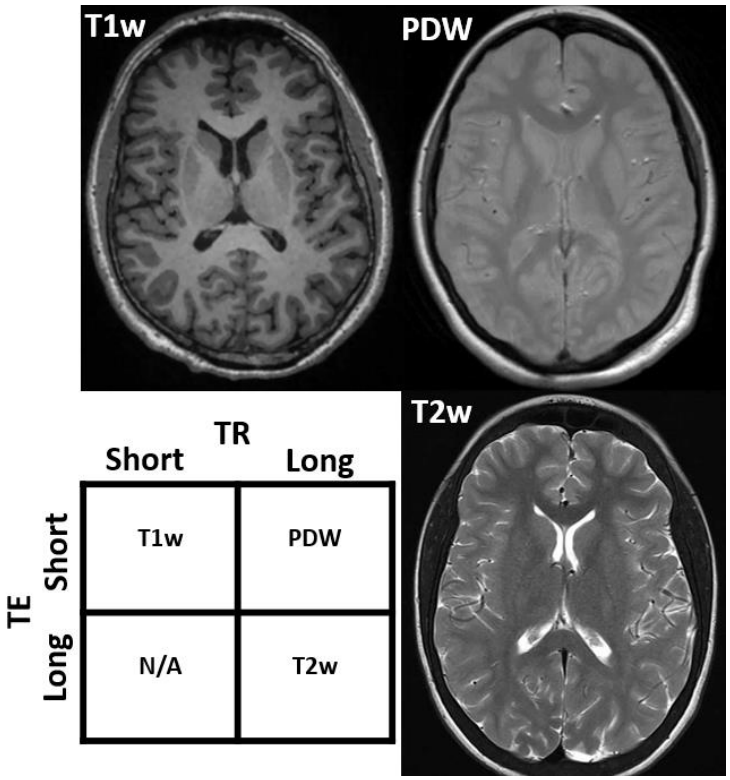

Figure 2-5: Different types of image contrast can be created by altering TR and TE. Here, an axial cranial slice was imaged with T1, T2, and proton density (PDW) weighting. A selection of a short TR and a long TE is not used for image contrast.

2.2 X-ray Imaging

2.2.1 Photon Generation

X-ray imaging uses the transmission of high energy photons, known as x-rays, through the human body to create diagnostic images. A commonly utilized technique to produces x-rays involves accelerating electrons to high speeds and bombarding a metal target inside a vacuum tube. The element that produces the fast-moving electrons is known as the cathode and the metal target, typically made of tungsten, is known as the anode. A simple diagram of some of the key components used in x-ray production can be viewed in Figure 2-6 A). Two different types of x-rays are produced through this technique, known as bremsstrahlung and characteristic x-rays. Bremsstrahlung, or breaking radiation, occurs due to the interaction between the high-energy electron and a nucleus. As the high-energy electron passes by a nucleus it can experience a sudden deflection (deceleration) causing part or all its energy to be converted

to electromagnetic radiation (x-rays). This interaction is predicted by Maxwell's general theory of electromagnetic radiation, which states that any accelerating (or decelerating) charged particle will produce electromagnetic radiation, in this case x-rays. An example of bremsstrahlung production can be viewed in Figure 2-6 B). Because a single electron can undergo multiple bremsstrahlung interactions and the electron may lose a whole range of energies, a continuous range of x-ray energies are produced through this process. The energy loss from the electron per atom depends upon the square of the atomic number (Z) of the target element (tungsten Z = 74). The overall efficiency of x-ray production depends upon both the atomic number of the target material and the electron energy:

$$\text{Efficiency x-ray production} = 9x10^{-10}\ Z \cdot V \qquad \text{Eq 2.7}$$

where Z is the atomic number and V is the tube voltage in units of volts (35,36). For tungsten at an energy of 100kV, the efficiency is <1%, resulting in the remaining 99% of energy being deposited as heat. This high level of heat deposition into the anode is dealt with by rotating the target, using materials with high heat conductivity, and housing cooling oil.

Characteristic x-ray production occurs from a collision between a high energy electron and orbital electron, in which the orbital electron is ejected from a target atom. The electron ejection causes the atom to become ionized and leaves one electron shell with a vacancy. An outer orbital electron can fall into the vacant electron's spot and, in doing so, will release energy as electromagnetic radiation (characteristic x-rays). As the energy difference between electron shells is discrete, characteristic x-rays are emitted at specific values depending on the atomic number of the target and which electron shells are involved in the ejection and replacement process. For this process to occur, the incoming electron must have an energy larger than the ejected electron's binding energy. After the collision, the excess energy from the primary electron is imparted as kinetic energy to both the primary electron and ejected electron. An example of characteristic x-ray production can be view in Figure 2-6 B).

Due to both x-ray generating process occurring in the target material, the final x-ray spectrum is heterogeneous in energy. There is a continuous distribution provided by the bremsstrahlung interactions

and discrete peaks associated with the characteristic x-ray energies. The produced x-ray spectrum is filtered, primarily absorbing lower energy x-rays, to create a "hardened" x-ray beam that is enriched with higher-energy photons. By increasing filtration, the average energy of the beam and penetrating power increases, with the drawback of decreasing the total beam intensity. Optimal imaging intensities are created by selecting the beam filtration and x-ray tube parameters (voltage, filament current, tube current, exposure time) best suited for specific imaging applications.

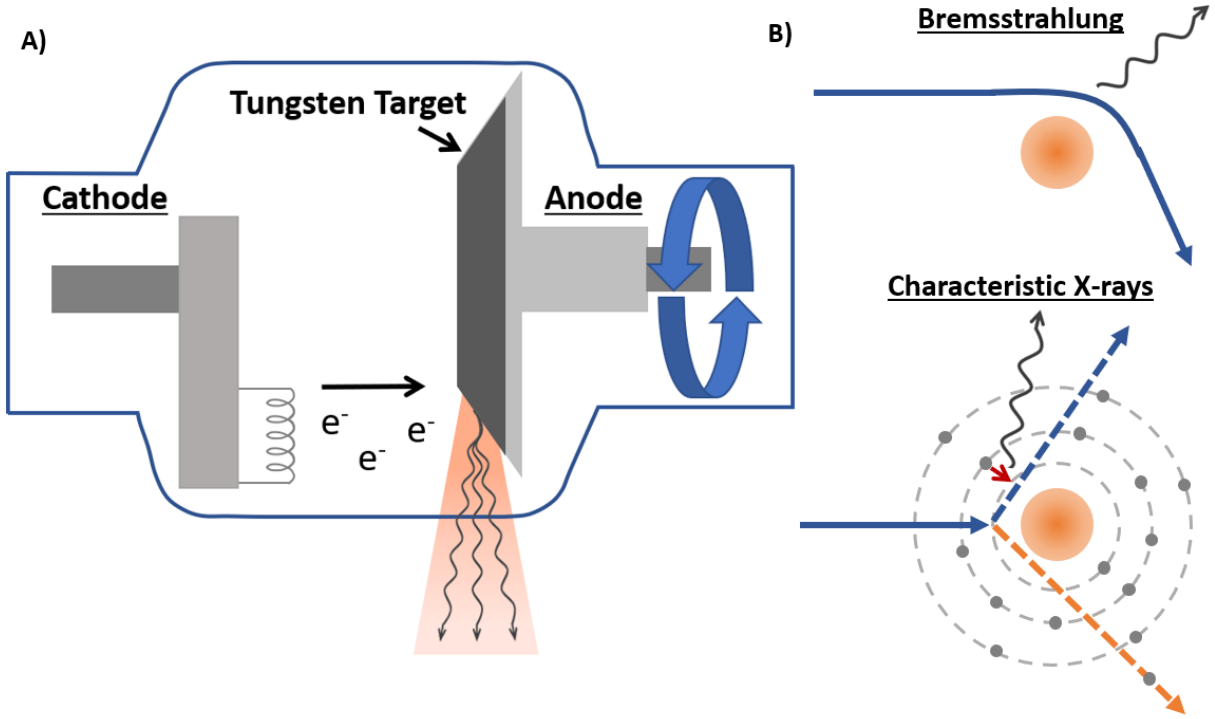

Figure 2-6: A) X-ray generation for diagnostic imaging is commonly completed by accelerating electrons at high energies toward a metal target. A cathode element generates the electrons while a rotating anode is the metal target. B) X-rays are produced by the Bremsstrahlung and characteristic x-ray processes. Bremsstrahlung produces a range of x-ray energies while characteristic x-rays are produced as discrete energy levels. This results in a heterogenous x-ray energy output with peaks at the characteristic x-ray energies.

2.2.2 Photon Interactions

Radiographic images are created by positioning a patient between an x-ray source and a detector. As the x-rays travel through the patient, they are absorbed at different rates depending upon local tissue properties. From the initial x-ray beam, a small number of photons traverse entirely through the patient

unattenuated and it is these x-rays that are captured to generate our image. These unattenuated photons travel to the image detector which are recorded in the form of a two-dimensional radiographic projection image. The signal intensities in this image represent the degree of absorption of x-rays along the photon path to the detector. For instance, a denser material will result in a higher absorption of x-rays and will lead to a lower signal intensity in the image. A simple radiographic setup with an example of how different tissues can change image intensity is shown in Figure 2-7.

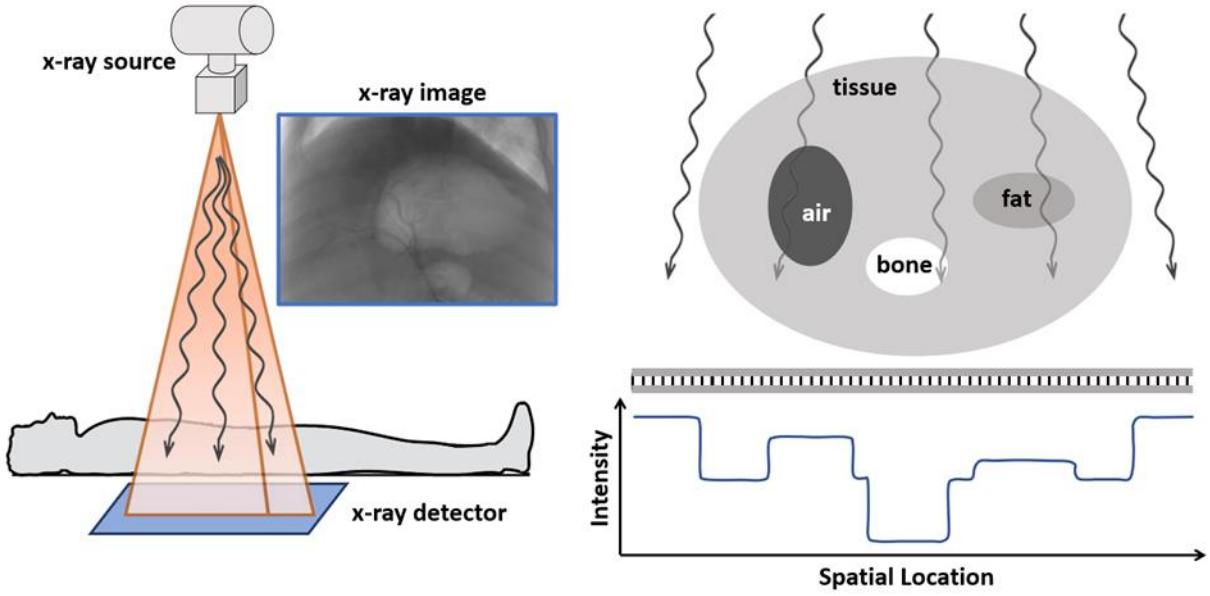

Figure 2-7: Typical radiographic imaging is completed by positioning a patient between an x-ray source and a detector. The resulting image intensities represent the degree of absorption of x-rays as the initial beam passes through the patient. Denser materials, such as bone, will absorb more x-rays and will appear dark while air, which is less absorptive, will appear bright.

There are four major ways in which x-rays can interact with matter: Rayleigh scattering, Compton scattering, photoelectric absorption, and pair production. The first three methods can occur for the typical diagnostic imaging energy range (~20-150 keV). Rayleigh scattering involves an x-ray interacting with the whole atom and then being emitted by the atom with the same energy but at a slightly different angle. This occurs mainly for the lower energy x-ray ranges (<30 keV) and accounts for approximately 10% of all the x-ray interactions (29). Compton scattering is the predominant interaction process for x-rays in soft tissue within the diagnostic imaging range. This process involves an x-ray delivering energy to eject an

electron from an atom, typically valence shell, producing a free electron and a scattered photon. The energy of the scattered photon is equal to the energy of the incident x-ray minus the electron's kinetic and binding energy. As the initial x-ray's energy increases, the scattering angles of the electron and scattered photon being to decrease. While increasing photon energy results in decreased scattering angles, this also results in higher energy photons. For photoelectric absorption, the incoming x-ray is completely absorbed by an ejected electron, with its kinetic energy being equal to the incoming x-ray minus the electrons binding energy. The last method of interaction is pair production, however, this interaction requires a minimum energy of 1.022 MeV and will not be considered in the following discussion because its minimum energy is well outside of the typical diagnostic energy range. Each of these processes can result in the attenuation of an x-ray beam as it travels through a material. The fraction of photons removed for a monoenergetic beam of x-rays per unit thickness of a material, due to all the x-ray interaction processes, is known as the linear attenuation coefficient (μ). No matter the thickness of a material, an exponential relationship exists (Eq. 2.8) between the number of incoming x-rays and the number of unattenuated x-rays:

$$N = N_0 e^{-\mu x} \qquad \text{Eq 2.8}$$

where N is the expectation number of unattenuated x-rays, N_0 is the expectation number of incoming x-rays, μ is the linear attenuation coefficient (cm^{-1}), and x is the material thickness (cm). A related metric is the mass attenuation coefficient, which can be computed by dividing the linear attenuation coefficient by the material density (Eq 2.9) which removes dependence on a material's phase (state of matter). This results in the equation changing to:

$$N = N_0 e^{-(\mu/\rho)\rho x} \qquad \text{Eq 2.9}$$

where N is the expectation number of unattenuated x-rays, N_0 is the expectation number of incoming x-rays, μ/ρ is the mass attenuation coefficient (cm^2/g), ρ is the material density(g/cm^3), and x is material thickness (cm). All of the various contrasts present in radiographic images are directly related to the variety of tissues present in the human, each with different attenuation coefficients and thicknesses.

2.2.3 Geometric Distortion

When interpreting a radiographic image, it is important to understand that a 2D image is being created by projecting through a 3D object. This is especially important when the x-ray source used for image generation is divergent, creating a fan-like beam, which can lead to geometric distortions. Two common geometrical distortions can be caused by an imaged object's position and shape. For example, an objects magnification in the final 2D image, is dependent upon its spatial location between the source and detector. As the object is moved closer toward the x-ray source the magnification of the object in the final image will increase. This magnification can be calculated by dividing the source to detector distance by the source to object distance. In addition to magnification, object foreshortening can occur in non-symmetrical objects. The level of foreshortening that occurs is related to the object shape and relation to the x-ray source and is crucial when looking at irregularly shaped objects with non-optimal projection angles. An example of object magnification and foreshortening can be seen in Figure 2-8.

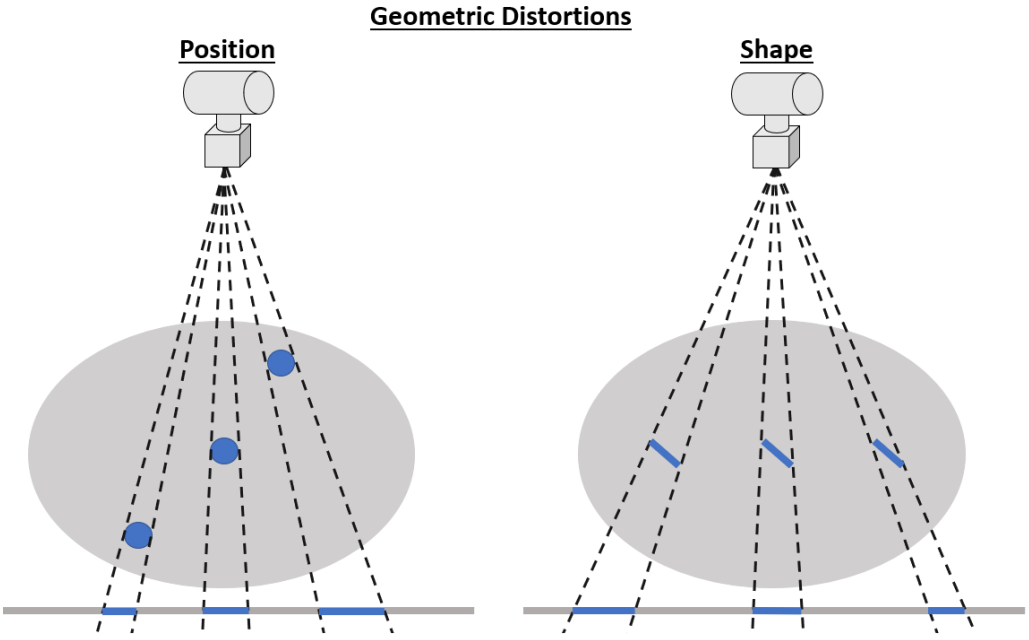

Figure 2-8: Geometric distortions in the final projection image can result from object location (relative to the x-ray source) and object shape. For diagnostic imaging, a point source is used, which leads to a divergent x-ray beam. Magnification will occur as an objects position is moved closer to the x-ray source. Object foreshortening can occur depending on the imaged object's shape and axial location relative to the x-ray source.

2.3 Angiographic Imaging

Angiography is a medical imaging technique that allows for the assessment of in vivo vasculature throughout the human body. Currently, angiographic images are acquired through the application of x-ray or magnetic resonance-based techniques. Computed tomography angiography (CTA), digital subtraction angiography (DSA), and magnetic resonance angiography (MRA) are the most common angiographic imaging techniques and are shown in Figure 2-9. Vascular images can be acquired in 2D, 3D, or 4D (time-resolved 3D) formats by each imaging modality. Angiograms provide important structural information about human vasculature that can be critical for the diagnostic assessment and treatment of vascular diseases. In addition to providing detailed vascular maps, angiographic imaging can be utilized to investigate quantitative hemodynamic parameters, further strengthening the potential benefits of utilizing angiographic imaging for the assessment of vascular disease states. Below, details on Phase Contrast MRA and DSA are provided as they played a major role in the work related to this thesis.

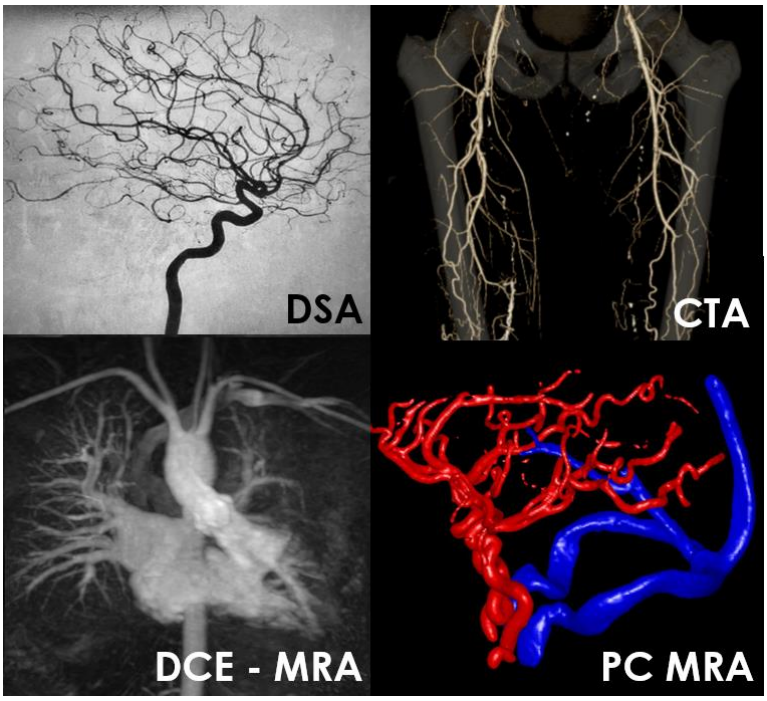

Figure 2-9: Angiographic imaging is routinely used to provide details about in vivo vascular structures throughout the body. The most commonly applied angiographic techniques include digital subtraction angiography (DSA), computed tomography angiography (CTA), and magnetic resonance angiography (MRA). DCE – Dynamic Contrast Enhanced; PC – Phase Contrast

2.4 Phase Contrast MRI

While several other MRA techniques are widely used in clinical practice, time-of-flight (37), and contrast-enhanced methods (38), the remainder of this section will focus specifically on phase contrast (39,40). All MRI images are acquired with the application of magnetic field gradients in specific combinations to spatially encode an image; the three directions for gradient application include the slice selection, frequency encoding, and phase encoding. The acquired signal is complex containing both magnitude and phase information. Typically, the phase information is discarded and the magnitude image is used for clinical diagnosis. However, in phase contrast (PC) imaging, the phase content of the complex image is used in the creation of the PC angiogram. It is known that in the presence of a magnetic field gradient, spins will acquire a phase shift that is proportional to the magnetic field strength. For the majority of MRI sequences, care is taken to use the phase information to spatially encode a single direction while minimizing the phase differences from the frequency and slice selection gradients. This works well for stationary tissues, but in the presence of motion, the acquired phase is dependent upon the velocity of the moving spin. The phase shift from a spin in the presence of a gradient can be determined with the following equation:

$$\Delta\omega(r,t) = \gamma\Delta B + \gamma \mathbf{r}(t)\mathbf{G}(t) \qquad \text{Eq 2.10}$$

where $\Delta\omega$ is the phase shift, γ is the gyromagnetic ratio, ΔB is local field inhomogeneities, $\mathbf{r}(t)$ is the time-dependent spatial location of the spin, and $\mathbf{G}(t)$ is the time-dependent applied magnetic field gradient. For the total phase accrual of a spin from initial excitation time to the echo time, Eq 2.10 must be integrated:

$$\varphi(r,t) = \int_0^{TE} \omega(r,t)dt = \int_0^{TE} \gamma\Delta B dt + \int_0^{TE} \gamma \mathbf{r}(t)\mathbf{G}(t)dt \qquad \text{Eq 2.11}$$

The first term in the equation represents the background phase, φ_0, while the second term describes the spatial and temporal dependent phase accrual. By performing a Taylor series expansion of the spatial $r(t)$ term and substituting into Eq 2.11 we get the following:

$$\varphi(r,t) = \varphi_0 + \gamma r_0 \int_0^{TE} G(t)dt + \gamma v \int_0^{TE} G(t)t dt + \cdots \qquad \text{Eq 2.12}$$

Gradient Moments M_0 M_1

where r_0 is the position along the gradient for a stationary spin and v is the velocity of a moving spin along the gradient direction. There are higher-order terms, such as acceleration and jerk, but they are not considered for most phase contrast acquisitions. Using the third term of Eq 2.12 we can show that for a moving spin, its constant velocity is proportional to its phase shift:

$$v = \frac{\varphi_{moving}}{\gamma M_1} \quad \text{Eq. 2.13}$$

PC MRI takes advantage of this motion sensitivity to encode velocity into the phase of moving spins while leaving stationary spins with a net phase of zero. Eq 2.13 then allows the acquired PC phase to be converted to velocity, a quantitative metric that can be utilized for hemodynamic analysis.

Bipolar gradients are typically utilized in PC MRI, prior to signal acquisition, to generate a non-zero first moment when encoding velocities for moving spins. An example bipolar gradient application, with its associated phase changes on moving and stationary spins, can be viewed in Figure 2-10. The size of the initial gradient is equal to the second inverse gradient, causing a net phase shift for moving spins while no net phase accrual for stationary spins. In the acquisition of an MRI signal, there are unavoidable additional background phase offsets caused by eddy currents, Maxwell term effects, RF saturation, hardware imperfections, and off-resonance effects, to name a few. To remove some of the additional background phase from the motion-induced phase, a second acquisition is completed using a flow compensated acquisition or by applying the same strength gradients but with opposite polarity while keeping all parameters the same (41). It is assumed the background phase are constant between the two acquisitions, thus, when a subtraction between the acquisitions is completed, only motion-induced phase remains. The difference in the first moment gradient, ΔM_1, determines the range of velocities that can be correctly encoded, which is commonly referred to as Venc. Venc is an input imaging parameter that defines the maximum and minimum velocities to a phase shift of π and $-\pi$, with the sign signifying the direction of velocity. Thus, all correctly encoded velocity values present in a phase-encoded image exist between -Venc and Venc. The difference of the first moments can be described as:

$$\Delta M_1 = \frac{\pi}{\gamma \mathrm{Venc}} \qquad \text{Eq 2.14}$$

By substituting Eq 2.14 into Eq 2.13, a voxel's velocity can be computed as a function of phase and Venc:

$$\mathrm{v} = \frac{\varphi_{vox}}{\pi} V_{enc} \qquad \text{Eq 2.15}$$

This allows for the generation of in vivo spatially encoded velocity maps. It should be noted that care needs to be taken in selecting the correct Venc prior to acquisition. If it is set too high, the signal-to-noise ratio of the image will suffer and the ability to distinguish velocities will be diminished. However, if the Venc is set too low, then velocity aliasing may occur causing velocities outside of the upper and lower Venc limits to be misrepresented.

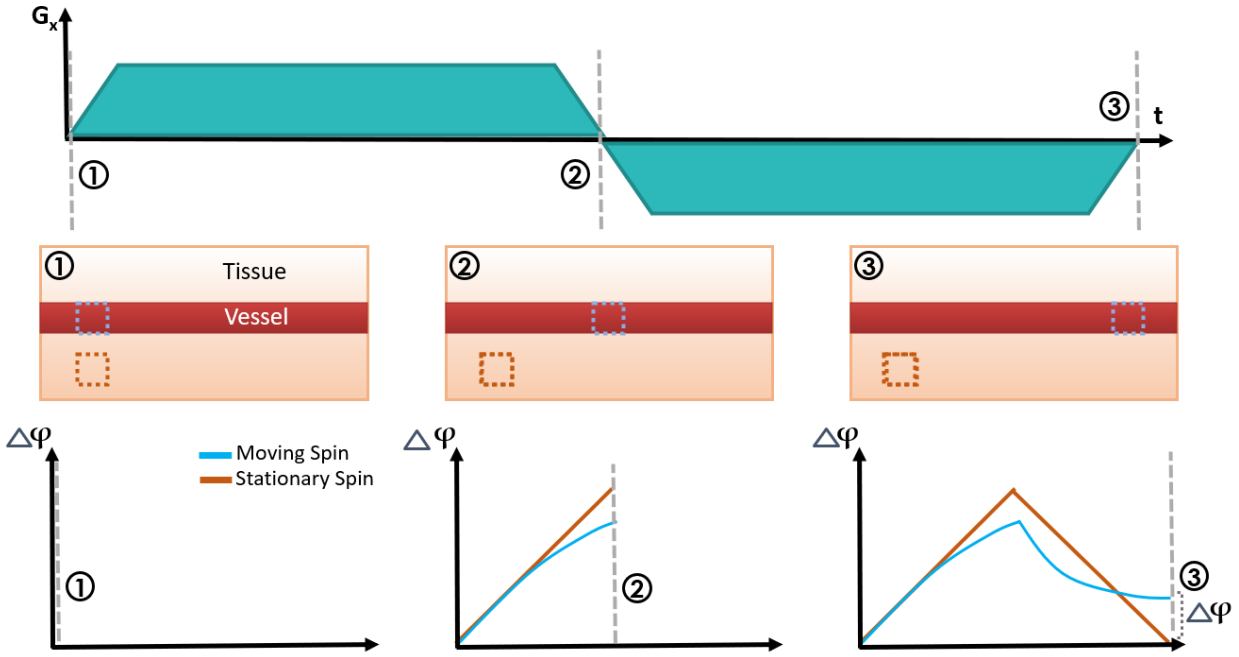

Figure 2-10: The application of bipolar gradients is used for encoding the velocity of moving spins into image phase (blue) while nulling phase for stationary spins (orange). Phase is linearly encoded as a spin moves with a constant velocity and will result in a final variation in phase that can be used to compute velocity. 1) At the onset of the first positive lobe, both the moving and stationary spins have no phase variations. 2) The first lobe of the motion encoding gradient has been applied, resulting in the moving and stationary spins acquiring phase shifts. 3) The inverse motion encoding gradient is applied causing the stationary spin phase to return to zero while the moving spin has a net phase shift.

Phase contrast imaging techniques can be processed to create magnitude, complex difference, and phase images. For magnitude images, the contrast comes from the strength of magnetization at each spatially encoded location. These types of images are similar in appearance to the typical MR imaging techniques as it can display anatomical details for the vessels and tissues. Complex difference images are generated by subtracting the complex data from the two PC acquisitions. Typically, these images are used for visualization and segmentation of vessels because signal from moving spins are highlighted and static background tissue is suppressed. Lastly, as discussed previously, phase difference images can be generated by performing pointwise subtraction of the phase images from the two PC acquisitions. For these images, moving spins in one direction will appear bright and moving spins in the opposite direction will appear dark. This allows for artery and vein differentiation as well as retrograde flow detection. In addition to providing vessel anatomy, the phase difference image provides quantitative values of blood velocities (speed and direction). By defining a vessel area within a PC image, a vessel's cross-sectional area can then be used in combination with blood velocities to quantify volumetric flow rates. Furthermore, if phase contrast images are acquired with cardiac gating, then time-resolved reconstructions can be completed by binning the data into images over multiple cardiac phases. This allows for the quantitative assessment of blood flow over a cardiac waveform. Representations of magnitude, complex difference, and phase images, with an associated time-resolved cardiac waveform, can be viewed in Figure 2-11.

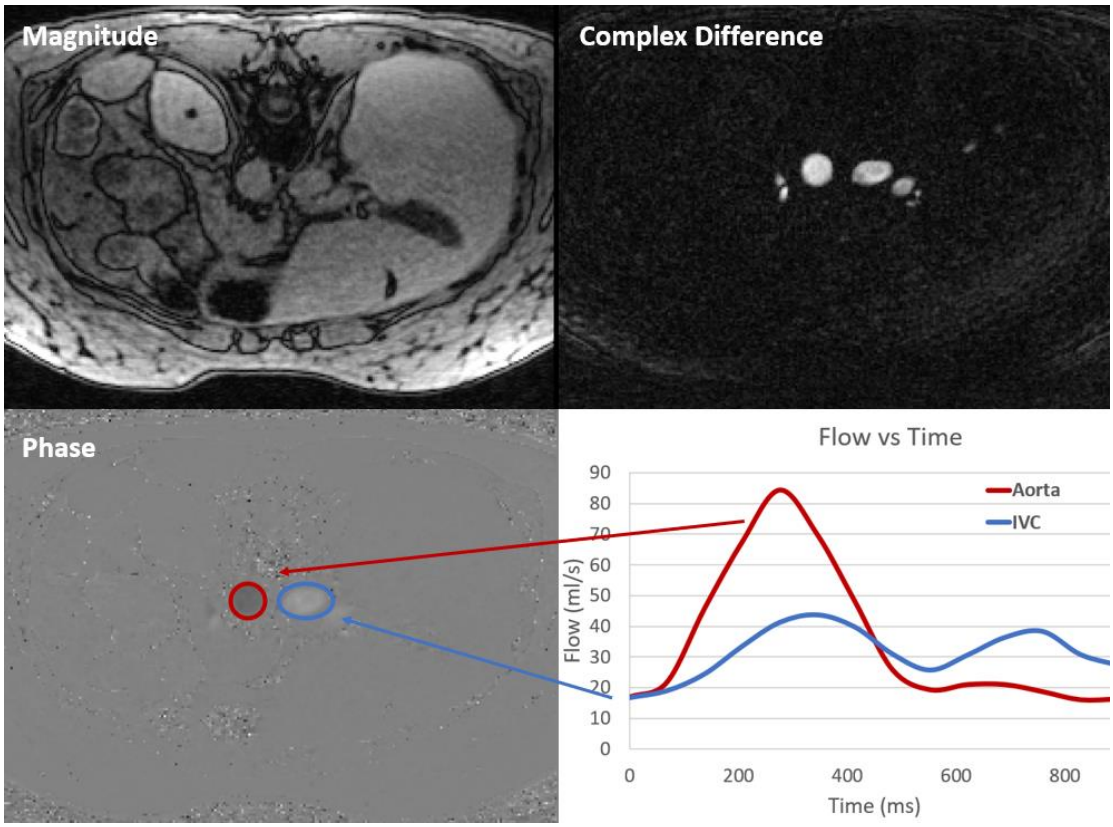

Figure 2-11: Phase contrast imaging can be used to reconstruct magnitude, complex difference, and phase difference images. The magnitude images represent the traditional MRI images routinely used clinically. The complex difference images provide bright signals for locations where motion is occurring. The phase images can be used to encode the motion's speed and direction resulting in a velocity vector for all voxels. A region of interest (ROI) can be placed to investigate hemodynamics parameters, such as flow, for a single image or over a cardiac cycle. The flow profiles are plotted for the lower abdominal aorta and inferior vena cava.

Although a majority of MRI acquisitions utilize Cartesian trajectories, this work takes advantage of radial acquisition techniques (42). Radial trajectories do not use a phase encoding gradient for image acquisition but instead apply multiple frequency encoding gradients to populate k-space, which is the frequency space in which MRI images are acquired (43). By utilizing a radial acquisition, we can reduce the TR and TE acquisition times while undersampling k-space. Radial acquisitions can be completed for 2D and 3D acquisitions with sample trajectories shown in Figure 2-12. Major benefits of radial trajectories include the relative insensitivity to motion artifacts, flexible cardiac gating, and preserved spatial resolution while undersampling.

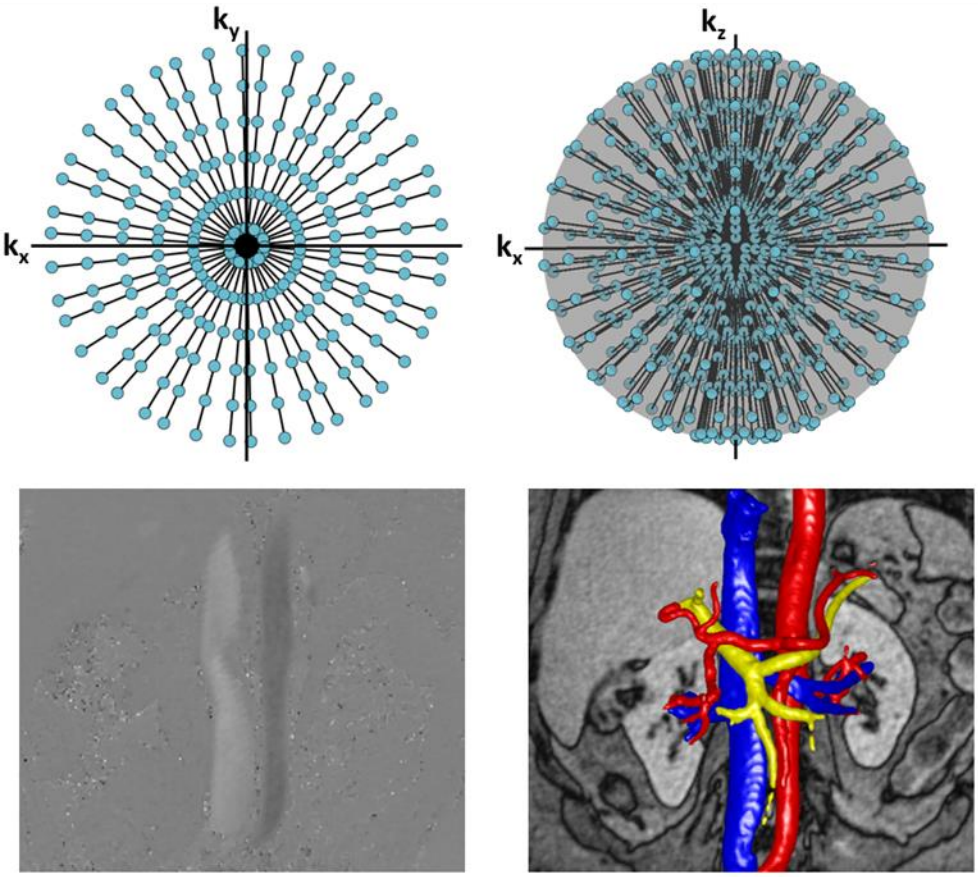

Figure 2-12: Radial gradients can be applied for 2D, 3D, or 4D phase contrast imaging acquisitions. The radial acquisition equally spaces k-space readout projections while passing through the center of k-space with each readout. This results in an acceleration imaging factor at the cost of under-sampling k-space. Radial acquisitions are motion robust and distribute the under-sampling artifacts diffusely allowing for minimal reductions in the image quality.

The vast majority of clinical phase contrast scans are two dimensional and quantify through-plane velocity or flow. To generate time-resolved velocity vector fields in three-dimensions, termed 4D flow MRI (13,44), cardiac-gated sequences with bipolar motion encoding gradients in all three spatial dimensions, with an associated flow-nulled background reference sequence, are required. The referenced technique is known as 4-point reference velocity encoding, while alternative methods exist such as 4-point balanced or 5-point balanced (45,46). 4D flow MRI allows for the analysis of complex flow fields within vascular networks throughout the body while providing large volumetric coverage. With the increase in dimensionality, especially for Cartesian acquisitions, scan times can become prohibitively

long, leading to limitations for clinical applications. Acceleration techniques, such as parallel imaging (47), compressed sensing (48), non-Cartesian trajectories (48), and view sharing (49), can be utilized to mitigate long scans and allow for clinical use. A 4D flow technique, known as Phase Contrast Vastly-undersampled Isotropic Projection Imaging (PC-VIPR (50,51)), is used throughout this work and takes full advantage of 3D radial undersampling to improve spatial and temporal resolution while keeping scan times relatively low (5-10 min). Through the application of PC-VIPR, 3D time-resolved blood velocity vector fields can be used for visualization and quantification of hemodynamic parameters. An abdominal 4D flow (PCVIPR) renal scan is shown in Figure 2-13 with quantitative cardiac waveforms and color-coded vector fields.

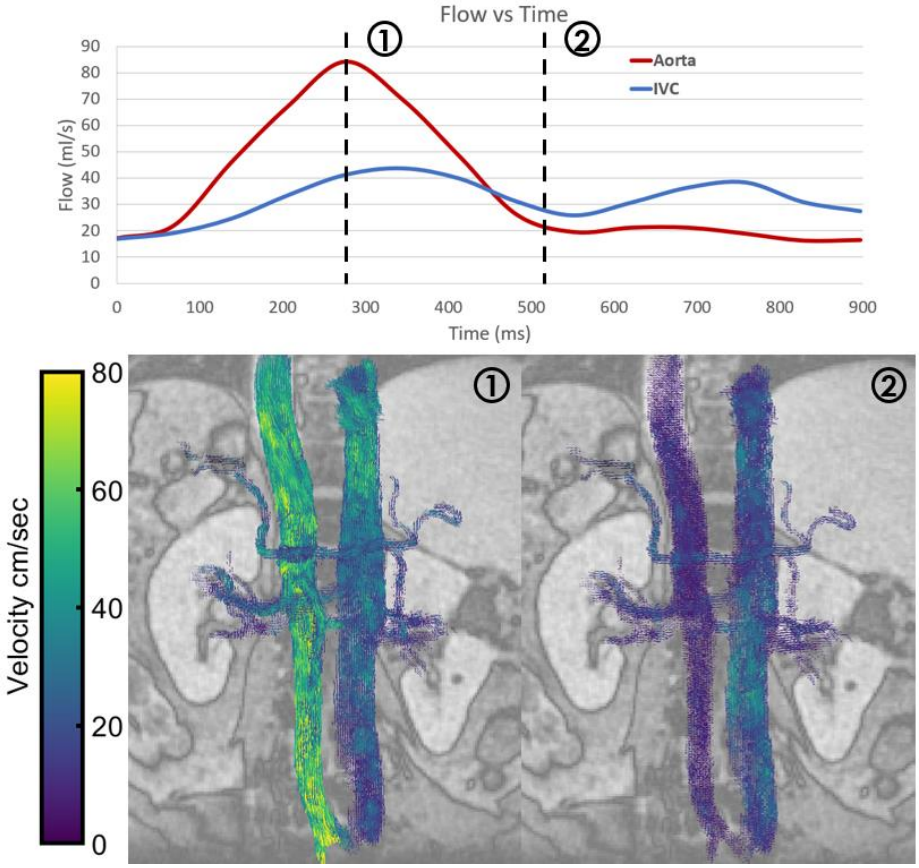

Figure 2-13: 4D flow MRI can acquire time-resolved vectors fields over a large 3D imaging volume. Quantification and visualization of these vector fields can be a powerful clinical tool in the assessment of vascular diseases. Flow waveforms were calculated for the aorta and inferior vena cava at a suprarenal location. The vector fields were color-coded with velocity at systole (1) and diastole (2) for the aorta and IVC, with the magnitude image overlaid for anatomical reference.

2.5 Digital Subtraction Angiography

The generation of digital subtraction angiography (DSA) images is made possible through the application of the x-ray imaging techniques previously described. As the name implies, DSA uses the subtraction between two radiographic images to produce diagnostic images of blood vessels (52,53). These images can provide a clear representation of vascular networks while lowering contrast doses compared to non-subtractive techniques. An initial non-contrast image, commonly referred to as the mask, is taken prior to contrast injection and shows the anatomy of a region and appears as a classical x-ray image. A high-density contrast material, such as iodinated agents, is injected into the vasculature and x-ray images are captured as the contrast moves through the vasculature. This image is commonly referred to as the fill image, as contrast is filling the vasculature in the imaged region. The high-density contrast agent causes an increase in x-ray absorption resulting in the vasculature appearing dark on the fill images. The mask image is identical to the fill image except for intensity changes in the vasculature caused by the presence of the contrast material. A subtraction between the mask and fill image is completed to remove the background structures and preserve the vasculature. With DSA imaging, pixels are converted to a log scale prior to subtraction, resulting in an image that is dependent on the contrast mediums presence. The derivation of DSA image generation is shown below using the x-ray intensity equations presented in Eq 2.8:

$$N_{mask} = N_0 e^{-(\mu b)(xb)} \quad (2) \qquad N_{fill} = N_0 e^{-(\mu b)(xb)} e^{-(\mu c)(xc)}$$

$$DSA = \ln(N_{mask}) - \ln(N_{fill})$$

$$DSA = \ln(N_0) - \mu_b x_b - \ln(N_0) + \mu_b x_b + \mu_c x_c$$

$$DSA = \mu_c x_c \qquad \text{Eq 2.16}$$

where μ_b is the linear attenuation coefficient (cm^{-1}) of the background, x_b is the thickness (cm) of the background, N_0 is the number of initial x-rays, μ_c is the linear attenuation coefficient (cm^{-1}) of the contrast agent, x_c is the thickness (cm) of the contrast region. Thus, DSA image intensities are linearly dependent upon the contrast agent's linear attenuation coefficient and the vessel thickness. It should be noted that

this derivation assumes a monoenergetic x-ray beam and that no scattering occurs (54). The addition of scatter causes a decrease in image intensity and causes the relationship to be non-linear.

The acquisition and reconstruction of accurate DSA images can be limited by the presence motion and noise (55,56). If there is no motion between the mask and fill images, then the only intensities in the final image will be due to the presence of contrast. In clinical application, a variety of in vivo sources of motion exist which can impact DSA image quality. The most obvious are bulk and respiratory motion which can be reduced with the application of breathholds, sedation, or physical restraints. Additional causes of motion include cardiac pulsations and peristalsis, which are more difficult to avoid or correct. Image subtraction, used for DSA generation, inherently causes a decrease in the signal-to-noise ratio, therefore the subtraction images appear nosier than the individual mask or fill image. To adjust for the increase in noise, the x-ray dose can be increased or scatter-reducing algorithms can be applied. Although there is an increase in noise, DSA improves the conspicuity of vessels by removing overlying anatomic clutter, leading to an improved ability to discern vessels. This allows for DSA to be a viable angiographic imaging option, especially for interventional procedures.

Traditionally, angiographic imaging techniques were primarily applied in 2D. With the increase in rotational capabilities of newer C-arm systems, 3D and 4D DSA applications have become possible (57). The basic idea for DSA image generation, acquiring a mask followed by a fill image with contrast injection, remains unchanged regardless of the acquired dimensionality. 2D imaging techniques keep a consistent projection angle and can acquire both the mask and fill images from a single image series. This involves imaging a few frames prior to contrast injection followed by a series of images capturing the contrast dynamics. In 3D and 4D DSA applications, the x-ray projection angle is rotated about the object of interested to provide depth information from multiple views. This requires two identical imaging rotations to be completed, one for the mask and one for the fill. The DSA images are then computed at each projection angle and the resulting images can be used to create detailed 3D or 4D angiograms. An outline of image acquisitions for 2D, 3D, and 4D DSAs is provided in Figure 2-14.

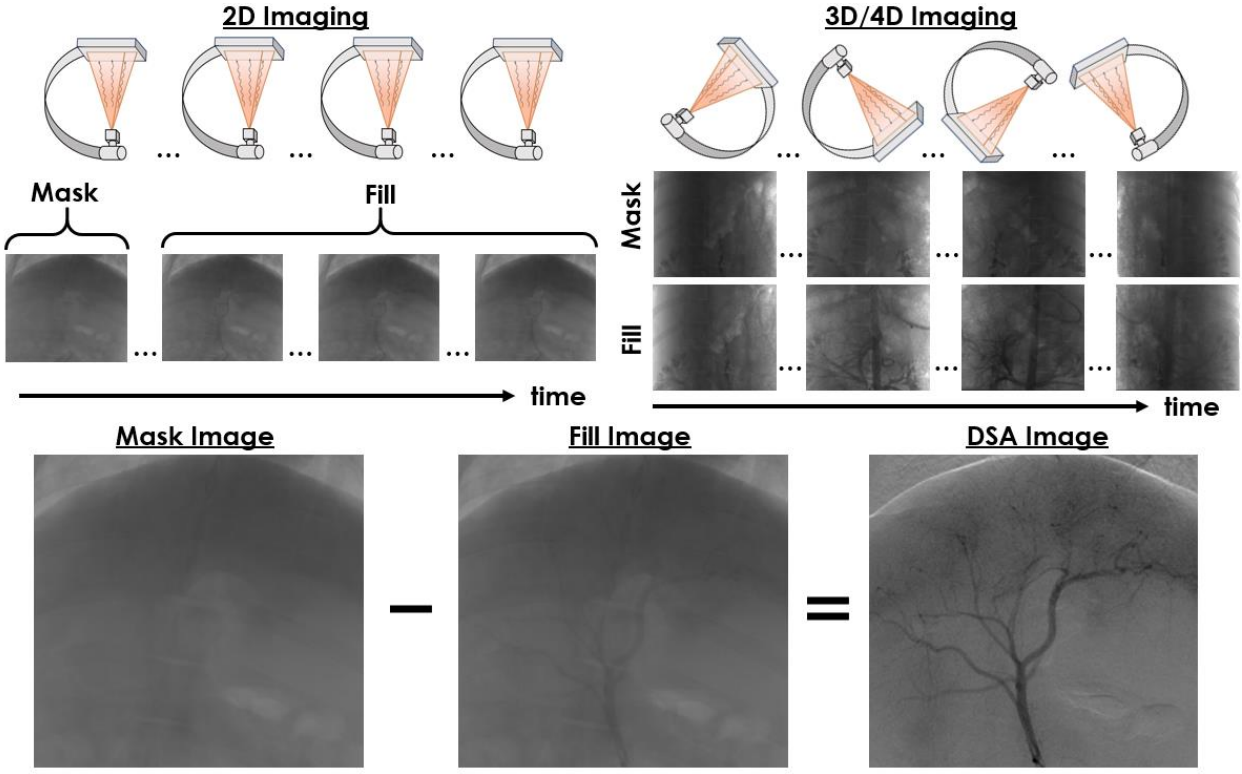

Figure 2-14: Digital subtraction angiography (DSA) is commonly completed with C-arm acquisitions. To create DSA images, a mask image containing only background signal is subtracted from a fill image which contains contrast injection dynamics. Both images are converted to the log space prior to subtraction so that the resulting image is linearly related to the contrast linear attenuation coefficient and the vessel thickness. 2D acquisitions keep a constant projection angle and can acquire both the mask and fill images from a single image series. 3D and 4D acquisitions are completed as the C-arm rotates about the imaged object and require separate acquisitions for mask and fill.

As DSA images are acquired throughout a contrast injection, the reconstructed images can provide both structural and temporal information related to blood vessels. 4D DSA takes advantage of both the spatial and temporal information captured in a 3D DSA to create a series of time-resolved 3D volumes. This is completed by first generating a 3D DSA reconstruction, without time dependence, and utilizing it as a constraining volume for the 4D DSA. The 2D DSA images, acquired during the C-arm rotation, are then back-projected through the constraining volume to provide temporal contrast information in 3D space. This allows for 3D vascular volumes to be viewed from any angle or time point over the DSA acquisition. An example of a 4D DSA reconstruction is shown in Figure 2-15.

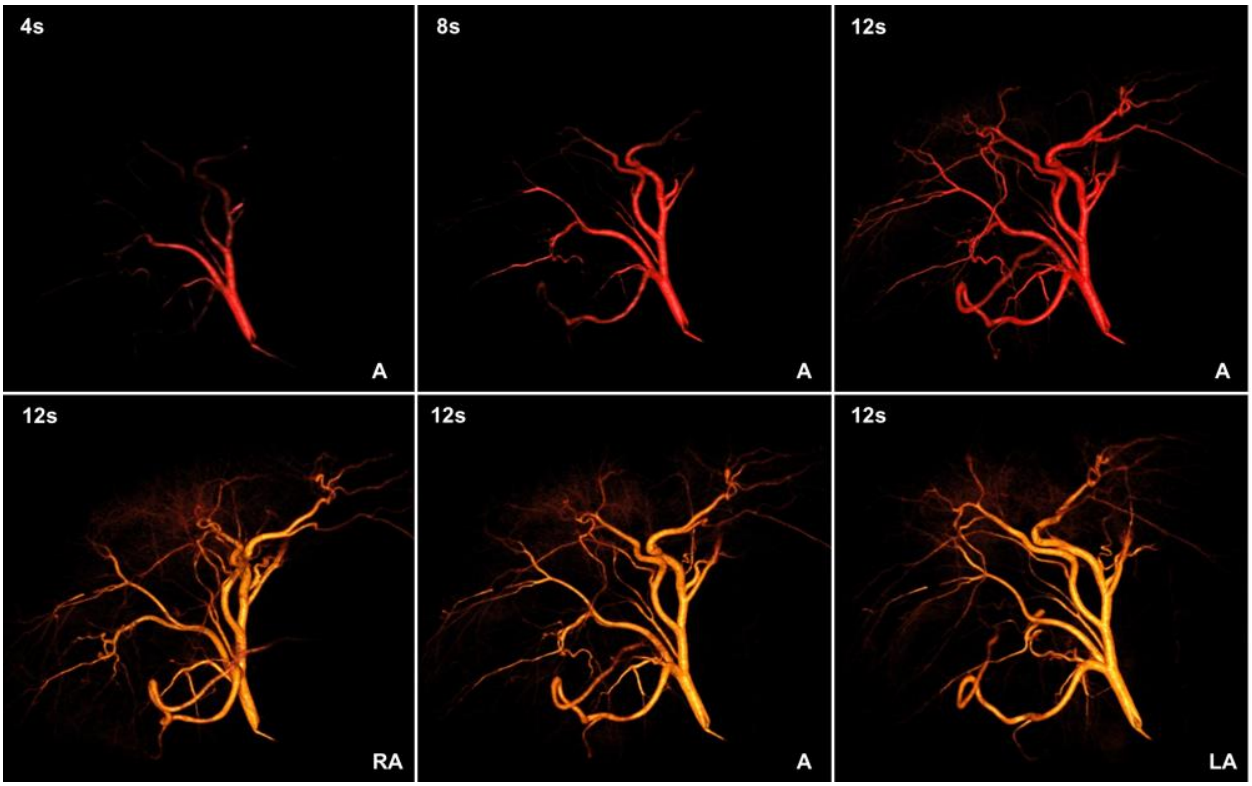

Figure 2-15: 4D DSA takes advantage of the spatial and temporal information provided by 3D DSA acquisitions. This allows for time-resolved 3D volumes to be created over the entirety of a contrast injection. Different temporal and spatial views can be used to provide additional information about vascular disease states. (Figure courtesy of Ece Meram)

The movement of radio-opaque contrast agents in a DSA image series has been utilized to provide quantitative values related to blood flow. A few common clinically available quantitative metrics include: area under the curve, time to peak, and mean transit time (58,59). Each of these metrics utilize the temporal information of the DSA acquisition and can be computed with a 2D or 4D DSA techniques. It has been shown that blood flow and velocity information may be useful for the assessment of vascular diseases (60–62). Due to DSA's ability to provide high temporal and spatial acquisitions, blood flow and velocity techniques have been developed utilizing bolus tracking or computational methods (14,63–65). For example, if two points are selected along a vessel path in a DSA image, the distance between points along a vessel can be computed through manual measurements or with the application of automated methods such as vessel centerlines. If the time-attenuation curves for each point are investigated, a shift in

the waveforms should be present as the contrast needs time to progress through the vasculature. Additionally, for arterial injections, the inherent cardiac pulsatility can cause unique time-attenuation curves to develop as the injected contrast agent interacts with the baseline blood flow. This creates a pulsatile time-attenuation signal, as the ratio of blood to contrast agent varies with the baseline blood flow rates. By utilizing computational methods(14), an optimal temporal shift can be computed that best aligns time attenuation curves. This temporal shift can be used in combination with the spatial distance between points to compute blood velocity. For volumetric techniques, such as 4D DSA, this can be extended to calculate blood flow with the additional computation of vessel area via segmentation. An example outline for blood velocity computations from 2D DSA can be viewed in Figure 2-16.

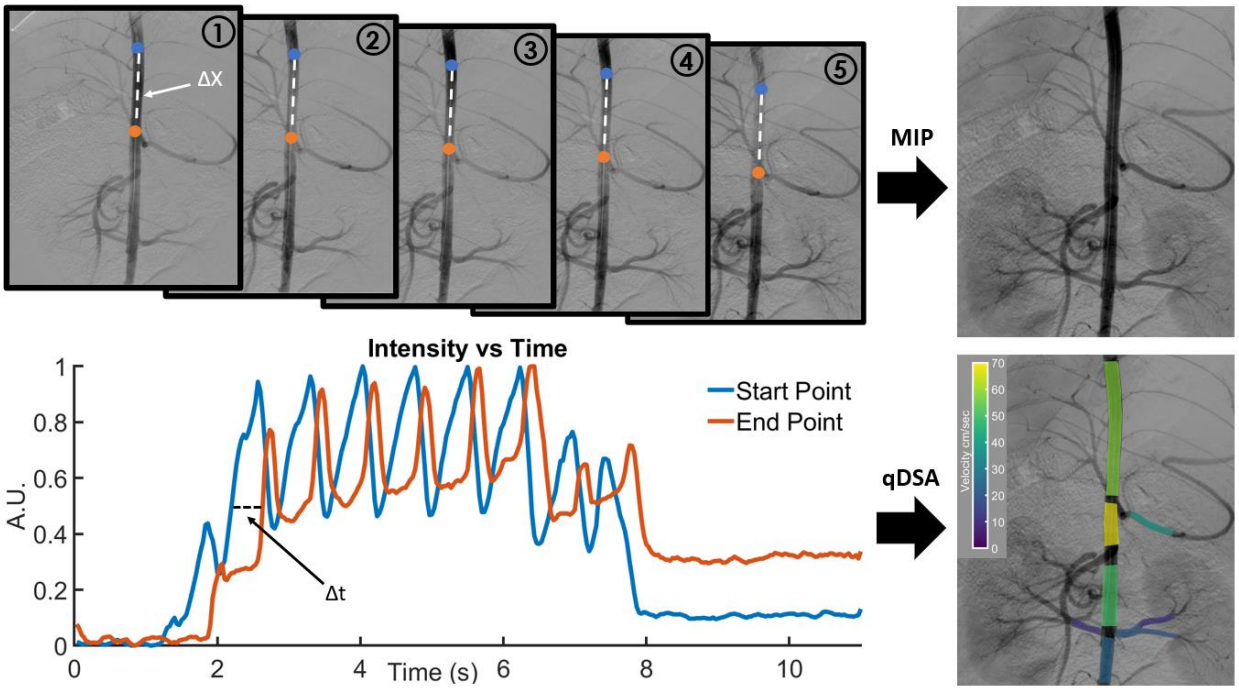

Figure 2-16: Quantitative digital subtraction angiography (DSA) can leverage the temporal and spatial information in DSA acquisitions to compute quantitative hemodynamic parameters, such as velocity and flow. The spatial distance between points can be measured manually or with automated techniques. A temporal shift between two locations can be computed by best aligning the individual time-attenuation curves. The vessel cross-section can additionally be measured to compute flow.

Chapter 3: A Technique for 2D DSA Intra-Procedural Blood Velocity Quantitation

3.1 Introduction

3.1.1 Angiographic Procedures

Angiographic procedures such as angioplasty, stent placement and transarterial embolization (TAE) are largely qualitative, relying on subjective, visual assessment of digital subtraction angiography (DSA) images to diagnose pathology, determine procedural endpoints, and evaluate treatment efficacy. Angiographic assessment using DSA depends on factors such as observer experience and perceptual bias, both of which have been previously shown to be a significant source of interpretive error in radiology(66). This leads to a high degree of interobserver variability and a decrease in reproducibility(67–69). Procedural outcomes are subsequently affected, including variable success rates in balloon angioplasty in peripheral arterial disease and poor correlation of tumoral perfusion changes with subjective treatment endpoints during TAE(70,71). Quantitative angiographic metrics may be beneficial in standardizing angiographic body interventions, ultimately improving their safety and efficacy.

3.1.2 Quantitative Techniques

Quantitative angiographic techniques, including quantitative color-coded DSA, 4D DSA, 4D Flow MR and 4D transcatheter perfusion, can provide data on hemodynamic parameters (e.g. time of arrival, flow, velocity)(50,63,64,72–76). DSA is the gold-standard imaging method for guiding and assessing intravascular procedures; as such, the application of MRI techniques for real-time guidance is limited by the need for additional specialized equipment and suites. 4D DSA requires rotational scans with additional radiation exposure and relatively long data acquisition times. Practically, this limits the number of 4D DSAs that can be acquired during any given procedure. Quantitative color-coded DSA can provide color-coded vessel displays based on time of arrival (TOA) or time to peak (TTP) during intravascular

procedures(59,77,78) but is highly susceptible to image artifact and variation in injection parameters(14,79,80). Additionally, it does not provide true arterial velocity or flow. A robust quantitative angiography technique that could provide blood velocities utilizing DSA would be minimally intrusive to the procedural workflow and would provide a quantitative complement to current assessment methods.

3.1.3 Study Motivation

The purpose of this study was to assess the accuracy, precision, and feasibility of a quantitative angiography technique which extracts blood velocity from time-resolved 2D DSA (qDSA) sequences. The ability to quantify blood velocity during procedures may provide insight and objective endpoints to clinical procedures.

3.2 Methods

All studies were performed with approval from the institutional animal care and use committee and complied with National Research Council guidelines.

3.2.1 Quantitative Angiography Method

The proposed quantitative angiography method uses the inherent cardiac pulsatility of arterial flow in addition to spatial information within an artery to compute blood velocity. Pulsatility of arterial blood flow during a contrast injection results in an oscillating contrast signal in the time-attenuation curve (TAC) of a given pixel in the DSA image sequence. This oscillation of signal, referred to as contrast pulsatility, represents a trackable marker of blood flow. Given two pixels along a vessel separated by distance d, the TACs from the two pixels will have similar pulsatile signals, offset by some temporal shift Figure 3-1. This temporal shift corresponds to the time a contrast bolus travels through a vessel. A shifted-least squares approach is employed to calculate the temporal shift(64). Distances and temporal shifts can be computed for pairs of points along the vessel centerline to improve statistical power and results in a spatially averaged blood velocity.

Blood velocities were calculated using a custom-built MATLAB tool Figure 3-1. The tool imports a DSA sequence and allows the user to choose a vessel of interest by selecting a proximal and distal point along the vessel. The vessel can then be manually or automatically segmented, after which the tool automatically determines the centerline. The user may view and window the time-intensity curves from the two selected points in order to select the region of strongest pulsatility. A correction for geometric magnification may be calculated and input into the tool by measuring a structure in the image and dividing by its known length (Magnification = Image Length / Object Length). The tool subsequently calculates an apparent blood velocity then multiplies by the magnification factor to convert it to a true velocity. Vessel foreshortening effects can arise for a vessel that is not perpendicular to the projection angle. Projection angle can be corrected for by dividing the apparent velocity by the cosine of projection angle offset (Velocity = apparent velocity / cos(projection angle)) which could be estimated using 3D reconstructions. Alternatively, a 3D angiogram can be utilized to select an optimal 2D projection that minimizes vessel foreshortening.

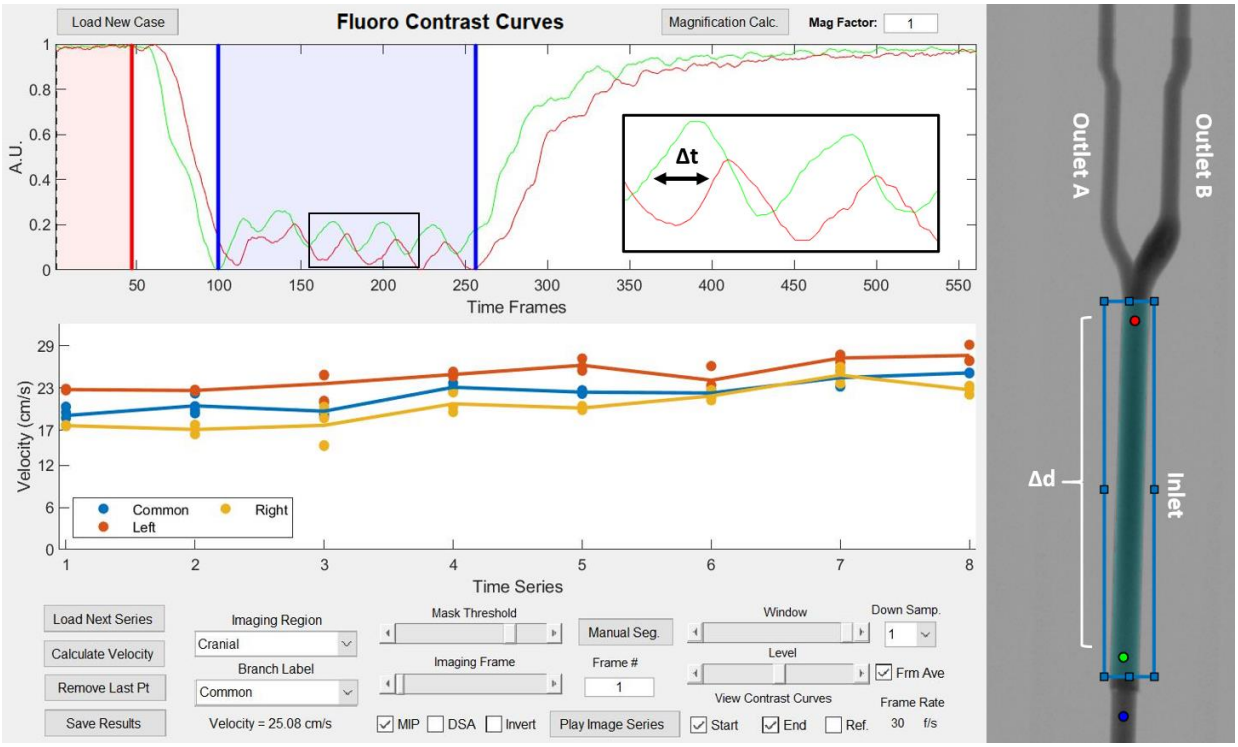

Figure 3-1: qDSA calculations were completed with the custom built post processing tool in MATLAB. Vessel start and end points are selected by moving the red and green points on the acquired image. Temporal windowing is adjusted by changing the blue shaded region overlaid on the time attenuation curves. The spatial information and temporal information used for velocity calculation are derived from the Δd and Δt. Visualization of the acquired image series can be completed using the tool's built in functions.

3.2.2 Phantom Study

In vitro validation of the qDSA method was performed in a silicone vascular bifurcation phantom (Shelley Medical Imaging Technologies, Ontario, Canada) to assess the algorithm in a controlled environment using different image acquisition parameters. DSA acquisitions were performed in triplicates for each experimental setup using an Artis zee x-ray system (Siemens Healthineers, Forcheim, Germany) and angiographic injector (Nemoto, Tokyo, Japan). A pulsatile displacement pump (BDC Laboratories, Wheat Ridge, CO), filled with water, was connected to the phantom in order to produce a physiologic flow profile similar to a cardiac cycle at a rate of 60 beats per minute. Average inlet velocity was calculated during all DSA acquisitions using a non-intrusive ultrasonic flow sensor measurement (Transonic, Ithaca, NY) and dividing by the known tube diameters. Experimental setup and sample

ultrasound flow probe acquisition for a single injection can be viewed in Figure 3-2. Imaging parameters of interest included baseline flow rate, contrast injection rate, projection angle, and magnification. To investigate these parameters, we varied the pump velocity, injector rate, gantry rotation and table height respectively. A guidewire, with a 3 cm long radiopaque tip, was navigated into the phantom and was used to correct for magnification. A complete list of imaging parameters for all experiments are included in Table 3-1.

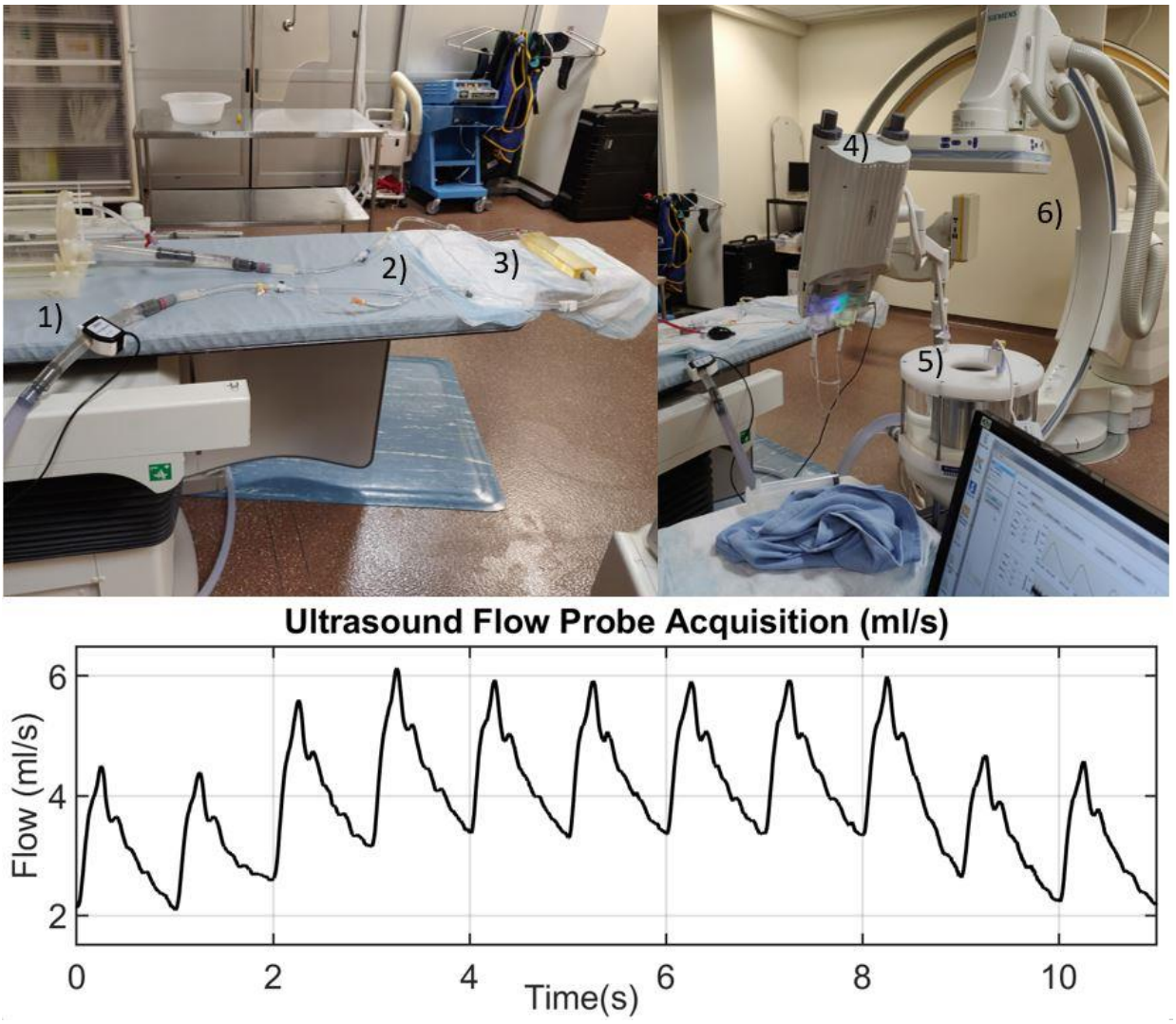

Figure 3-2: Experimental setup for the phantom study is shown with a sample ultrasound flow probe acquisition. Key components required for this study are present: 1) Ultrasonic flow probe, 2) catheter access location, 3) bifurcation model, 4) contrast injector, 5) BDC flow pump, and 6) Artis zee x-ray system. The sample flow probe shows an increase in flow during the injection region (2-9 sec) and a heart rate consistent with the desired 60 bpm.

Baseline Flow	Pump Flow (ml/s)	Injection Rate (ml/s)	SID (cm)	Projection Angle	Injection Time (s)
	6.8	**1.5 - 3**	120	0	8
	12.2	**1.5 - 3**	120	0	8
	16.8	**1.5 - 3**	120	0	8
	22.1	**1.5 - 3**	120	0	8
	27.2	**1.5 - 3**	120	0	8
Projection Angle					
	5.2	2	120	**0**	10
	5.2	2	120	**5**	10
	5.2	2	120	**10**	10
	5.2	2	120	**20**	10
	5.2	2	120	**30**	10
Magnification					
	7.4	2.5	**90**	0	6
	7.4	2.5	**100**	0	6
	7.4	2.5	**110**	0	6
	7.4	2.5	**120**	0	6

Table 3-1: Experimental parameters used to evaluate baseline flow rate, injection rate, projection angle, and magnification are present in the table. The bolded italicized values are the parameter that is being varied during each experiment.

3.2.3 In Vivo Study

The in vivo validation of the qDSA method was performed in a porcine model. Female domestic swine (n=2, 50 kg, approximately 3-4 months of age) were sedated with intramuscular tiletamine hydrochloride/zolazepam hydrochloride (7 mg/kg; Telazol; Fort Dodge Animal Health, Fort Dodge, IA) and xylazine hydrochloride (2.2 mg/kg; Xyla-Ject; Phoenix, St. Joseph, MO). Anesthesia was maintained with inhaled 1.0%–2.0% isoflurane (Halocarbon, River Edge, NJ). An auricular vein was cannulated for administration of intravenous fluids. First, the animals underwent 4D Flow MRI (3T Signa MRI scanner, GE Healthcare, Waukesha, WI) using a radially undersampled sequence, PC VIPR**(45)**. The animal was then transferred to the angiography suite. The right femoral artery was accessed and a 5Fr angled Glide Catheter (Merit Medical, Salt Lake City, UT) was used to select arteries of interest (left iliac, left and right

renals, common hepatic, splenic). A guidewire, with a 3 cm radiopaque tip, was navigated into the vessel of interest and a fluoroscopic image was acquired prior to DSA acquisition for geometric magnification corrections. Projection angles for 2D DSA acquisitions were selected to minimize the effect of vessel foreshortening. Triplicate DSAs were acquired in each artery with a breath hold at end expiration. A complete list of imaging parameters used for MR and DSA acquisitions can be seen in Table 3-2. Velocities were calculated and compared between the MR and DSA techniques. A semi-automated workflow for the 4D flow MRI analysis was developed in MATLAB 2018a. Angiograms were segmented using an adaptive region growing technique on the complex difference data. A 3D centerline path was generated to aid in the automatic placement of cross-sectional planes. Automatic segmentation of vessels was completed using a local thresholding technique and reported velocities were an average of all points along the vessel centerline. In order to compare velocities on MRI to those on DSA, which are acquired in the presence of intra-arterial contrast injection, velocities calculated on MRI were adjusted by adding velocity from an injection equivalent to that performed during acquisition of the DSAs (programed injection rate (2ml/s) divided by the 4D flow MRI vessel area).

DSA Swine Scan	Injection Rate (ml/s)	Injection Time (s)	Projection Angle	Frame Rate (fps)
All Vessels	2	12	0	30
MRI Swine Scan	Spatial Res. (mm)	Scan Time (min)	VENC (cm/s)	Time Frames
All Vessels	1 x 1 x 1	18	100	14

Table 3-2: In vivo scan parameters for qDSA and 4D Flow MRI. Identical scans were used for all vessel locations, including: Iliac, right renal, left renal, common hepatic, splenic. MRI time frames is the number of reconstructed volumes for a cardiac cycle. The velocity encoding (VENC) was set to 100 cm/s in order to capture velocities from all abdominal vessels in a single scan.

3.2.4 Statistical Analysis

To assess the correlation between the external flow probe and the velocities calculated from the qDSA technique in the phantom study, linear regression was used. Associated model p-values, 95% confidence intervals and Pearson's correlation coefficient, r, were all calculated following model estimation. Linear regression and Bland-Altman analysis were used to assess the calibration between qDSA velocity and 4D flow MRI in the in-vivo study. Right-tailed chi-square tests were used to assess if the observed variances of the phantom qDSA measurements across different magnifications and angle corrections were less than 5% of the mean in the associated flow probe. A desired variance of 5% of the mean velocity from the ultrasonic flow probe was set as the upper limit for the projection angle and magnification correction techniques. This was used to establish the precision of our tool in cases where corrective factors may be needed. For this study, a p-value < 0.05 was considered statistically significant. All statistical analyses were done using R (V 3.6.2, R Core Team, 2019).

3.3 Results

3.3.1 Phantom Study

Quantitative velocities were computed using the proposed custom-built MATLAB tool. The tool was able to successfully load DSA image series, select vessels of interest, complete vessel segmentation, allow temporal windowing, and compute velocities for all cases. Magnification corrections from a reference object were computed and implemented into the velocity calculations for all DSA acquisitions. All computations were completed within 2-3 minutes of acquisition during experiments. The physiologic pulsatile cardiac waveforms were inspected using the non-intrusive ultrasonic flow probe prior to and during DSA acquisition. The waveforms maintained their pulsatility for all pump and injection rates. Adequate contrast mixing was seen in all DSA acquisitions completely filling the vessel and maintaining a pulsatile nature.

The pulsatile pump's average and peak velocities were measured prior to the bifurcation and ranged from 8-30 cm/s and 13-55 cm/s respectively. Linear regression between the calibrated external

flow probe and velocities calculated from our qDSA technique is shown in Figure 3-3. The linear regression equation was: VDSA = 1.012*VUS – 3.043, where VDSA is the velocity calculated from qDSA and VUS is the velocity measured with the ultrasound flow probe. A strong correlation between the variables was observed (r = 0.996, p<.0001). The 95% confidence interval (CI) for the slope was [0.989,1.035] and the 95% CI for the intercept was [-3.52, -2.565].

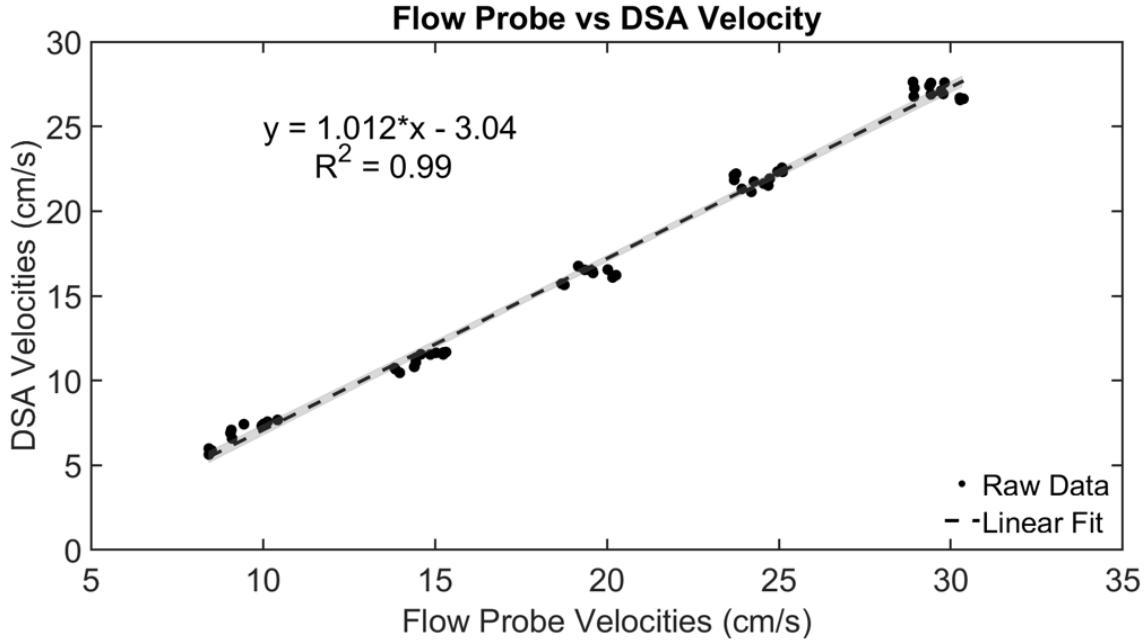

Figure 3-3: Linear regression analysis between the flow probe velocities and the calculated qDSA velocities. The shaded region represents the 95% confidence interval. The data were found to be strongly correlated (r = 0.996, p<.0001).

The variance of qDSA velocities decreased after correction for magnification and projection angle. The flow probe's baseline mean velocity (±SD) for projection angle and magnification was 14.18 ± 0.053 cm/s and 14.65 ± 0.129 cm/s respectively. The uncorrected and corrected velocities as a function of projection angle can be seen in Figure 3-4. For projection angle correction, the qDSA variance ($\sigma 2$ = 0.0745, 95% CI [0.0388,0.1933]) was less than the defined variance limit (5% Mean = 0.709) resulting in a failure to reject the null hypothesis ($\sigma 2$ < 5% Mean, p = 0.999). The uncorrected and corrected velocities as a function of table height (magnification) for the inlet and outlet branches can be seen in Figure 3-5. For magnification correction, the qDSA variance ($\sigma 2$ = 0.2147, 95% CI [0.1073,0.6188]) was

less than the defined variance limit (5% Mean = 0.733) resulting in a failure to reject the null hypothesis ($\sigma 2 < 5\%$ Mean, $p = 0.956$).

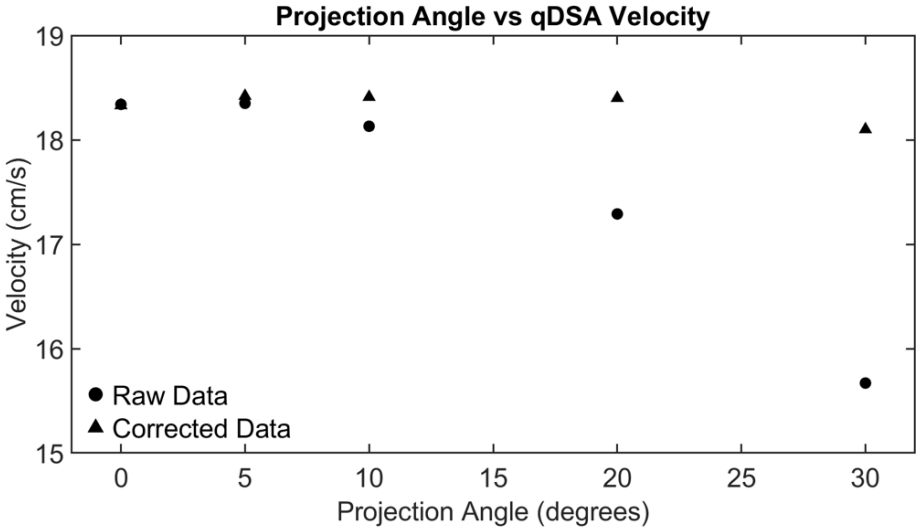

Figure 3-4: The raw qDSA velocity calculations as a function of projection angle are plotted as circles. As the projection angle increases the calculated velocity values decrease as a function of cosine the projection angle. Applying the projection angle correction reduces variation in the calculated velocity over a range of projection angles.

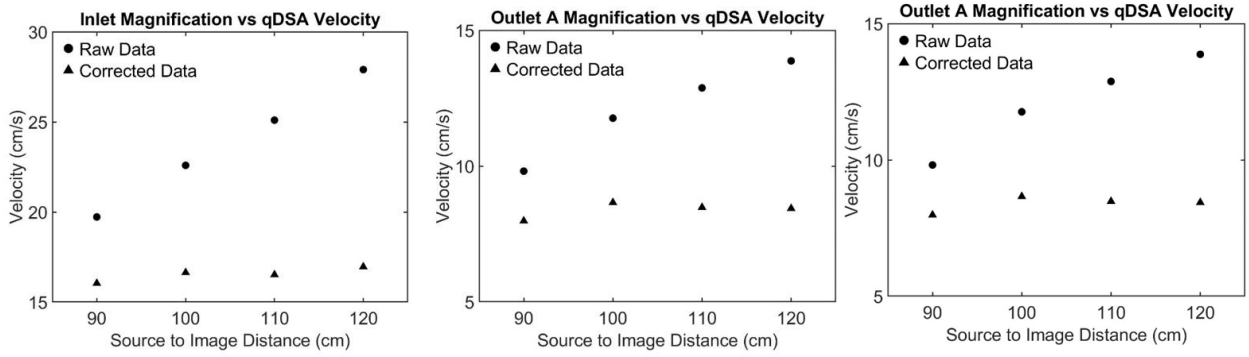

Figure 3-5: The raw qDSA velocity calculations as a function of source to image distance (SID) are plotted as circles. As the SID increases the magnification factor increases causing the calculated velocity values to increase as a function of magnification. Applying the magnification correction, using a reference object, reduces variation in the calculated velocity over a range of SIDs.

3.3.2 In Vivo Study

Triplicate DSA acquisitions were successfully acquired at the five abdominopelvic arterial vessels of interest: left iliac, left renal, right renal, common hepatic, and splenic. Adequate downstream contrast

mixing was seen in all in vivo DSA acquisitions, allowing for velocity calculations to be completed in the injected vessel. Linear regression between 4D flow MRI velocities and calculated qDSA velocities is shown in Figure 3-6. The linear regression equation was: VDSA = 1.01*VMRI -0.10, where VDSA is the velocity calculated from qDSA and VMRI is the velocity measured with 4D flow MRI. There was a strong correlation between velocity on 4D flow MRI and qDSA (r = 0.880, p <.01). The Bland-Altman analysis showed a bias of 0.117 cm/s between techniques with a upper limit of agreement of 10.53 cm/s and a lower limit of agreement of -10.30 cm/s. Figure 3-7 shows the quantitative angiograms, color-coded by velocity, from the MRI and DSA scans from swine 1. The quantitative velocity values from MR and DSA for both swine can be found in Table 3-3. The distribution of velocities followed similar trends for both imaging modalities.

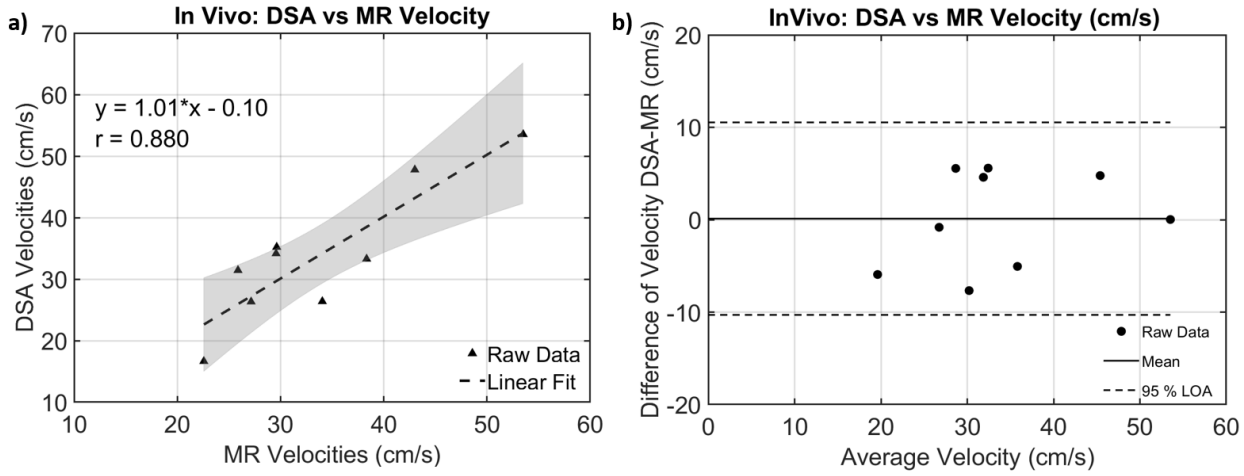

Figure 3-6: a) Linear regression analysis between the 4D Flow MRI velocities and the calculated qDSA velocities (r = 0.880, p = <.001). The shaded region represents the 95% confidence band. b) Bland-Altman analysis between the 4D Flow MRI and qDSA velocities (Bias = 0.117 cm/s, LOA [-10.30 cm/s, 10.53 cm/s]).

Swine 1	MR Velocity (cm/s)	DSA Velocity (cm/s)	DSA Std. Dev.	Mag. Factor
Common Hep.	53.51	53.51	6.69	1.19
Splenic	27.15	26.33	4.53	1.11
Left Renal	22.57	16.65	1.98	1.28
Right Renal	25.88	31.44	4.39	1.16
Iliac	38.33	33.28	5.03	1.20
Swine 2				
Common Hep.	43.01	47.78	8.78	1.28
Splenic	29.56	34.16	2.72	1.26
Right Renal	29.62	35.21	4.48	1.28
Iliac	34.05	26.38	3.11	1.33

Table 3-3: Quantitative values from the in vivo study for both imaging modalities are presented in the table. The standard deviation of the DSA velocity is provided from the triplicate scans. The magnification factor was calculated for each vessel by imaging a reference wire, of 3 cm in length, in the vessel of interest prior to injection.

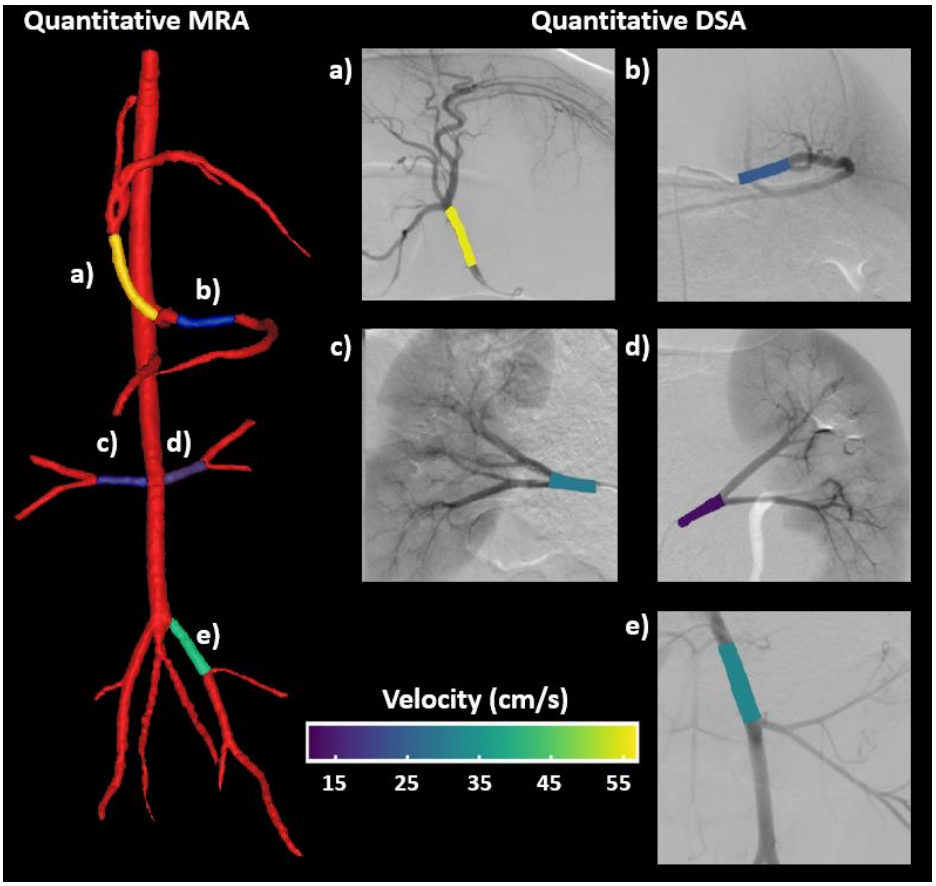

Figure 3-7: Quantitative angiographic images for both the 4D Flow MRI and qDSA methods from Swine 1. The magnetic resonance angiogram (MRA) 3D reconstruction was manually segmented and average velocities were calculated for the associated DSA vessels. The distribution of velocities was similar between both imaging modalities.

3.4 Discussion

This study investigated the feasibility of a quantitative angiography method using time-resolved 2D DSA. The method was assessed for accuracy and precision in a phantom model and an in vivo porcine model. Our results indicate that qDSA allows the calculation of quantitative velocities, over a range of physiologic abdominal arterial velocities(81) in near real-time, that are both accurate and precise. Potential errors from angle projection and magnification were investigated and successfully corrected for, demonstrating the robustness of the technique. Quantitative velocities were computed in vivo using branches of the abdominal aorta and were found to be strongly correlated with an established quantitative MRI technique. The application of the proposed method was similar for both the experimental and in vivo studies, indicating the potential for clinical adaptation.

Prior intraprocedural quantitative imaging techniques have been described, including a commercially available DSA-based technique (syngo iFlow; Siemens, Forchheim, Germany). However, quantitative color-coded DSA does not provide true arterial velocity or flow, rather it provides time-attenuation curves for specified points and color-coded vessel displays based on time of arrival (TOA) or time to peak (TTP). Such an analysis is prone to error and sensitive to changes in cardiac output, motion, total amount and duration of contrast medium administration, imaging parameters (eg, injection delays), and angiographic catheter position (82–84). The proposed qDSA technique takes advantage of spatial and temporal information along the vessel allowing for a more robust quantitative technique. Volumetric techniques, including quantitative 4D transcatheter intra-arterial perfusion (TRIP) MRI and 4D DSA have also been described(63,64,76). A major advantage of volumetric techniques is the ability to provide flow, not just velocity, which can be important for interventions in which vessel diameters change. TRIP MRI lacks feasibility as it requires a complex hybrid angiography/MR suite only available at select institutions, and also requires significant time and cost. 4D DSA is useful for characterizing blood flow at baseline and upon completion of a procedure, but the long data acquisition times and susceptibility to motion artifacts make it less suitable for repeated use throughout a procedure.

The qDSA technique described here could be easily translated to intraprocedural clinical workflows given that it would only require modification to image acquisition parameters. In the present study, all velocity calculations were performed within 2-3 minutes per image acquisition using the prototype MATLAB tool on a standard laptop (Intel Core i7-8550U 1.80 GHz CPU, 16 GB RAM). The variation in post processing time was dependent upon the length of the vessel of interest and number of time frames used for velocity calculations. Further refinement of the technique and tool will likely lead to significant reductions in computational times, enabling near real-time determination of velocities repeatedly during procedures. Although qDSA is currently limited to blood velocity, further development may allow for calculated velocities to be converted to blood flow using forward projection techniques on pre-procedure 3D imaging (65). This would permit flow quantification in a manner more similar to 4D Flow MR or 4D DSA.

An accurate velocity calculation requires precise knowledge of both the distance the blood traveled and the time (or temporal shift). The measured distance will differ from the true distance if the projection is not orthogonal to the vessel segment. The proper projection angle can be determined from 3D imaging, either preprocedure or at the time of the procedure, and the true distance can be determined by placing an object of known dimensions into the vessel segment (eg a guidewire or catheter with radiopaque markings). While both projection angle and magnification corrections are important to achieve accurate absolute velocity values, relative velocity changes during a procedure (eg, pre- and post-intervention) can be calculated without incorporating corrections as long as the table position and projection angle are maintained. Furthermore, corrections for projection angle may be unnecessary for many abdominopelvic interventions given that many vessels are relatively straight, vessels can typically be laid out in AP or shallow oblique projections, and minimal variation (< 5%) in velocity was observed over a wide range of projection angles (± 15 degrees) in the phantom study. A minimum frame rate is required to achieve adequate temporal resolution for the higher velocity values encountered in clinical practice. In its current form, qDSA is associated with additional radiation dose (from additional high frame-rate scans).

However, preliminary studies indicate that qDSA may also be viable with fluoroscopy, which would significantly decrease the exposure compared to subtraction angiography.

X-ray videodensitometric blood velocity methods have been previously described (14). Many of these blood velocity techniques were developed for cerebrovascular interventions. Few have been developed or validated in the abdominal vasculature. Furthermore, an analysis tool for near real-time calculation has yet to be created for use in body interventions. We have developed a tool that allows the calculation of blood velocity from 2D DSA sequences within minutes with minimal user interaction. The graphical user interface allows common visualizations of DICOMS and TACs while providing quantitative blood velocity values from temporally and spatially segment vessels of interest. The development of this qDSA velocity tool makes intraprocedural blood velocity calculations feasible and more readily translatable to clinical workstations.

Our study had several limitations. Our preliminary in vitro testing was performed in a bifurcation phantom with three segments, all relatively linear and of constant diameter. The velocity in this phantom is primarily laminar, but the larger outlet does contain a region of recirculation. The abdominal arteries have more tortuosity and variation in vessel diameter which can lead to increased turbulent velocities and disruption in pulsatile signal. Additionally, we used a pump that generated a repeatable pulsatile signal, which may not entirely represent the hemodynamic heterogeneity of abdominal vasculature. Despite the limitations of the phantom model, the results of the in vivo experiments suggest the technique is robust and accurate with more complicated vessel geometries. In our in vivo testing, the MR velocity data was acquired without an intra-arterial injection requiring an additive velocity correction before a direct comparison to qDSA velocity could be made. To replicate the DSA injection during MRI, catheter placement could be completed under fluoro guidance and then the animal could be moved to the MRI scanner. However, for a multi-vessel analysis, this would require a minimum of 5 trips between imaging modalities with the risk of catheter movement occurring during each transport. Additionally, the MR scans would need to be adjusted to capture near real-time velocities, limiting the scans to 2D techniques

which would no longer allow averaging along the vessels of interest.

3.5 Conclusions

qDSA can provide quantitative blood velocity measurements during arterial interventions and was found to be strongly correlated with established quantitative techniques. The major advantage of the proposed technique is near real-time measurement of relative and absolute changes in blood velocity in an intraprocedural, interventional environment. While our study focused on the accuracy, consistency, and feasibility of calculating blood velocity using time-resolved 2D DSA sequences, further investigation is necessary to evaluate the performance of the qDSA technique in an intra-procedural context.

Chapter 4: Characterizing Hepatic Arterial Velocity Changes from TAE

4.1 Introduction

4.1.1 Hepatocellular Carcinoma

Hepatocellular carcinoma (HCC) is the most common primary liver cancer and is the fourth leading cause of cancer-related death worldwide(85). It is predicted that 42,810 additional new cases will occur with an estimated 30,160 deaths in the US alone(86). A few of the most important risk factors associated with the development of HCC include chronic liver disease and cirrhosis. Incidence of HCC has been increasing for the last two decades with models predicting a continued increase for the next ten years(87). HCC presentation has altered significantly over the past few decades due to the screening of high-risk patients (eg. Cirrhosis) with non-invasive imaging techniques. The diagnosis of HCC can be completed through the use of imaging alone and in scenarios where biopsy is required imaging is typically completed in tandem for guidance(88). The best option for treatment of HCC is liver transplantation, but due to the limited number of good quality donor organs other treatment methods must be utilized. The alternative treatment options to liver transplant include: resection, thermal ablation, embolization (bland, chemo, radio), or systemic therapies.

4.1.2 Trans-arterial Embolization

Embolization is a procedure that injects a substance directly into the arterial system, with the intent of reducing blood flow to a non-healthy (cancerous) region. This is a common minimally invasive treatment option for patients that have tumors that cannot be removed surgically. The four most common embolization techniques include: trans-arterial embolization (TAE), trans-arterial chemoembolization (TACE), drug-eluting bead chemoembolization (DEB-TACE), and radio embolization (RE). TAE uses the injection of small particles directly into the artery to plug up vessels and cause necrosis to the tumor. TACE follows a similar technique but prior to plugging up the arteries chemotherapy agents are injected

into the artery. DEB-TACE is essentially the same procedure as TACE except that the drug-eluting beads are close to the cancer and slowly release the chemo. RE relies on the combination of embolization and radiation therapy to delivery radioactive isotopes close to the tumor site. Currently it is unclear which treatment method has the best long-term outcome for patients. An example of a TAE can be seen in Figure 4-1.

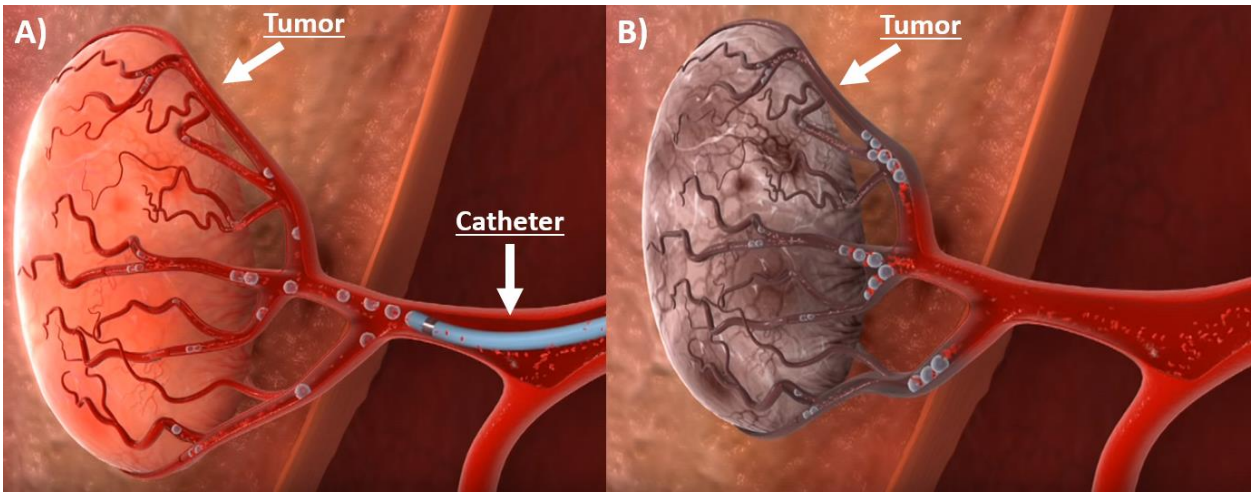

Figure 4-1: A representation of a trans-arterial embolization (TAE) being used as a treatment method for hepatocellular carcinoma (HCC). In the presence of an unresectable tumor, TAE can be a viable treatment option that utilizes a catheter to deliver particles into the arterial vasculature to block off tumor blood supply (A). By blocking the blood supply to the tumor this in turn leads to tumor necrosis(B).

4.1.3 Embolization for HCC

Patients with intermediate-stage hepatocellular carcinoma (HCC) are commonly treat with minimally invasive intra-arterial therapies, such as TAE or TACE(89). Multiple studies have shown the benefits provided by TACE and TAE for HCC patient survival than compared to alternative treatments(90,91). In addition to being a treatment method, these embolization techniques have been utilized to delay disease progression, reducing the demand for transplantation in HCC patients(92,93). The effectiveness of TAE and TACE depend on achieving the appropriate degree of stasis in the target vasculature and tumor. Not enough stasis can lead to insufficient tumor necrosis, alternatively causing complete stasis can upregulate angiogenesis factors, increase liver toxicity, and increase mortality(94,95). Treatments ending at sub-stasis have been shown to be a more optimal endpoint and can in increase the overall survival when

compared to complete-stasis(96). Determining a sub statis endpoint for TAE and TACE is completed with subjective angiographic assessments of radiographic images, which have high inter-observer variability and are inconsistent(70). Determining objective endpoints through the application of non-invasive imaging would help to standardize the procedures, increase treatment efficacy, and improve patient outcomes.

4.1.4 Imaging for HCC

Imaging is critical for establishing a diagnosis and staging HCC. A variety of common medical imaging modalities, including ultrasound (US), computed tomography (CT), magnetic resonance (MRI), angiography, and positron emission tomography (PET), are used in the assessment of HCC patients. Currently, ultrasound is the recommended method for screening at risk HCC patients. CT and MRI are the standard diagnostic tests for HCC, with potential for PET to assist in staging the disease(97). Attempts to establish quantitative metrics that may aid in the treatment or management of patients have been completed. Quantitative 4D transcatheter intra-arterial perfusion MRI was investigated but required specialized infrastructure making wide-spread adoption difficult(98). A 4D-digital subtraction angiography (DSA) feasibility study showed that blood velocity calculations were possible in a hepatic swine model(72). This may lead to the application of quantitative 4D-DSA pre- and post- HCC intervention to assess the success of treatment. Recently, color-coded DSA (ccDSA) has demonstrated validity as a tool for quantifying embolization endpoints(77,99,100). The technique uses contrast arrival dynamics such as time-of-arrival (TOA), time-to-peak (TTP), and area under the curve (AUC) to quantify changes in blood flow.

4.1.5 Study Motivation

4D flow MRI is an established quantitative imaging technique that allows for macroscopic vasculature visualization and hemodynamic quantification to be completed over a large imaging volume. This technique can be used to characterize pre- and post- procedural changes in blood velocity in response to vascular intervention on a local and global level. Quantitative digital subtraction angiography (qDSA) is a

newly developed technique which calculates blood velocity in a vessel of interest using time attenuation curves (TAC) present in time-resolved 2D-DSA sequences(101–103). This technique can be used to characterize intraprocedural changes in blood velocity in response to vascular intervention. The objective of this study was to determine the feasibility of using quantitative vascular imaging techniques, 4D flow MRI and qDSA, to characterize pre-, post-, and intra-procedural changes in hepatic arterial blood velocity in response to trans-arterial embolization (TAE) in an in vivo porcine model.

4.2 Methods

All procedures were approved by the institutional research animal care and use committee and were compliant with regulatory guidelines. Transarterial embolization was performed in the livers of eight swine (mean weight, 49.4 ± 2.0 kg). Subjects were sedated with an intramuscular administration of 7 mg/kg of tiletamine hydrochloride-zolazepam hydrochloride (Xyla-Ject; Phoenix Pharmaceutical, St. Joseph, Missouri), endotracheally intubated, and then underwent anesthesia induction and maintenance with 2% inhaled isoflurane (Halocarbon Laboratories, River Edge, New Jersey).

4.2.1 Trans-arterial Embolization

To help establish baseline hepatic flow states in swine, five of the eight patients completed 4D Flow MRI scans prior to trans-arterial embolization. Scans of the abdomen were acquired with a radially undersampled sequence, PC VIPR(50,51), on a clinical 3T system (Discovery MR750, GE Healthcare): imaging volume: 32x32x32 cm, acquired spatial resolution = 1 mm isotropic, VENC=50 and 100 cm/s, scan time: ~15 min; retrospective cardiac and respiratory gating. All eight of the swine were transported and imaged in an angiography suite (Artis zee; Siemens Healthineers, Forcheim, Germany) where femoral arterial access was obtained and the common hepatic artery selected with a 5 Fr angled glide catheter. A 3D-DSA was acquired to delineate hepatic arterial anatomy and were used to visually determine an optimal 2D projection angle for vessel layout. Prior to embolization, a 2D-DSA of the common hepatic artery was acquired using an injection of iohexol 300 mg/mL (Omnipaque 300; GE

Healthcare, Waukesha, Wisconsin) see Table 4-1 for imaging parameters. All DSA images were acquired with breath holds.

Animal	Artery Embolized	Embolization Type	Angiographic Endpoint	Projection Angle	Contrast Injection Rate	Contrast Volume	DSA (fps)
1	LMHA	Incremental	Sub-Stasis	0 deg	2.5 mL/s	15 mL	30
2	LMHA	Incremental	Sub-Stasis	0 deg	2.5 mL/s	15 mL	30
3	LMHA	Incremental	Partial-Stasis	30 deg LAO	2.5 mL/s	15 mL	30
	RLHA	Non-incremental	Sub-Stasis	30 deg LAO	2.5 mL/s	15 mL	30
4	LMHA	Incremental	Partial-Stasis	50 deg LAO	3.0 mL/s	18 mL	30
5	LMHA	Incremental	Sub-Stasis	0 deg	2.5 mL/s	15 mL	30
	RMHA	Non-incremental	Partial-Stasis	0 deg	2.5 mL/s	15 mL	30
6	LMHA	Incremental	Sub-Stasis	0 deg	2.0 mL/s	16 mL	30
7	LMHA	Incremental	Partial-Stasis	0 deg	2.0 mL/s	16 mL	30
8	LMHA	Non-incremental	Sub-Stasis	0 deg	2.5 mL/s	15 mL	30

Table 4-1: Details about the treatment and imaging protocol are given for all swine that participated in this study. A left medial hepatic artery embolization (LMHA) was completed for majority of swine, as it is the more well defined and dominate hepatic branch. In swine 3 and 4 we had to alter the projection angle to better layout the vessel of interest due to vessel overlap. A frame rate of 30 frames per second (fps) was used for all 2D DSA acquisitions.

The dominate hepatic lobe, typically the left, was embolized with two swine having both a right and left embolization. A complete list of embolization and imaging parameters can be found in table 1. Bland embolization, TAE, was performed with particles given that the primary objective of the study was to characterize variations in blood velocity and no tumors were present in this model. A 0.014" guidewire was used to select a second-order hepatic artery branch supplying the target lobe, after which a 2.8 Fr microcatheter was advanced into the vessel. Once the microcatheter was correctly positioned, an incremental or non-incremental embolization was performed using 100-300 um microspheres (Embosphere Microsphere; Merit Medical Systems, South Jordan, Utah) diluted in 10 mL of ioxhexol 300 mg/mL.

Incremental embolizations were performed in seven of the eight swine to generate velocity

reduction-embolization curves during a liver embolization. Incremental embolizations were performed in the left medial hepatic artery (LMHA). For incremental embolization, microspheres were typically delivered in 0.5-1 mL (up to 3 mL) aliquots with 2D-DSA imaging being performed before and after particle delivery. Additional particles were delivered until partial or sub-stasis endpoints were achieved. The level of stasis was determined by visual inspection of the 2D DSAs, with a decrease in antegrade arterial flow being categorized as partial stasis and minimal residual antegrade arterial flow being complete stasis. In the case of non-incremental embolizations, similar endpoints were achieved without the additional 2D DSA images during the embolization.

Three of the eight subjects had doppler wire (Volcano FloWire, Phillips) blood velocities acquired just distal to the catheter tip in the common hepatic artery (CHA) and embolized vessel pre- and post-TAE. Doppler wire measurements were made inside the vessel and no injections were completed during data acquisition. These swine were also transported back to the MR system for 4D Flow MRI scanning with identical parameters approximately 20 min after the embolization. Pre-, intra- and postembolization velocities in the target arteries were calculated using the qDSA and ccDSA methods as described below. A flow chart detailing the imaging protocol for the eight swine can be found in Figure 4-2.

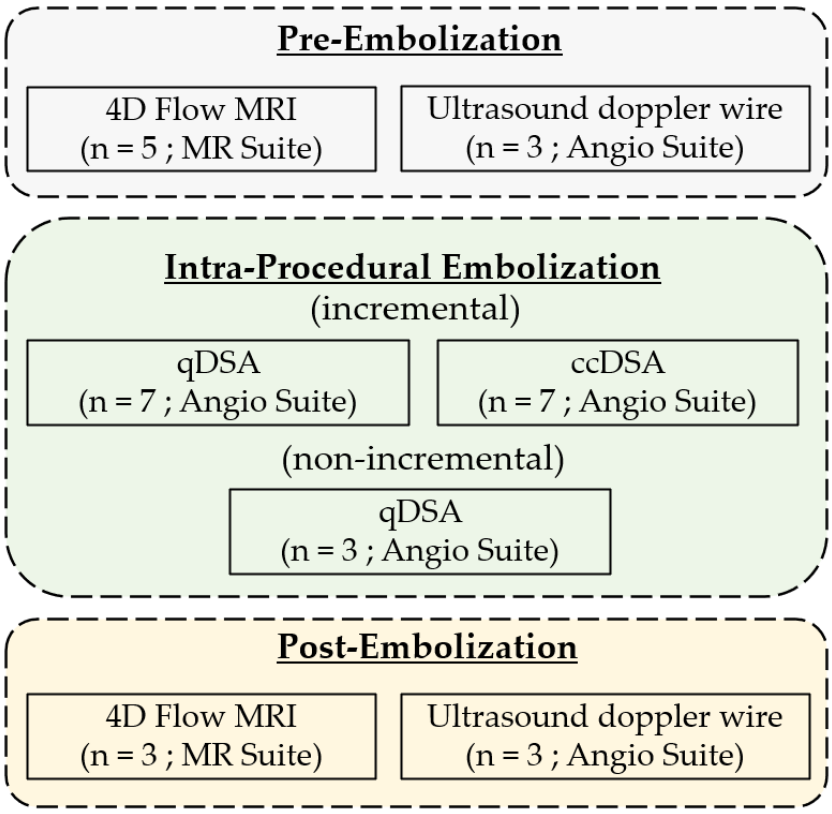

Figure 4-2: An outline of the quantitative imaging protocols completed are shown for the pre-, intra-, and post- procedural time points. The MR and US technique were used pre- and post- embolization, while the 2D DSA techniques were applied during the trans-arterial embolization. qDSA – quantitative digital subtraction angiography, ccDSA – color-coded digital subtraction angiography.

4.2.2 Post Processing

4D flow MRI angiograms and velocity vector maps were generated via offline time averaged reconstruction with cardiac and respiratory gating. The hepatic arterial networks were semi-automatically segmented from the PC angiogram using Mimics (Materialize, Brussels, Belgium), a commercial segmentation software. Ensight (Ensight 10.0.3 CEI, Apex, NC) was used for the visualization of vessel anatomy and placement of cross-sectional analysis planes: CHA, left hepatic (LH), left medial (LM), left lateral (LL), right hepatic (RH), right medial (RM), right lateral (RL), and gastroduodenal (GDA) arteries. Visualization of a representative hepatic angiogram and a 4D flow MRI angiogram can be found in Figure 4-3. These analysis planes were exported to a customized software package (stalder abstract) for dynamic manual vessel segmentation and hemodynamic analysis. Doppler wire velocities were analyzed with an

in-house software developed in MATLAB (R2018b Mathworks, Natick, MA) with the resulting values being average velocities. Velocity values from pre- and post- embolization were compared between MRI and US modalities to investigate baseline blood flow states and assess blood velocity changes related to TAE.

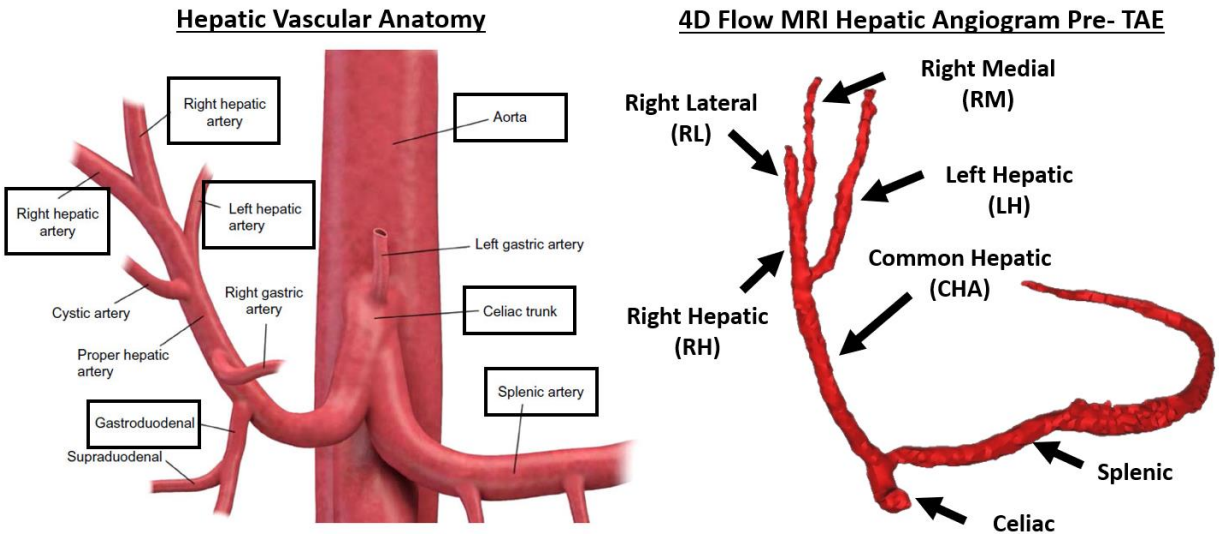

Figure 4-3: A detailed animation of abdominal arterial vasculature is displayed with major vessels being labeled. A 4D flow MRI was taken of the liver and all the detectable abdominal vessels are labeled with the associated animation vessels having the names boxed. The 4D flow MRI was able to capture up to 2nd order branches in the liver.

The intra-procedural 2D DSA blood velocity calculations relied on a qDSA method that uses inherent oscillations in the image contrast. The contrast oscillations are caused by the natural arterial flow pulsatility and can be used as a trackable marker of blood velocity in arteries. Centerline pixels of a vessel were automatically generated and used in the assessment of distances and temporal shifts in their TACs. The temporal shifts were calculated using a shifted-least squares approach (26) which has been shown to accurately estimate cranial velocities from 4D DSA acquisitions. The resulting velocities were spatially averaged and no magnification corrections were applied, thus the resulting values represented apparent blood velocity. An in vivo example of the TAC shift in a porcine model is illustrated in Figure 4-4. All qDSA calculations were completed with a custom-built MATLAB graphical user interface (MATLAB R2018b, MathWorks, Natick, Massachusetts). A commercially available ccDSA method (syngo iFlow, Siemens Healthineers) was used to calculate time-to-peak (TTP) in the embolized vessel for all the intra-

procedural 2D DSA scans. A similar region-of-interest was used for the qDSA and ccDSA techniques and an example of each method can be seen in Figure 4-4.

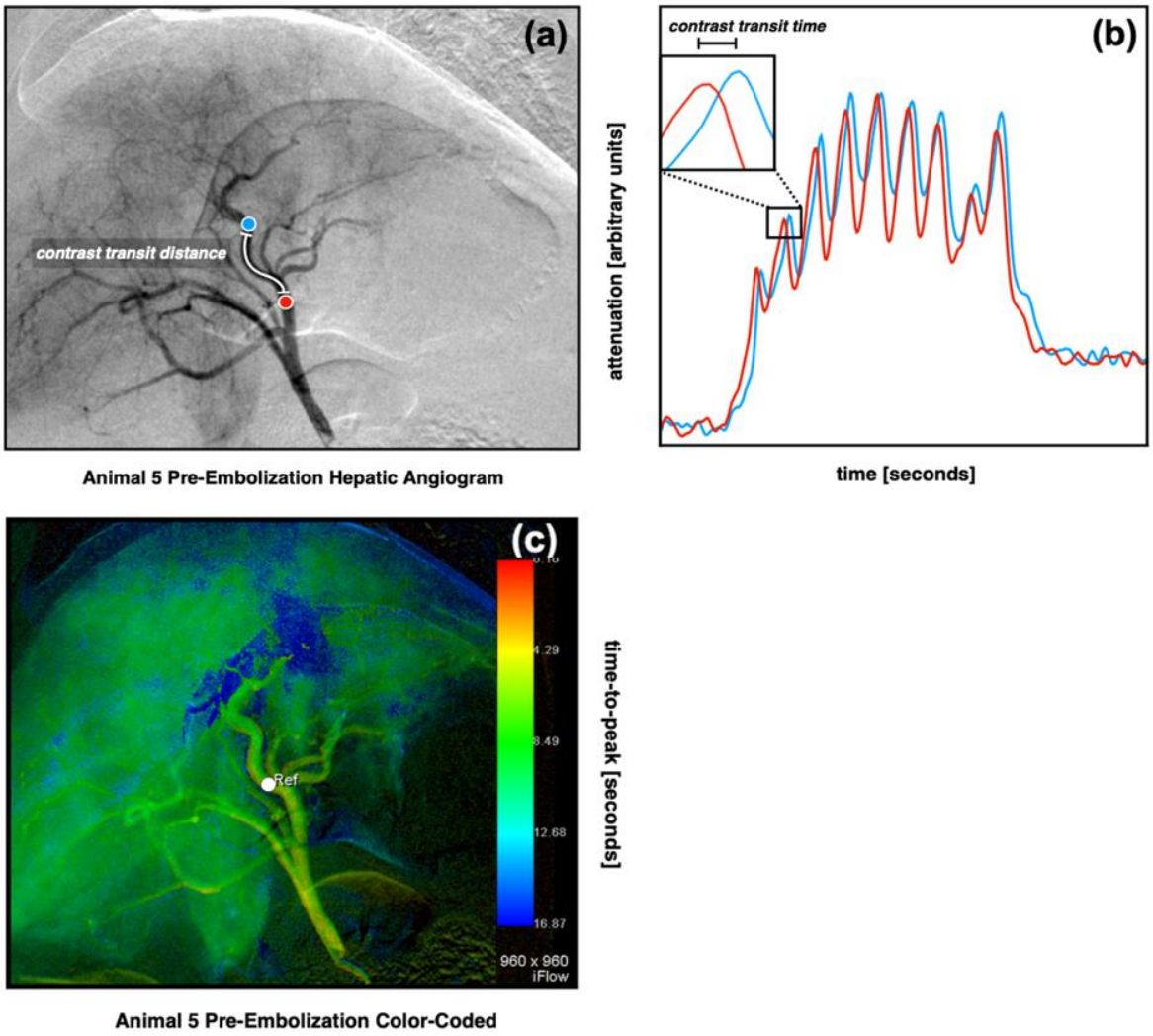

Figure 4-4: An example for each quantitative technique, quantitative DSA (qDSA) and color-coded DSA (ccDSA), is presented for a 2D DSA liver scan of a swine. The pre-embolization 2D DSA was acquired with a iodine contrast injection into the common hepatic artery. The qDSA technique relies on the spatial distance computed from a vessel centerline (a) and the temporal shift in the attenuation curves (b) to compute a relative blood velocity. The time-attenuations curves for the starting (red dot) and endpoint (blue dot) are shown in (b), with a zoomed window to emphasize the temporal shift between signals. A color-coded DSA (ccDSA) was generated from the 2D DSA (c) and color-encodes the image with time-to-peaks (TTP) values. A region-of-interest was selected in the same embolization vessel (white circle), with a diameter equal to the vessel diameter, was to be used for the comparison of variables between techniques. (Figure courtesy Sarvesh Periyasamy)

4.2.3 Statistical Analysis

To assess the baseline flow states in the hepatic vasculature of the swine, flow conservation of the first order and second order branches were compared to the common hepatic artery. The variation in velocities pre- and post- TAE, for MRI and US, were compared for three swine using the velocity percent change as the variable of interest. To compare the reduction in hepatic arterial blood velocity as a function of embolization level, sub-stasis vs partial-stasis, a linear mixed model was fit to the data using the 'lme4' package, where the individual animal was modeled as a random intercept. The mixed model p-values were calculated using Satterthwaite's approximation.

To assess the correlation between qDSA relative blood velocities and delivered volume of embolic particles, linear models were fit for each individual animal with the qDSA velocities being the dependent variable. From each model, the Pearson's correlation coefficient (r) the mean-squared error (MSE), and coefficient of determination (R2) were calculated. A lower MSE, higher R2, and a larger Pearson's r would lead to the best results for characterizing linear embolic flow reductions. The same models and metrics were calculated for the ccDSA time of arrival calculations and deliver embolic particles. To test if the MSE was lower when using the qDSA technique verse the commercially available ccDSA method, a one-sided, paired, Wilcoxon-rank sum test was used. The same test was used in the assessment of R2 comparisons between the qDSA and ccDSA techniques. To determine if the absolute correlation between qDSA and embolization was stronger than that of ccDSA, the paired, overlapping, correlation coefficients were tested using the methods described in Dunn and Clark (1969), at the animal level. The absolute correlation was used due to blood velocity decreasing as embolic particles increase and time of arrival increasing as embolic particles increase. For all tests a p-value less than 0.05 was considered statistically significant. All statistical analyses were done using R (V 3.6.1).

4.3 Results

4.3.1 Pre- and Post- Embolization

The pre- embolization average normalized MR flow for 1st order (LH+RH+GDA) and 2nd order branches (LL+LM+RL+RM+GDA), when being normalized to the 0th order branch (CHA), resulted in similar conservations of flow (1.11±0.35 and 0.92±0.3), respectively. The average hepatic flow values for each branch can be seen in Figure 4-5. The standard deviation of MR normalized flow values ranged from 30.5% in low order branches to 92.1% in high order branches. Velocity reductions were seen in the CHA for both the 4D Flow MRI and doppler wire measurements, with greater reductions occurring for sub-stasis embolization. Residual flow in the embolized vessel from the 2nd swine (RH), allowed for post-velocity percent reductions to calculated at 46.7% for MRI and 46.1% for doppler wire, as seen in Figure 4-6. qDSA relative hepatic arterial blood velocities for hepatic lobes that were embolized to sub-stasis angiographic endpoints had statistically significant larger reductions ($p < 0.01$) than the partial-stasis endpoints. A visual inspection of 2D DSA images was used to determine sub-stasis and partial-stasis endpoints and an example can be seen in Figure 4-7. Lobes embolized to partial-stasis had an average reduction in relative blood velocity of 45.2%±5.1% (n=4) when compared to baseline velocities. Lobes that were embolized to sub-stasis an average reduction in relative blood velocity of 22.4%%±12.2% (n = 6) when compared to baseline velocities. All the relative velocity reductions for partial and sub stasis are plotted in Figure 4-8.

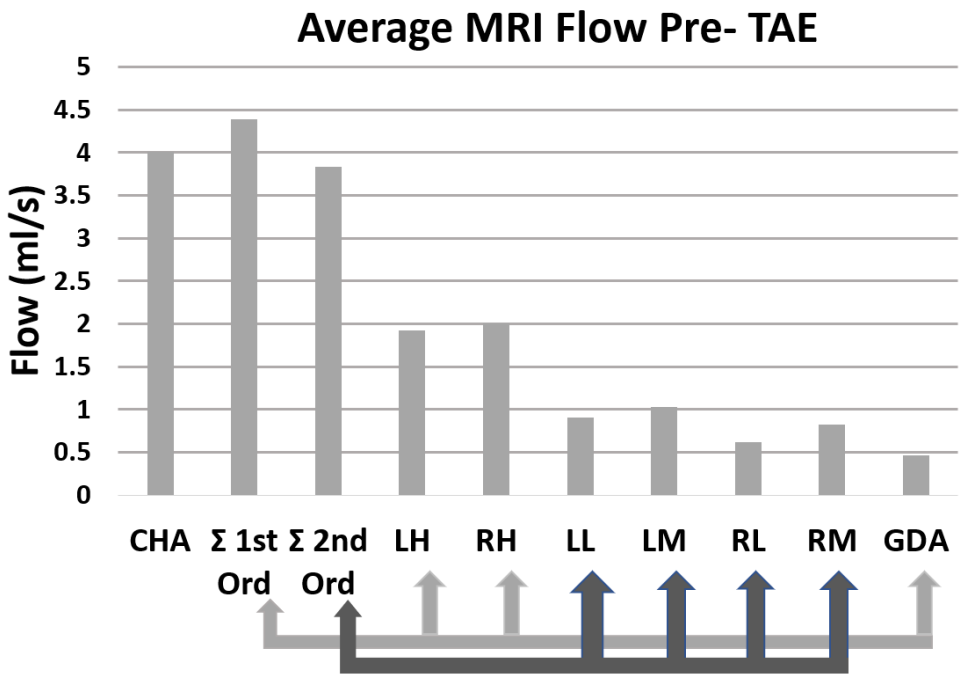

Figure 4-5: The average flow, utilizing 4D Flow MRI, was computed for all the hepatic arteries. The conservation of flow was computed for the 1st order and 2nd order branches and compared to the common hepatic artery(CHA). Conservation of flow for the 1st order and 2nd order branches showed good agreement to the 0th (CHA) order branch. CHA – common hepatic artery, LH – left hepatic artery, RH – right hepatic artery, LL – left lateral artery, LM – left medial artery, RL – right lateral artery, RM – right medial artery, GDA – gastroduodenal.

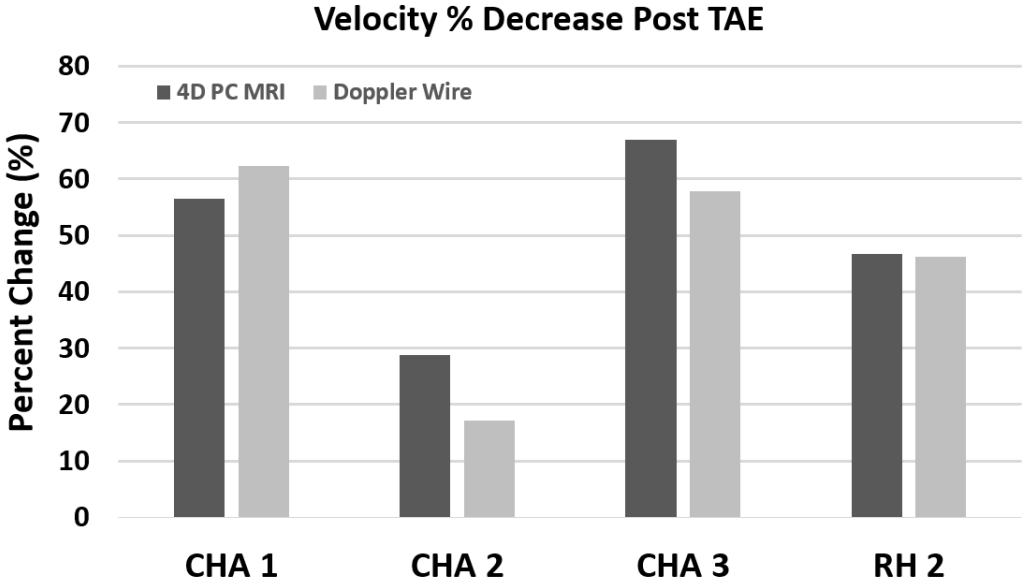

Figure 4-6: The percent blood velocity reductions for the common hepatic artery due to trans-arterial embolization are presented for both the MRI and US quantitative techniques. In the 2nd swine an embolization was completed to partial-stasis which allowed for the percent velocity reductions in the embolized vessel to be quantified. The average variation between MRI and US doppler wire reductions was less than 10%.

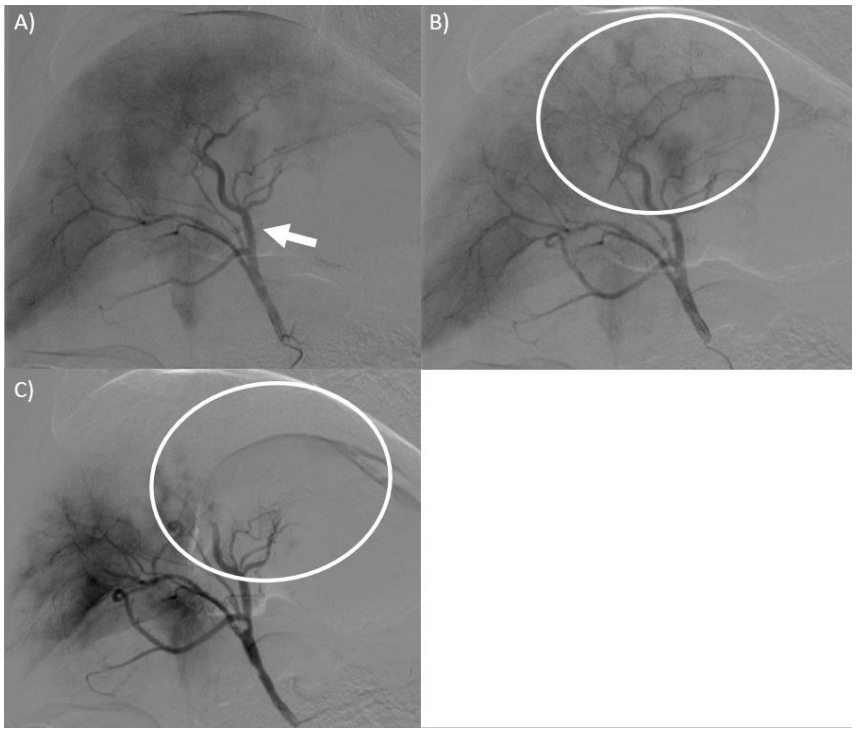

Figure 4-7: A representative 2D DSA image for pre- embolization (A), partial-stasis (B), and sub-stasis (C) is presented for a single swine case. The embolic particles were delivered in the left hepatic artery indicated by the arrow in (A). The affected region is bound by the white circle displayed on the partial- and sub- stasis images. A splotchy parenchyma pattern developed for the partial-stasis and little to no contrast reached the parenchymal region for the sub-stasis regions.

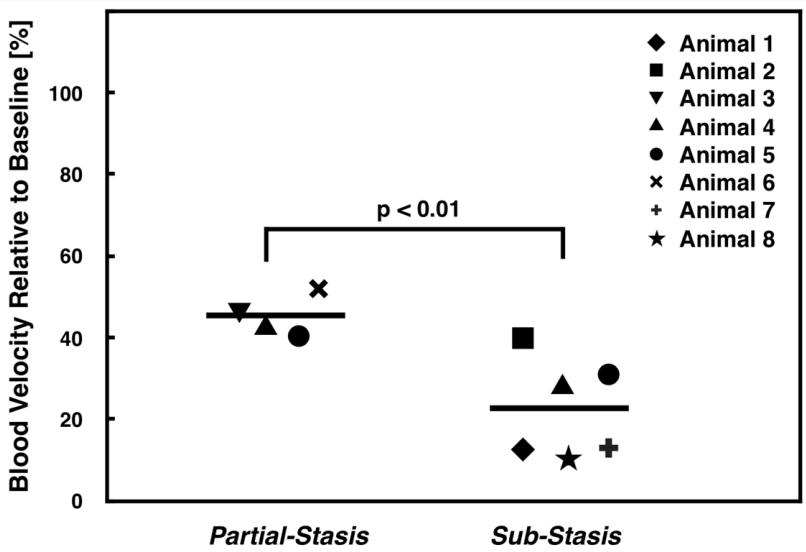

Figure 4-8: Post-embolization relative qDSA blood velocities were computed and grouped by partial or sub stasis. The determination of partial or sub stasis was completed through the visual inspection of the final 2D DSA images. There was a statistically significant reduction in relative blood velocity when comparing partial-stasis to sub-statis. (Figure courtesy Sarvesh Periyasamy)

4.3.2 Intra-procedural Embolization

In all the incremental embolizations, there was a negative linear relationship between the relative qDSA blood velocities and the volume of embolic particles delivered. For the commercially available ccDSA technique, there was a positive linear relationship seen in five cases when comparing the ccDSA time-to-peak (TTP) and the volume of embolic particles delivered, with the final two cases consisting of a negative slope. The linear fit parameters, correlation, MSE, and R^2, were compared between the relative qDSA blood velocities and ccDSA techniques. All fit parameters are reported for both qDSA and ccDSA in Table 4-2. The average correlation was -0.858 for qDSA and 0.359 for ccDSA. The correlation between qDSA and embolization was significantly greater than the correlation between ccDSA and embolization for animals 1 ($p < 0.05$), 3 ($p < 0.05$), 6 ($p < 0.001$) and 7 ($p < 0.05$). The average MSE for qDSA was 0.22, which was significantly smaller ($p < 0.01$) than the MSE for ccDSA, 0.62. The average R^2 for qDSA (0.75) was significantly larger ($p < 0.01$) than the R^2 for ccDSA (0.30). A representative incremental embolization from Animal 1 is presented in Figure 4-9.

Animal	Correlation		Mean Squared Error		R^2	
	qDSA	***ccDSA***	***qDSA***	***ccDSA***	***qDSA***	***ccDSA***
1	-0.96	0.70	0.08	0.46	0.92	0.49
2	-0.60	0.42	0.61	0.78	0.36	0.18
3	-0.87	-0.14	0.20	0.82	0.76	0.02
4	-0.85	0.59	0.23	0.55	0.72	0.34
5	-0.80	0.50	0.33	0.62	0.64	0.25
6	-0.98	-0.38	0.03	0.76	0.97	0.14
7	-0.94	0.82	0.10	0.28	0.89	0.68

Table 4-2: The fit parameters for all incremental embolizations are given for the quantitative DSA (qDSA) and color-coded DSA (ccDSA) techniques when compared to embolic particles delivered. The correlation, means squared error, and coefficient of determination (R^2) were used to investigate if a connection between a quantitative metric (relative blood velocity, time-to-peak) and embolic particle delivery could be made. Overall, the qDSA technique resulted in higher correlation coefficients, a lower mean square error, and a coefficient of determination closer to one.

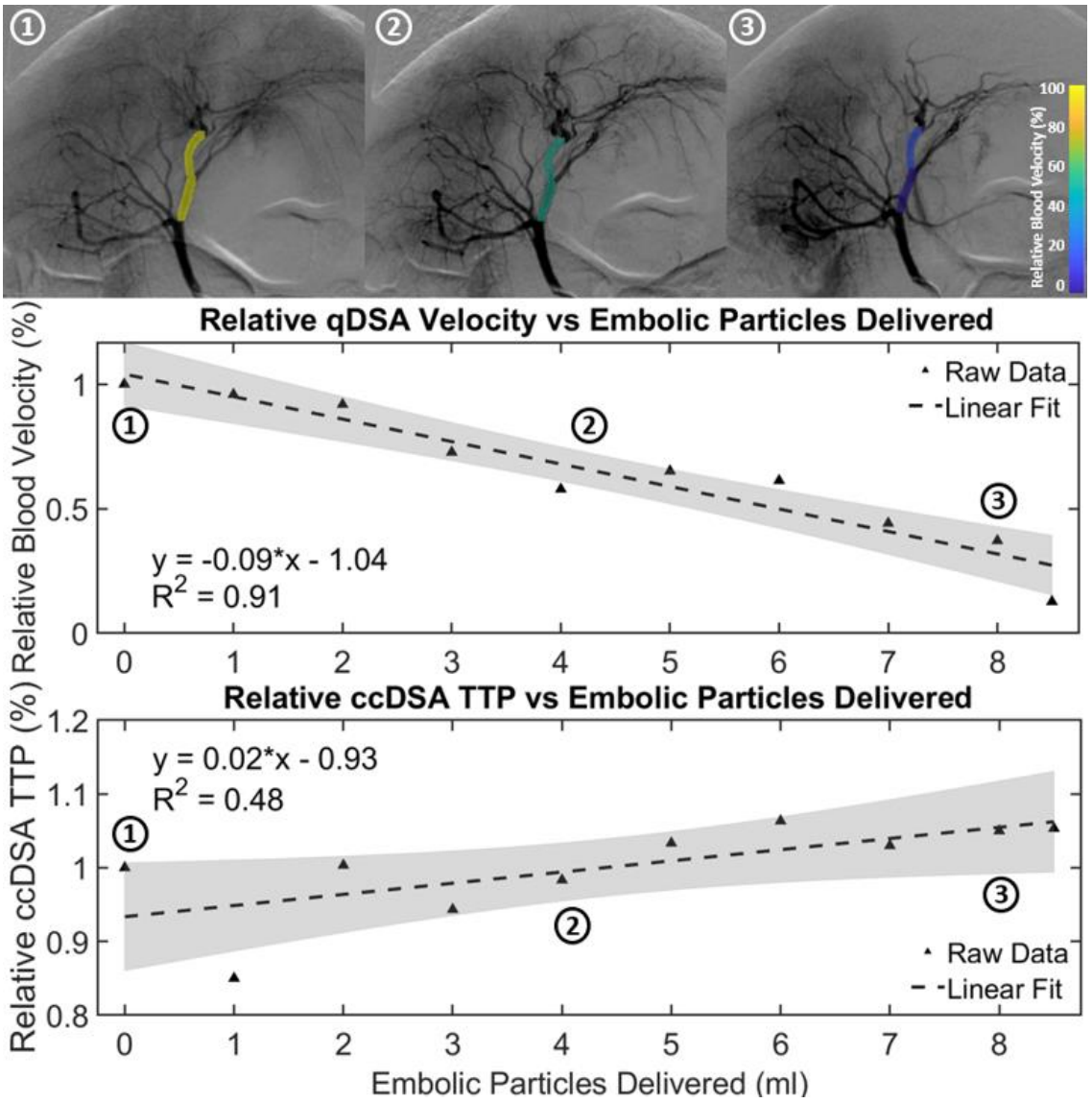

Figure 4-9: Relative velocity (qDSA) and TTP (ccDSA) reduction-embolization curves from an incremental embolization performed in the left medial hepatic artery in a porcine model. The three DSA images represent baseline (1), partial stasis (2), and sub-stasis (3) with the vessel of interest being color-coded with relative blood velocity percentage. A negative correlation is seen between the relative qDSA blood velocities and embolic particles delivered. There positive correlation between ccDSA calculated TTP and embolic particles delivered. The shaded regions represent the 95% confidence intervals for the fit estimations.

4.4 Discussion

The efficacy of trans-arterial liver embolization depends on achieving the appropriate degree of stasis in the target vasculature and tumor. Through the application of quantitative angiographic imaging, it may be possible to provide insight about the optimal procedural endpoints and evaluate the current subjective

endpoint techniques. Sub-stasis and partial-stasis endpoints have been used to provide favorable outcomes for patients undergoing TAE procedures(96). This work showed the feasibility of using 4D flow MRI, US doppler wire, and qDSA techniques for the evaluation of TAE procedures. These techniques were applied to pre-, post-, and intra- procedural time points, allowing for a complete overview of how quantitative blood velocity values could be applied to TAE procedures.

Embolizations performed to a greater degree of stasis, determined by visual inspection of 2D DSA, had a larger reduction in relative blood velocity as shown by 4D flow MRI, US doppler wire, and qDSA methods. For the embolizations performed in an incremental fashion, all vessels of interest exhibited a moderate-to-strong linear decreases in relative blood velocity, when computed with the proposed qDSA technique. The linear relationship between relative blood velocity reduction on qDSA and degree of embolization could play a critical role for determining the correct level of stasis for TAE. In addition, the technique could provide information to clinicians, during a procedure, about how many additional embolic particles should be delivered. qDSA may facilitate achieving standardized, reproducible, and objective endpoints during liver embolization given these results. The MR and US methods are viable techniques to assess the current subjective endpoints of TAE. Both methods showed quantitative reductions related to embolic procedures, with 4D flow providing the additional capability to assess vasculature changes in non-target organs.

In a controlled setting, qDSA demonstrated a stronger correlation with the degree of embolization than a commercially available color-coded technique (ccDSA). Techniques such as ccDSA, which utilized time-to-peak TTP, are more susceptible to variations in imaging parameters due to the limited spatial sampling(14,79,80). Variations in vessel morphology and catheter position may have contributed to the higher inter- and intra-procedural variability observed in the ccDSA calculations. Additionally, image artifacts caused by respiratory motion can introduce errors in TTP calculations, which can be lessened in the qDSA technique through spatial and temporal averaging. ccDSA was able to show consistent increases in TTP when viewing pre- and post- calculations but had a high degree of

variability for measurements computed during a procedure. The qDSA technique was able to provide relative blood velocities for all swine cases. The combination computing a spatially averaged blood velocity and utilizing temporal segmentation, allowed for outlier removal and the ability to avoid artifacts from motion. In all cases breatholds were used to reduce majority of the respiratory motion but some cardiac motion still remained in the images.

Attempts have been made to develop objective embolization endpoints using volumetric imaging techniques. MRI and CT techniques have been applied to pre-, post-, and intra-aterial perfusion(98,104,105), but are limited by procedural complexity and minimal peri-procedural assessment. 4D-DSA techniques have been recently shown to be feasible in the assessment of hepatic arterial blood velocities (72), which may allow for the quantification of velocities pre- and post- TAE. Standardization of this technique is still needed to allow widespread application. The addition of a 4D flow MRI could be applied with relative ease for pre- and post- procedural imaging as commercial software and scans are available through most major vendors. The 2D qDSA technique described is still investigative but could be easily translated to intra-procedural clinical workflows given minor modification to image acquisition parameters may be needed. A thorough investigation into reducing the patient dose and contrast load while maintaining quantitative abilities would be needed prior to clinical application. The software used for post-processing could be further optimized and adapted for clinical workstations to allow for quick computations and wider availability.

4.4.1 Limitations

This study had several limitations. First, TAE was performed in livers of non-tumor bearing swine, which approximates the hemodynamics of a human liver with HCC but would be altered when transitioned to a human model. The MRI spatial resolution allowed for majority of larger vessels to be captured but if smaller vessels are desired additional scan time would be needed, which could lead to non-feasible clinical scan times. The US system used for in vivo blood velocity measurements required manual manipulation of the wire to find optimal signal waveforms. The most consistent measurements were

found near the catheter tip, but additional studies would be needed to further investigate optimal wire locations. The qDSA method has technical limitations. The calculations presented were relative blood velocity rather than an absolute blood velocity as the magnification of the vessel due to 2D imaging was not considered. Additionally, a typical parameter used for in vivo imaging is blood flow instead blood velocity, which is what qDSA currently calculates. There is potential to use the vessel diameters seen in the 2D images to approximate cross-sectional areas, but this would require assumptions of spatial vessel information and require additional validations. Even without calculating the flow this study indicate that relative blood velocity changes could potentially be a surrogate for flow in the vessels we investigated. This may be due to the limited changes in vessel diameter seen along a vessel segment and the minimal changes in artery size throughout a TAE procedure. The shifted-least squares approach used in qDSA relies on adequate sampling in both the time and spatial domains which can be limited by the presence of short vessel sections or high blood velocities. With the addition of each aliquot of embolic particles, the contrast pulsatility seemed to diminish due to turbulent and retrograde flow, causing very low velocities in the presence of sub-stasis to become less robust. The qDSA method, however, was able to resolve a range of velocities that would be regularly encountered during interventions. Further work is necessary to resolve velocities at maximal and minimal flow states.

4.5 Conclusion

In conclusion, quantitative angiographic imaging techniques, 4D flow MRI, ultrasound, and qDSA, were able to quantify velocity reductions pre-, post-, and during liver embolization in a porcine model. The intra-procedural relative blood velocity reductions, calculated with qDSA, were found to be linear and correlated with visual assessment of sub-stasis and partial-stasis endpoints. Further work is needed to correlate changes in velocity from quantitative angiographic techniques with tissue-level response. This work highlights the potential benefits of having quantitative blood velocity metrics available pre-, post- and during TAE.

Chapter 5: Automated Post-Processing of Cranial 4D Flow MRI

5.1 Introduction

5.1.1 4D Flow Applications

Time-resolved, 3D phase contrast imaging with three-directional velocity encoding, often referred to as 4D flow MRI, allows for the non-invasive in vivo acquisition of dynamic, volumetric velocity vector fields. This data can be used to visualize angiograms and blood flow patterns via streamlines, as well as retrospectively analyzed for hemodynamics of any vessel within the imaging volume(13). Among other applications, 4D flow MRI has shown promise in evaluating, diagnosing, and characterizing a wide range of intracranial disease processes including aneurysms(106,107), arteriovenous malformations(108), dural arteriovenous fistulas(109), Alzheimer's Disease(110), venous drainage(111), and functional challenges(112).

The demands for spatial resolution are particularly high for the capture of the small and torturous cranial vasculature, especially when compared to the most commonly imaged vessel with 4D Flow MRI, the aorta(113). A well-suited approach for the demands of cranial imaging is the use of a radially-undersampled 4D flow MRI trajectory, termed PC-VIPR(50,51) (Phase Contrast Vastly-Undersampled Isotropic Projection Reconstruction). The radial sampling scheme offers several advantages over Cartesian acquisitions including: preserved spatial resolution while undersampling for scan time reductions, improved robustness to motion artifacts by oversampling central k-space(42), favorable noise properties for parallel imaging and regularized reconstructions(48), and flexible retrospective gating schemes(114). Advanced reconstruction methods have also been used to further accelerate imaging or to increase data fidelity(115).

5.1.2 4D Flow Post-Processing

Despite great advances in 4D Flow MRI acquisition and reconstruction, efficient and repeatable post-processing methods for cranial 4D flow MRI datasets remain a challenge. The high dimensionality of the reconstructed datasets (1 temporal, 3 spatial dimensions, and 3 velocity directions) and the complexity of the brain vasculature which often requires the simultaneous analysis of numerous vessels and can lead to prohibitively long post-processing times. Typical processing steps usually require manual vessel segmentation and manual placement of double-oblique tangent planes for hemodynamic analysis, approaches that are impractical when analyzing numerous vessels across a large number of datasets. User-dependent manual segmentation and plane placement also reduce the reproducibility of 4D flow MRI-derived hemodynamic parameters. Recently, a centerline processing scheme(CPS)(116) based analysis platform has been inroduced, which automatically segments the cranial vasculature and positions tangent planes along all vessel centerlines. This approach improved 4D flow intracranial post-processing times and robustness over manual analysis, enabling streamlined and reproducible processing in larger patient cohorts(110). However, limitations still exist in accurately selecting vessels due to the wide range of vessel sizes, tortuosity, and velocities present in the brain. Additionally, the segmentation techniques applied could be further improved upon due to the limitations of clustering techniques(117).

5.1.3 Study Motivation

Here we introduce a novel quantitative analysis tool (QVT), a post-processing analysis platform that further optimizes and advances the previously-established CPS to improve usability and repeatability of cranial 4D flow MRI analyses. Specifically, we (1) develop a novel, sliding threshold segmentation method optimized for cranial in-vivo imaging, (2) improve efficiency of vessel centerline generation, (3) create an interactive, 3D user-interface that allows for intuitive vessel selection and color map visualization of hemodynamic metrics (flow, area, etc.), and (4) reduce memory and storage requirements. These improvements allow for rapid, robust, and repeatable cranial 4D flow analyses while providing

users with an intuitive and user-friendly platform to visualize hemodynamic parameters across complex vascular networks.

5.2 Methods

5.2.1 Processing Scheme

All 4D Flow MRI data were acquired with a radially undersampled trajectory, PC VIPR(50,51). For each cardiac phase, 4 datasets were reconstructed offline: all three velocity directions and the magnitude averaged from all velocity encoded acquisitions. We utilize PC-VIPR in combination with parallel imaging acceleration techniques(47) to reduce scan times while preserving spatial and temporal resolution. The reconstruction pipeline included: PILS(47) (Parallel Imaging with Localized Sensitivities) reconstruction to reduce the spread of under sampling artifacts, Maxwell term phase offsets corrections(118), 4D Laplacian unwrapping to automatically correct for aliased voxels(119), and an automated 3rd-order polynomial background phase correction for eddy current phase offsets(120,121).

An angiogram was generated in the QVT by means of a novel sliding threshold algorithm applied to the time-averaged complex difference (CD) dataset(122). The CD dataset was normalized to a dynamic range from 0 to 1. Subsequently, the upper threshold for inclusion in the PC angiogram was varied from 0 (all voxels included) to 1 (only the voxel with the highest signal intensity included) in increments of 0.001 to record the number of voxels in the imaging volume below the varying threshold. This distribution was smoothed for noise reduction and the point of its maximum curvature was chosen as a global threshold. This threshold value was found to consistently preserve the vessel angiogram minimizing the inclusion of background voxels even in relatively high-noise datasets.

A vessel skeleton was created by use of a homotopic thinning algorithm(123) on the binary 3D global threshold angiogram, thereby, creating vessel centerlines with 1 voxel diameters. Dilation and thinning algorithms were used to automatically connect broken centerline segments and remove vessel spurs prior to vessel labeling. The QVT identified vessel endpoints and junctions, facilitating automated unique labels for each vessel branch. All branches were spatially smoothed using 3D spline interpolation

to improve orthogonal plane generation. A tangent vector, created using neighboring centerline points, was used to automatically generate orthogonal vessel planes for all centerline locations. A 13.8x13.8 mm plane (20x20 pixels) was used to ensure the large range of arterial and venous cranial vessel diameters were consistently encompassed while minimizing extravascular background signal. Vessel cross-sections were segmented using the sliding threshold method as discussed previously. However, for improved local segmentation, 2D input images were generated from a weighted sum of the complex-difference, velocity, and magnitude data. The local threshold was found at the point of maximum curvature from the distribution of weighted 2D vessel area as a function of threshold value.

With knowledge of the vessel boundaries in each analysis plane using the sliding threshold, vessel area and hemodynamic parameters, including mean and maximum velocity over the cardiac cycle, total volumetric flow rate, vessel area, pulsatility index(124), and resistivity index(125), were automatically calculated for all vessel segments and centerline points.. Total volumetric flow rates were defined as the mean velocity over the cardiac cycle multiplied by the time-averaged cross-sectional vessel area. To reduce noise in calculated parameters, quantitative values from the current and 2 proximal and 2 distal analysis planes were averaged.

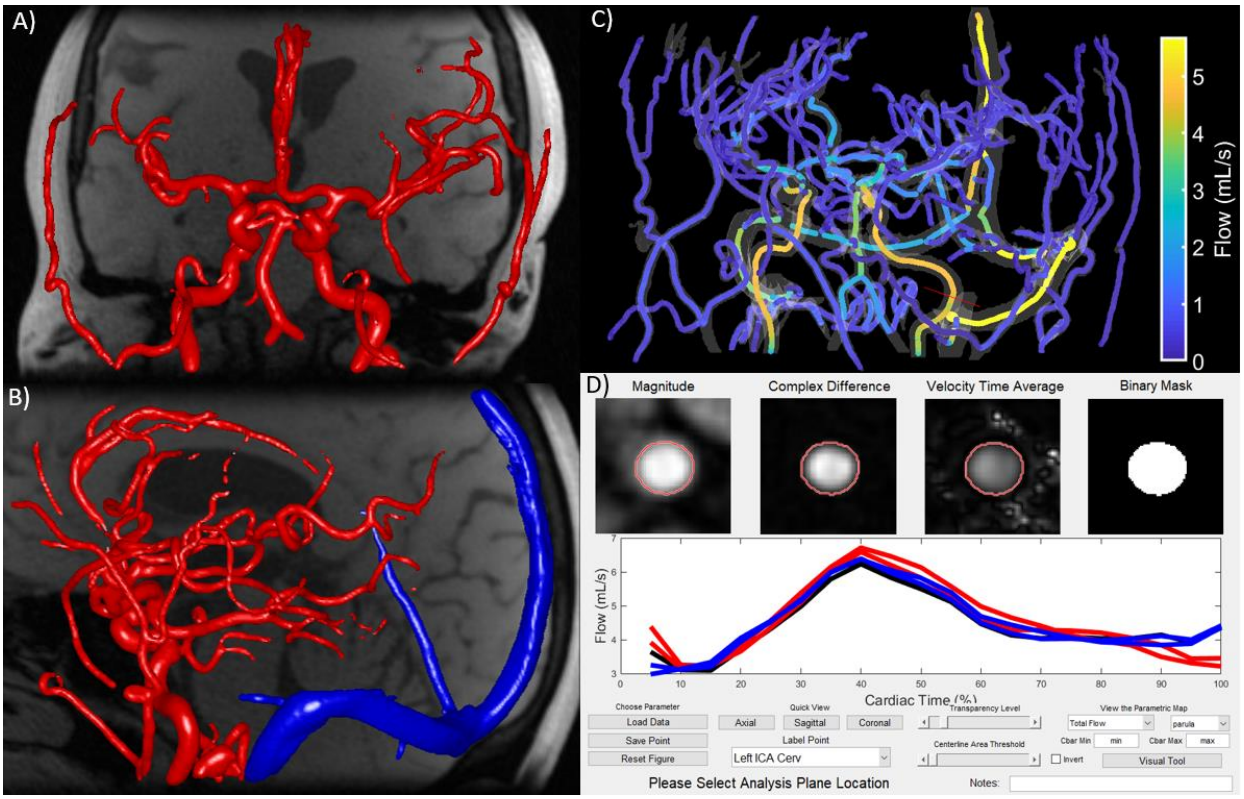

Figure 5-1: A) Coronal view of cranial arterial vascular anatomy B) Sagittal view of cranial arterial (red) and venous (blue) vascular anatomy. C) Quantitative velocity tool (QVT) display for automated vascular segmentation and color-coded centerline generation for interactive 3D vessel selection D) QVT control window that updates local segmentations and flow profiles as ROI is moved with options to adjust visualizations and save data.

Once all previously mentioned processes (angiogram generation, centerline generation, vessel labeling, cross-sectional segmentation, and hemodynamic parameter calculation) are automatically completed, the data is stored and loaded in the QVT graphical user interface (GUI) as shown in Figure 5-1. An interactive 3D interface is used to display the global angiogram and vessel centerlines, allowing the user to rotate, zoom, and pan the angiogram, and interactively select vessels (Figure 5-1A). To display quantitative parameters, vessel centerlines are color-coded with a hemodynamic parameter of choice (Figure 5-2). Global angiograms can be displayed superimposed on the vessel centerlines and visualized with varying degrees of transparency. Upon selecting a centerline point of interest from the 3D interface, 2D orthogonal images of the time-averaged magnitude, complex difference, through-plane velocity, and vessel segmentation mask, along with the flow over the cardiac cycle, are automatically updated in the

QVT GUI control window (Figure 5-1B). The QVT GUI control window allows the user to visually inspect the data and check image quality at the selected point prior to labeling and saving results. Additionally, a compressed MATLAB structure file containing all relevant data required to run the QVT is automatically saved to allow for fast reloading of 4D flow studies. A flow chart describing the post processing steps used to complete data reconstruction, analysis, and visualization can be seen in Figure 5-3.

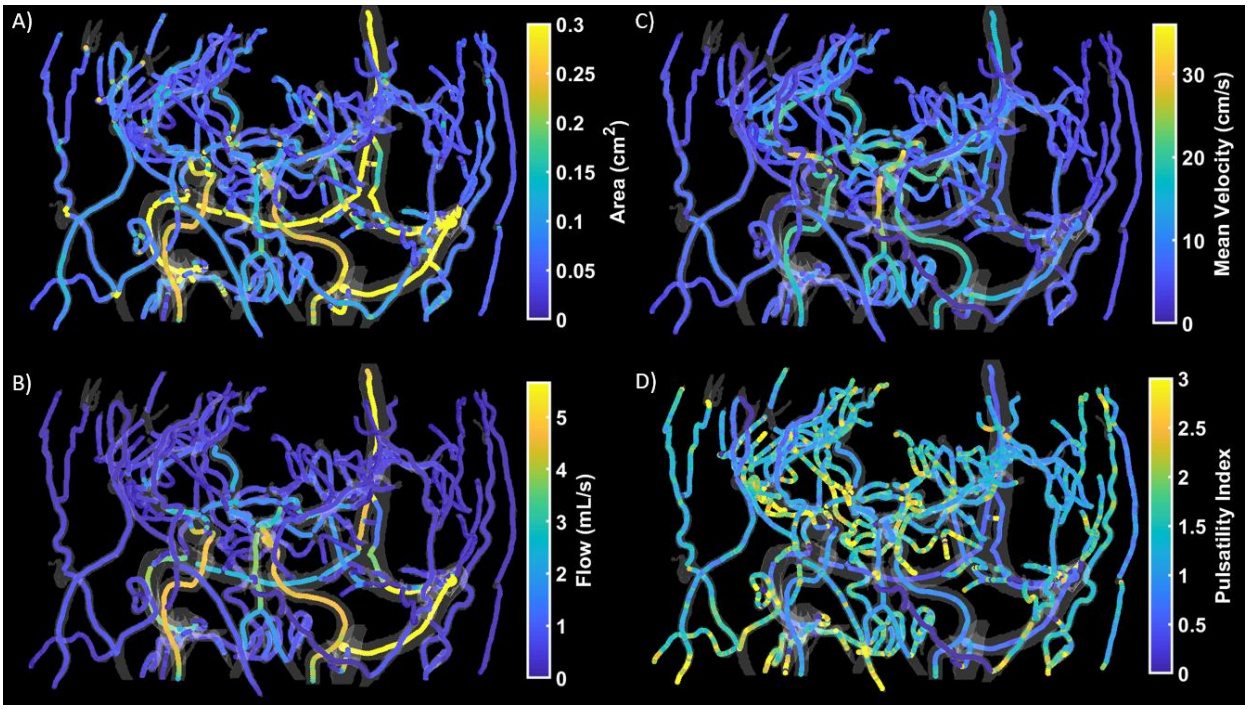

Figure 5-2: Color coded centerline displays for automatically computed hemodynamic parameters of area (A), flow (B), mean velocity (C), and pulsatility index (D). These displays allow the user to view a complex vascular network in a single image and visualize both local and global hemodynamic changes.

Optimal weighting coefficients, for the summed 2D cross-sectional vessel images, were determined by minimizing the differences between calculated vessel areas and manually segmented areas for 645 in vivo vessel locations from a total of 10 healthy subjects. The vessels used for this optimization consisted of both arterial and venous locations with a wide range of vessel sizes and velocities. Once the weighting was determined, these weights were used for segmentation in both the in vitro and in vivo studies. Optimization of the in vitro weights was not completed as it would be phantom dependent and

result in an unrealistically high magnitude weighting due to the silicon the background.

The quantitative velocity tool (QVT) was implemented in MATLAB 2018b (MathWorks, Natick, MA, USA) improving upon a previously established CPS(116). To assess workstation requirements, QVT analysis was completed independently with two desktop computer systems running Windows 10: (1) Dell Precision 5820 Tower, Intel Xeon W-2123 3.60 GHz CPU, 32 GB RAM and a (2) Dell Optiplex 9020, Intel Core i7-4770 3.40 GHz CPU, 16 GB RAM.

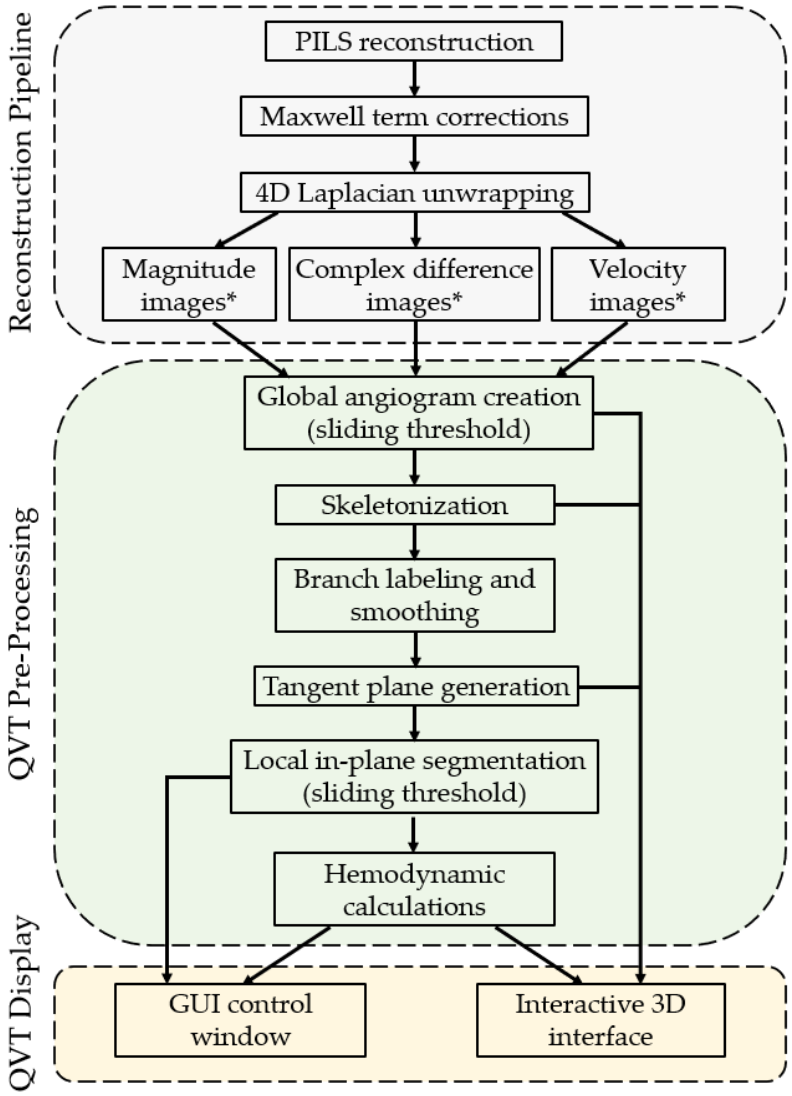

Figure 5-3: Flowchart describing the reconstruction pipeline, QVT pre-processing, and QVT display functionality. * Time-resolved and time-averaged datasets are produced via cardiac- and respiratory-gating. QVT – quantitative velocity tool, PILS - Parallel imaging with localized sensitivities, GUI – Graphical User Interface. [Flow chart courtesy of Grant Roberts]

5.2.2 In Vitro Validation

In vitro validation of the QVT was performed in a silicon-based arterial cranial flow phantom (Model H+N-R-A-002+, Shelley Medical Imaging Technologies, London, ON, Canada) to assess the quantification of area and flow in a controlled environment. A pulsatile displacement pump (Model PD-1100 BDC Laboratories, Wheat Ridge, CO, USA) was connected via distensible PVC tubing to the cranial flow phantom to form a closed loop system free of air. A pulsatile flow profile mimicking arterial blood flow, was produced at the pump outlet and maintained at a rate of 60 beats per minute. The fluid used for the experiment was gadolinium-doped water with 2 ml MultiHance (gadobenate dimeglumine) for 3 L of water. The dose was chosen to mimic clinical contrast concentration used in a 70 kg patient at 0.2 mmol/kg. Pulsatile waveforms were generated at five physiologically-realistic input flow rates (0.8, 0.9, 1.0, 1.1, and 1.2 L/min). Prior to MR imaging, a 0.25-inch non-intrusive ultrasonic flow sensor (PXL Clamp-On Flowsensor Transonic Systems Inc., Ithaca, NY, USA) was used to measure flow rates at the phantom's inlet and six outlets to ensure equal distribution of flow throughout the phantom. During 4D flow acquisitions, a 0.75-inch non-intrusive ultrasonic flow sensor (PXL Clamp-On Flowsensor Transonic Systems Inc., Ithaca, NY, USA) was placed at the pump outlet, well before the phantom input, to record and validate input flow rates.

A total of seven 4D flow scans were acquired from five flow rates, including two repeat scans performed at 1.0 L/min. 4D flow MRI was performed using a 3D radially-undersampled sequence (PC-VIPR(50,51)). Complete volumetric coverage of the cranial phantom was acquired with the following imaging parameters: TR/TE = 7.7/2.6 ms; tip angle = 8˚; number of projections = 11,000; reconstruction matrix= 320x320x320; acquired isotropic resolution = 0.69 mm^3; imaging volume = 22x22x16 cm^3; scan time = 5:40 min; encoding scheme = 4-point referenced; 3D golden angle sampling scheme. For all flow rates, velocity encoding sensitivity (V_{ENC}) was maintained at 80 cm/s. These parameters were chosen to be consistent with a currently used clinical 4D flow cranial protocol. Cardiac gating was recorded using an

MRI-compatible MR Finger (Shelley Medical Imaging Technologies, London, ON, Canada) that simulated the ECG waveform output directly from the flow pump. Cardiac time frames were binned retrospectively using our custom reconstruction pipeline based on the ECG signal. All MR scans were acquired on a clinical 3T Discovery 750 system (GE Healthcare, Waukesha, WI, USA) with a 32-channel head coil.

QVT was used for the assessment of all quantitative parameters derived from the acquired 4D flow MRI scans. Two segmentation methods, a k-means(126) (using the CPS(116)) and the sliding threshold approach (using the QVT), were evaluated for the analysis of area. Areas derived from these two segmentation methods were compared to CT-calculated areas, using CT areas as the reference standard. A high-resolution, 3D cone-beam CT of the phantom was obtained with a Siemens Artis zee biplane system using a Syngo DynaCT reconstruction (Siemens Healthineers, Forcheim, Germany). The scan parameters for the CT included: acquisition matrix = 512x512; resolution = 0.38 mm^2; number of slices = 488; slice thickness = 0.38 mm; field of view = 19.3x19.3x18 cm^3. Sufficient contrast existed between the surrounding silicon material and the air-filled vessels nullifying the need for iodinated contrast agents and avoiding potential air bubbles. Global thresholding followed by a manual segmentation was used to create the CT angiogram mask using Mimics software (Materialize, Brussels, Belgium). The CT angiogram was registered to the MR coordinate system in MATLAB 2018b using an intensity-based, regular-step gradient descent registration using mutual information as a similarity metric. For all scans, 29 vessel locations were selected and k-means (CPS) and sliding threshold (QVT) segmented areas were compared to the CT reference area for a total of 203 pairs of points (7 scans * 29 vessel locations). Vessel locations and the CT angiogram can be seen in Figure 5-4. A flow comparison between QVT-derived flow measures and a 0.75-inch ultrasonic flow sensor was completed, using the ultrasonic flow as the reference standard. The 4D flow MRI contained multiple inlets to replicate the cranial anatomy while the ultrasonic flow probe could only be used on the pump outlet. Thus, to compare flow values, the sum of flow from 3 vessels near the phantom inlet (shown in Figure 5-4) was compared against ultrasonic flow measures.

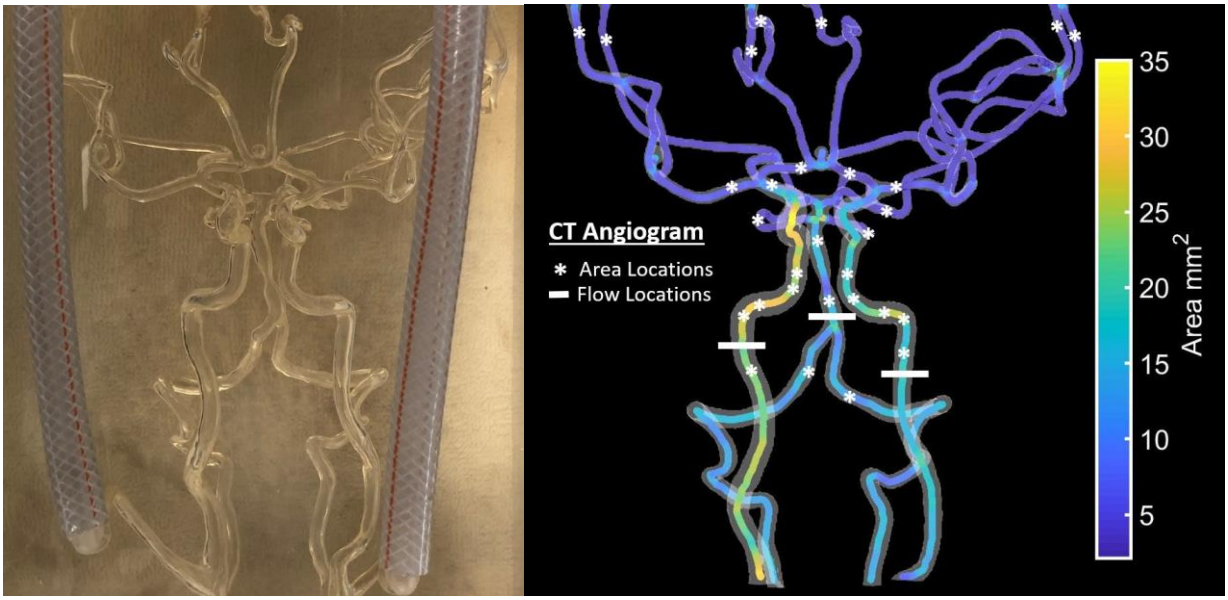

Figure 5-4: Left: Realistic cranial arterial model used for the for the phantom studies. Right: A CT angiogram used for the reference area measurements and to display locations for the area and flow calculations.

5.2.3 In Vivo Validation

In vivo validation of the QVT was performed on 10 healthy subjects (females: 8, mean age: 56.4 years, age range: 48-67 years) after informed patient consent and Institutional Review Board (IRB) approval. PC-VIPR scans were acquired on all subjects with the same magnet, coils, and scan parameters as the in vitro studies. Data reconstruction and corrections were kept consistent between in vitro and in vivo studies. QVT was used for the evaluation of area and flow parameters from the acquired 4D flow MRI scans. An area evaluation was completed with the two segmentation methods previously presented for the CPS (k-mean) and QVT (sliding threshold) methods. Both automatic segmentation methods were compared to ground-truth manually segmented vessels from arterial and venous vessel locations. A total of 13 vessel locations were selected from each patient: internal carotid arteries (ICA, 4 planes), basilar artery (1 plane), middle cerebral arteries (MCA, 2 planes), posterior cerebral arteries (PCA, 2 planes), straight sinus (SS, 1 plane), superior sagittal sinus (SSS, 1 plane), and transverse sinuses (TS, 2 planes). A total of 5 orthogonal planes were extracted from each location giving a total of 650 possible pairs of points. Quantitative segmentation comparisons were completed between the automatic and the manual

methods. Locations with a high degree of difficulty for accurate segmentation (tortuous vessels, slow velocities, multiple close vessels) were additionally selected for qualitative comparisons between the automatic CPS and QVT segmentation methods.

In vivo validation of QVT flow measurements was completed by assessing conservation of flow at junctions and along vessel segments using acquired 4D flow MRI data. A total of three arterial and venous vessel junctions were analyzed for each patient: ICA (arterial inlet), MCA (arterial outlet), and anterior cerebral artery (arterial outlet) for both the left and right sides; SSS (venous inlet), SS (venous inlet), and left and right TS (venous outlets). Flow along a vessel was measured at every 5^{th} point along the vessel centerline for three vessels: left ICA, right ICA, and SSS. Flow values used in the analysis of conservation of flow along a vessel were normalized by the mean and converted to a percentage from the mean. This was completed to allow quantitative flow values from different ranges and magnitudes to be compared equally. For all flow analyses, flow from the 4 neighboring planes (surrounding the current point) and the current point were averaged.

A comparison of vessel selection and post-processing times was performed by 2 researchers with over 3-years of experience in MR flow image processing using 16GB and 32GB RAM computers, respectively. Vessel selection and post-processing times were compared between the CPS and QVT methods for the 13 in vivo vessel locations previously mentioned. If the vessel of interest was not present or selectable, the vessel was recorded as missing. Interobserver repeatability was assessed using measures of mean flow, acquired with the QVT method, at all vessel locations for each subject. Vessels that were not selectable were excluded from the interobserver analysis. Post-processing times for angiogram generation, data loading, quantitative vessel selection, and total case analysis were measured with both computers and both post-processing methods.

5.2.4 Statistical Analysis

To assess the accuracy of 4D flow MR relative to reference standards in an arterial cranial phantom, linear regression was used for the following comparisons: (1) CPS segmented vessel areas vs. CT areas, (2) QVT segmented vessel area vs. CT areas, and (3) QVT flow vs. ultrasound flow. To assess the accuracy of 4D flow MR in vivo, linear regression was used for the following comparisons: (1) CPS areas vs. manually segmented areas, (2) QVT areas vs. manually segmented areas, and (3) QVT flow at junction inlets vs. QVT flow at junction outlets. Associated model p-values, 95% confidence intervals (CI) and Pearson's correlation coefficient (r) were calculated for each linear regression model. Conservation of flow along a vessel was assessed by fitting the percent flow variation for all vessels to a gaussian curve using a minimum variance unbiased estimator and providing the 95% CI for the estimated parameters (mean and standard deviation). To analyze segmentation performance in vivo, an average Dice coefficient was computed between k-means (CPS) and sliding threshold (QVT) segmentations relative to ground-truth manual segmentations. Interobserver repeatability for flow measurements with the QVT method were calculated using a Bland-Altman analysis(127). Paired t-tests were used to compare post-processing times between the 16GB and 32GB RAM computers and the CPS and QVT post-processing methods. For this study, a p-value < 0.05 was considered statistically significant. All statistical analyses were done using MATLAB 2018b.

5.3 Results

4D flow reconstructions, including additional data corrections, were completed automatically in approximately 1 hour. All ECG gating files used for accurately binning the time-resolved data did not contain significant variations in heart rates. Visual inspection of local cross-sectional planes used for analysis, both in vitro and in vivo, showed no visible aliasing artifacts and included all relevant vasculature. All reconstructed data was automatically post-processed and analyzed successfully with the QVT. Optimized weighting values for the weighted sum cross-sectional plane, generated from the complex-difference, velocity, and magnitude data, were 0.6, 0.2, and 0.2, respectively. These weights

were used for both the in vivo and in vitro experiments.

5.3.1 In Vitro Validation

The pulsatile pump's average flow rates were measured at the pump outlet, during the 4D Flow scans, and ranged from 0.82 – 1.21 L/min, which were within the desired physiologically blood flow limits. Pulsatile flow was visible in both the ultrasound probe measurements and throughout the phantom vasculature as visualized by the QVT. Linear regression between k-means (CPS) and CT-segmented areas was calculated and plotted. The resulting linear regression equation was: ACPS = 0.71*ACT + 4.35 (in units of mm2), where ACPS is the automatic k-means segmented area and ACT is the manual CT segmented area. The 95% CIs for the slope and intercept were [0.68,0.74] and [3.93, 4.77], respectively. Linear regression between sliding threshold (QVT) and CT segmented areas was calculated and plotted. The resulting linear regression equation was: AQVT = 1.03*ACT + 3.51 (in units of mm2), where AQVT is the automatic sliding threshold segmented area. The 95% CIs for the slope and intercept were [0.99,1.07] and [2.91, 4.11], respectively. A very strong correlation between the variables was observed for both the CPS and QVT segmentation methods (CPS: $r = 0.95$, $p<0.001$; QVT: $r = 0.95$, $p<0.001$). Linear regression between QVT-derived flow and ultrasound flow was calculated and plotted. The resulting linear regression equation was: FQVT = 0.98*FUS + 0.05 (in units of L/min), where FQVT is the QVT 4D MR flow and FUS is the ultrasound flow measured at the pump outlet. The 95% CIs for the slope and intercept were [0.74,1.22] and [-0.20, 0.29], respectively. A very strong correlation between the variables was observed for quantitative flow ($r = 0.96$, $p<0.001$). Linear regression plots for all in vitro comparisons are shown in Figure 5-5.

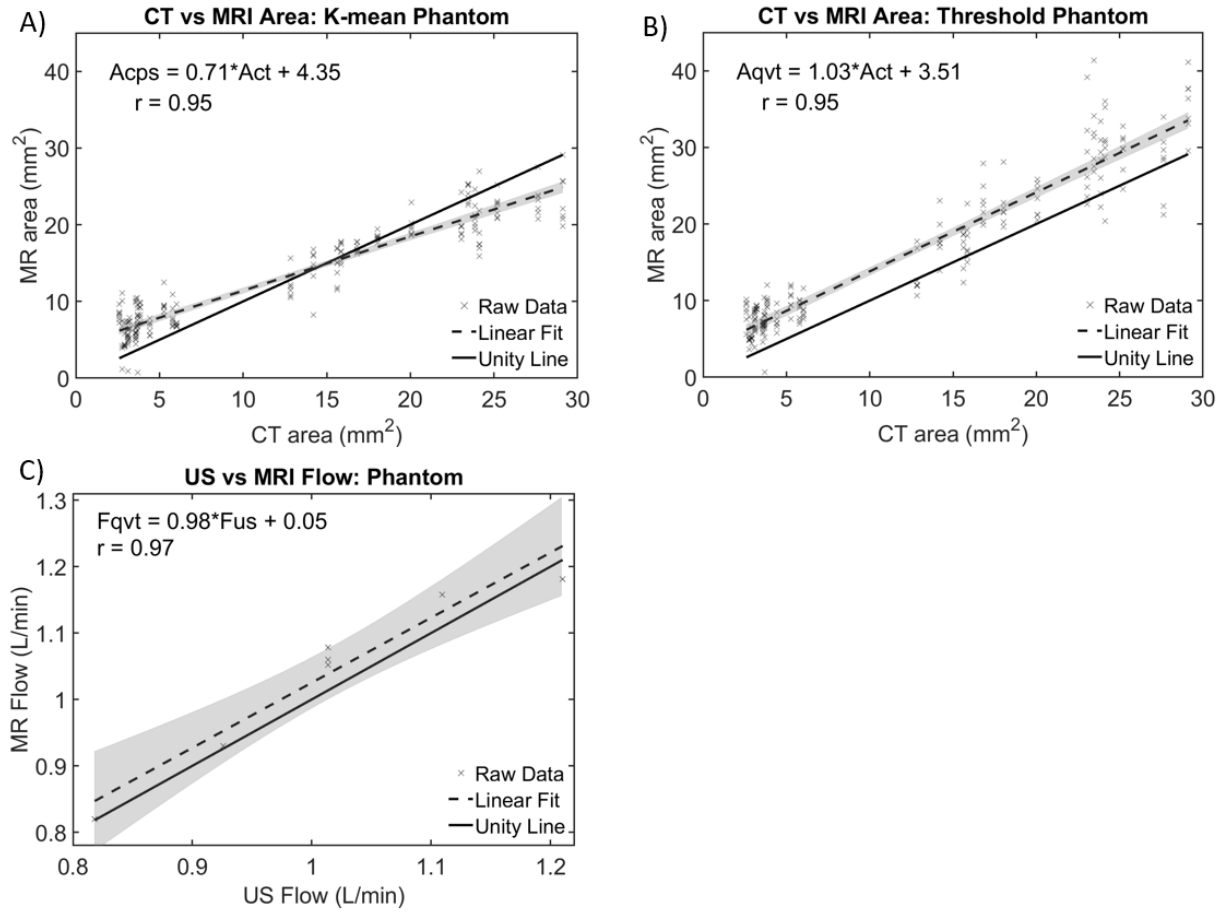

Figure 5-5: Linear regression for the segmentation techniques used in the centerline processing scheme (CPS) and the quantitative velocity tool (QVT) are displayed in A) and B) for the phantom experiments. Both techniques were highly correlated to areas calculated from a high-resolution CT with the QVT method giving a slope closer to unity. Linear regression of the QVT flow and the ultrasonic flow probe C) showed a strong correlation with a slope near unity for the phantom experiments.

5.3.2 In Vivo Validation

Linear regression between k-means (CPS) and manually segmented cross-sectional areas from the 4D flow MRI was calculated and plotted. The resulting linear regression equation was: $A_{CPS} = 0.61 * A_{MAN} + 0.38$ (in units of mm^2), where A_{CPS} is the automatic k-means segmented area and A_{MAN} is the manual segmented 4D flow MRI area. The 95% CIs for the slope and intercept were [0.60,0.63] and [0.08,0.68], respectively. Linear regression between sliding threshold (QVT) and manually segmented cross-sectional areas from the 4D flow MRI was calculated and plotted. The resulting linear regression equation was: $A_{QVT} = 0.93 * A_{MAN} - 0.00$, (in units of mm^2), where A_{QVT} is the automatic sliding threshold segmented

area. The 95% CIs for the slope and intercept were [0.92,0.95] and [-0.44, 0.43], respectively. A very strong correlation between the variables was observed for both the CPS and QVT segmentation methods (CPS $r = 0.96$, $p<0.001$; QVT $r = 0.96$, $p<0.001$). Linear regression between the inlet and outlet flow from vessel junctions was calculated and plotted. The resulting linear regression equation was: $F_{IN} = 1.05*F_{OUT} - 0.21$ (in units of mL/s), where F_{IN} is the total QVT inlet flow and F_{OUT} is the total QVT outlet flow. The 95% CIs for the slope and intercept were [0.98,1.13] and [-0.68, 0.26], respectively. A very strong correlation between the inlet and outlet flow was observed ($r = 0.98$, $p<0.001$). Flow values along a vessel were converted to a percentage from the mean and plotted in a histogram to assess variation of flow along single vessel segments. The histogram gaussian curve fit resulted in a mean and standard deviation of 9.33e-16 [95% CI: -0.35,0.35] and 3.05% [95% CI: 2.82,3.31], respectively. Linear regression and histogram plots for in vivo area and flow comparisons can be viewed in Figure 5-6.

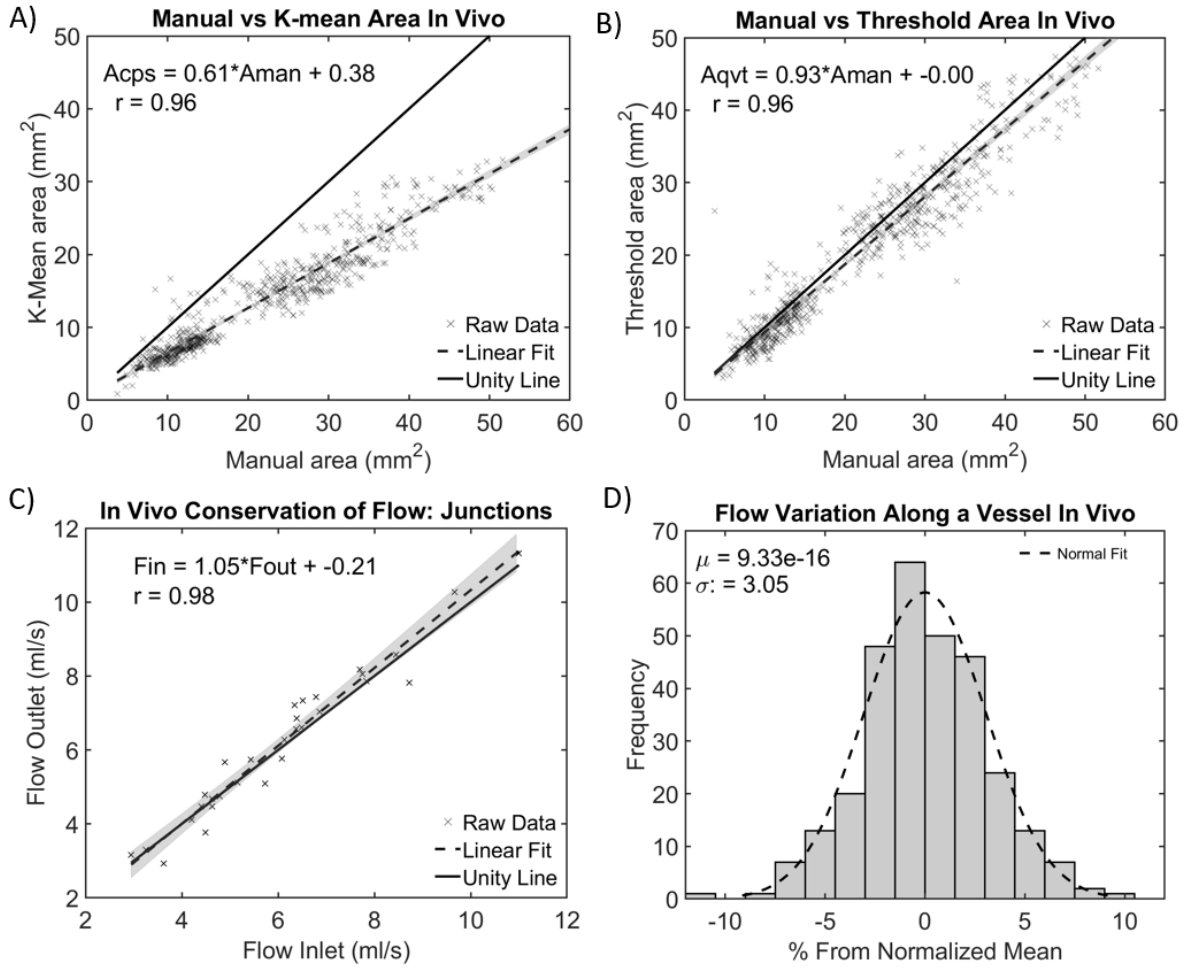

Figure 5-6: Linear regression for the segmentation techniques used in the centerline processing scheme (CPS) and the quantitative velocity tool (QVT) are displayed in A) and B) for the in vivo experiments. Both techniques were highly correlated to areas manually segmented from the acquired 4D flow data sets with the QVT method giving a slope closer to unity. Linear regression of the conservation of flow at junctions C), using the QVT method, showed a strong correlation with a slope near unity for the in vivo scans. The normalized percent variation of flow along a vessel D) resulted in a gaussian distribution with a mean of 9.33e-16 and a standard deviation of 3.05.

A total of 645 cut-planes (1 missing transverse sinus) were successfully segmented manually for comparison. Dice coefficients were used to assess the similarity between automatic and manual segmentations. Average Dice coefficients for k-means (CPS) vs. manual segmentation and sliding threshold (QVT) vs. manual segmentation were 0.77±0.07 and 0.91±0.06, respectively. Several illustrative examples of the differences between the two segmentation methods are shown in Figure 5-7. The percentage of missed vessels from the desired 13 was 16.2% for the CPS and 3.8% for the QVT methods. Small vessels and vessels with slow flow, namely the MCA, PCA, and TS, accounted for the

majority of missed vessels. Bland-Altman analysis of interobserver repeatability for QVT flow quantification demonstrated a mean bias of 0.042 ml/s with 95% limits of agreement of [-0.37, 0.45] ml/s seen in Figure 5-8. Average post-processing times for angiogram generation, data loading, quantitative vessel selection, as well as total case analysis times, are given in Table 5-1 for both methods (CPS and QVT) and computers (16G and 32G RAM). All comparisons between post-processing times were found to be statistically significant except for angiogram generation (CPS: $p = 0.53$) and quantitative vessel selection between (CPS: $p = 0.38$; QVT: $p = 0.15$) the 16GB and 32GB computers, as seen in Figure 5-9.

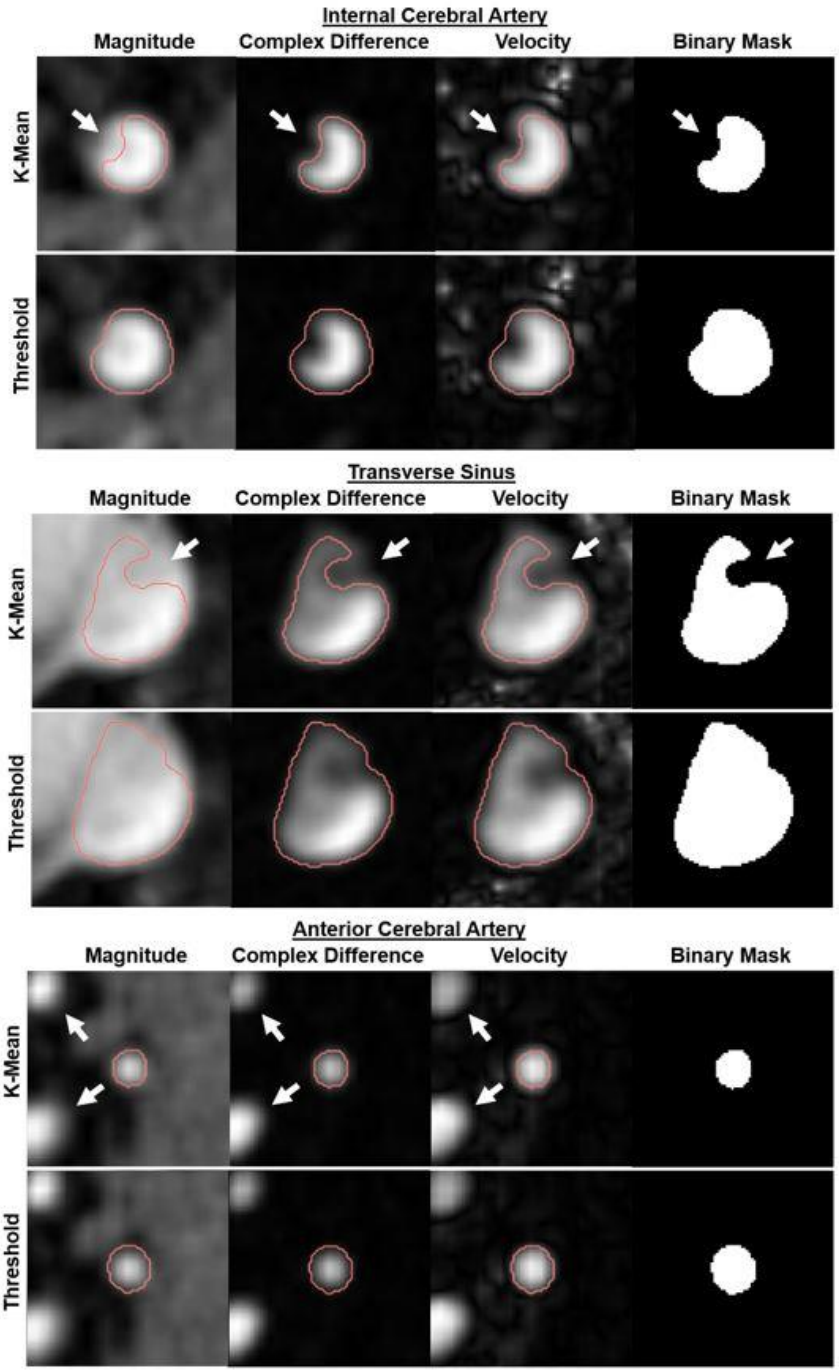

Figure 5-7: Segmentations were completed for both methods, k-mean and sliding threshold, on the curve of an internal cerebral artery (top), in a transverse sinus (middle), and in an anterior cerebral artery (bottom). In all cases, the sliding threshold technique outperformed the k-mean segmentation. Arrows were placed in the images to indicate the potential sources of error related to slow flow or other vessels present in the region of interest.

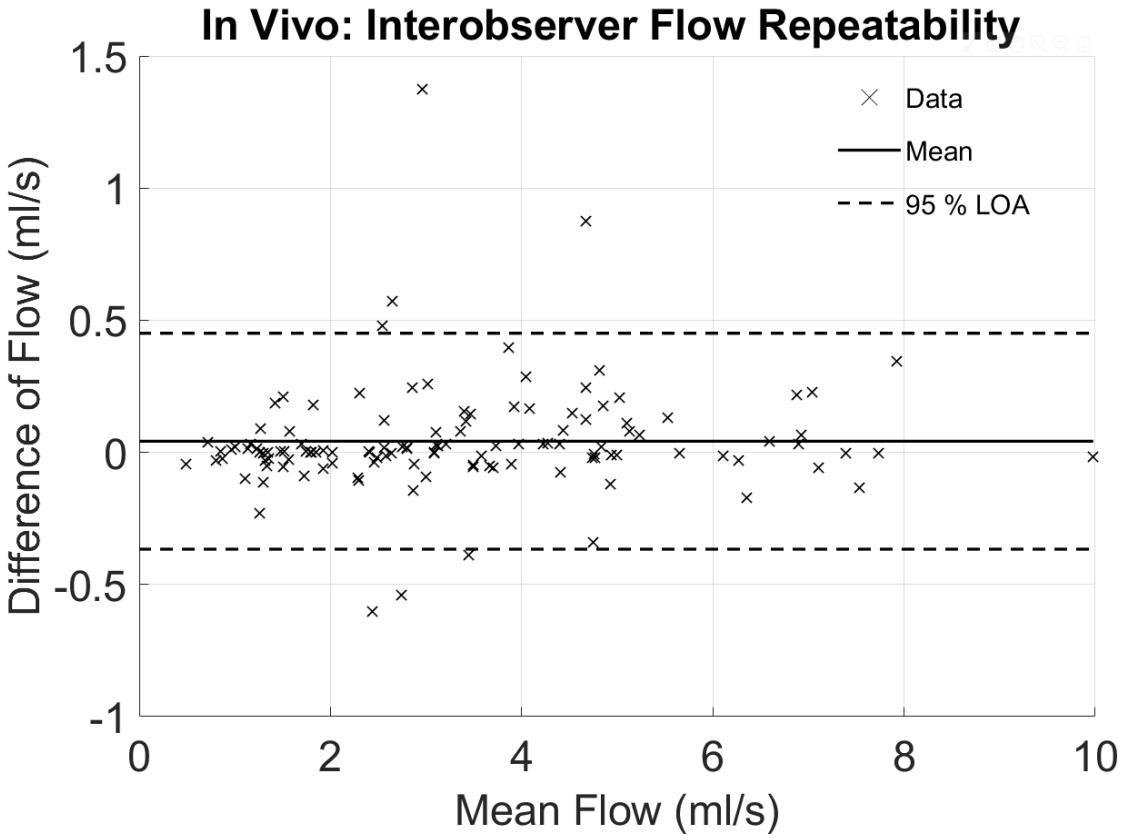

Figure 5-8: Ten cranial cases were post processed using the quantitative velocity tool (QVT) by two independent users. A total of 13 vessels were desired for each patient and the resulting flow values were compared using a Bland-Altman analysis showing mean bias of 0.042 ml/s with 95% limits of agreement of [-0.37, 0.45] ml/s.

Table 1: Post-Processing Times for CPS and QVT Methods

Method	RAM (GB)	Angiogram (min)	Load Data (min)	Vessel Select (min)	**Total Case (min)**	**Per Plane (min)**
CPS	16	0.80 ± 0.15	3.43 ± 0.21	14.8 ± 2.75	**19.1 ± 2.76**	**1.14 ± 2.58**
CPS	32	0.82 ± 0.14	1.02 ± 0.18	15.6 ± 3.36	**17.5 ± 3.36**	**1.20 ± 3.20**
QVT	16	0.24 ± 0.02	6.06 ± 0.54	5.28 ± 0.58	**12.4 ± 0.79**	**0.41 ± 0.68**
QVT	32	0.20 ± 0.02	2.34 ± 0.42	4.71 ± 0.88	**7.94 ± 0.98**	**0.36 ± 0.97**

Table 5-1: The centerline processing scheme (CPS) and quantitative velocity tool (QVT) were used for the analysis of ten 4D flow cranial scans. The post processing times were recorded for both techniques with machines of 16 GB and 32 GB RAM. A reduction in post processing times was seen when using the QVT method for angiogram generation, vessel selection, and total case times. The per plane column indicates on average the amount of time that was needed to select a vessel location, validate accurate segmentation, and check the pulsatiliy.

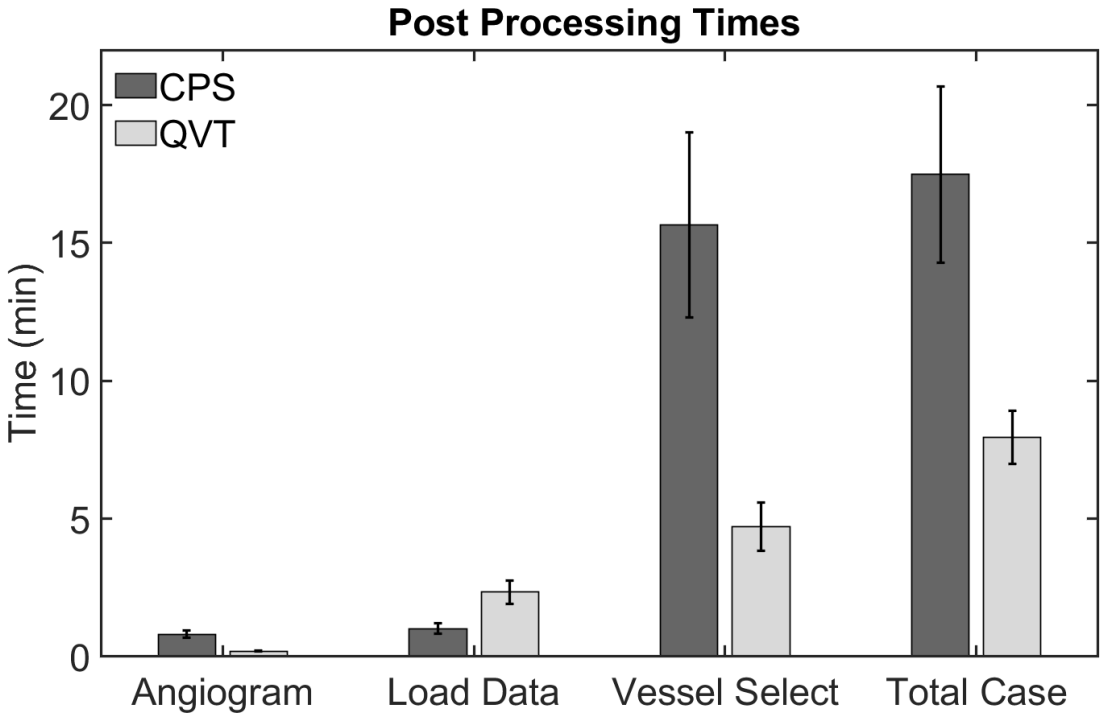

Figure 5-9: The post processing times for the centerline processing scheme (CPS) and the quantitative velocity tool (QVT) were compared for angiogram generation, loading data, vessel selection, and the total processing time. The QVT reduced the time needed to complete a cranial analysis of 13 vessel locations. An increase in loading time was due to additional corrective algorithms applied prior to vessel selection.

5.4 Discussion

This paper presents a quantitative velocity tool (QVT) that allows for automated quantitative analysis of hemodynamic parameters and easily interpreted 3D visualizations generated from cranial 4D flow MRI. The accuracy and repeatability of quantitative metrics derived from the QVT, specifically vessel area and flow, were validated both in vitro and in vivo. Additionally, this tool provides a unique, interactive 3D visualization tool that can simultaneously display anatomic and color-coded quantitative vascular information while also allowing a user to visualize data from cut-planes and flow profiles on a point-by-point basis. Combined, these features allow for quick, repeatable, and robust analyses to investigate hemodynamic parameters throughout the brain, which would otherwise be difficult and time-consuming to perform using alternative post-processing software or flow-sensitive imaging techniques. Furthermore, the improvements in automated nature, accuracy, and time savings can help not only in the research settings, but also may make the application of 4D flow MRI more widely available in the clinical setting.

Quantitative 4D flow MRI-derived parameters, such as flow, average velocity, pulsatility index, and resistivity index, depend upon the accurate segmentation of vessel cross-sections. Previous studies have utilized automatic segmentation methods, including global thresholding(128), clustering(126), and local thresholding(117) to help improve the repeatability and accuracy required for clinical use. In this paper, we presented a novel, sliding threshold segmentation methodology that provided accurate and efficient global segmentation (for centerline generation) and in-plane segmentation (for vessel area and flow analysis). While both k-means and sliding threshold segmentation techniques were highly correlated to reference standards for in vitro and in vivo studies, linear regression and Dice coefficients indicated that the sliding threshold technique (QVT) outperformed k-means clustering (CPS). The k-means segmentation consistently underestimated the area by ~30-40% while the sliding threshold method reduced this to less than 10%. Visual inspection of the segmentations revealed that the sliding threshold technique was better at preserving low velocities leading to a more accurate segmentation. These techniques could further be improved by increasing the input image dimensionality. While doing this would greatly increase the time and memory requirements for k-means clustering, there would be little to no changes for the sliding threshold technique.

Intracranial blood flow is an important hemodynamic parameter in the assessment of many vascular diseases such as Alzheimer's disease, aneurysms, and arteriovenous malformations(129–131). Doppler ultrasound can provide quantitative values but is limited by a small field of view, the cranial bone window, and operator dependence. Radiographic techniques such as computed tomography (CT) and digital subtraction angiography (DSA) provide excellent spatial resolution and qualitative flow information but require the use of radiation exposure and iodinated contrast agents. The application of 4D flow MRI allows for non-invasive quantitative analysis of blood flow while maintaining large volumetric coverage. We investigated the accuracy and internal consistency of blood flow for an in vitro and in vivo model. The QVT-derived flow values from 4D flow MRI showed strong correlation and agreement with ultrasonic flow probe measurements for in vitro studies. In vivo QVT analyses demonstrated that flow

was conserved both along vessel segments and at vessel junctions, signifying good internal consistency of QVT-derived flow measurements. This was performed in both in arterial and venous intracranial vasculature, providing a range of vessel sizes and flow rates for conservation of flow analysis.

A major improvement made in the development of the QVT was the ability to visually assess and interact with 4D flow data. We designed an interactive 3D representation of a vessel angiogram with a superimposed centerline display, color-coded by the user-selected hemodynamic flow parameter of interest. This functionality allows users to easily switch between quantitative hemodynamic parameters of interest and quickly identify locations with potential flow variations. The combination of the angiogram and centerlines in a single display allows users to easily identify vascular regions and ensure accurate centerline generation. Upon the selection of a centerline point of interest, 2D orthogonal cut-planes of the magnitude, complex difference, through-plane velocity, and vessel segmentation mask, along with the flow over the cardiac cycle, are automatically displayed in the QVT control window. These visualizations can be used to ensure that accurate segmentations are performed and may assist in the identification of abnormal flow patterns. For every vascular region of interest analyzed, images of all QVT visualizations (including 3D display, time-averaged 2D cut-plane data, and flow profiles) are automatically captured and stored to allow for easy review of post-processed cases. Additionally, by automatically saving a compressed MATLAB structure file containing only relevant data needed to run the QVT, a user has the capability to seamlessly reload cases within a matter of seconds.

The QVT improved upon a previously presented CPS with technical and graphical developments that led to a significantly faster cranial post-processing tool. By automating post-processing steps, user interaction time is decreased and potential user-dependent errors can be mitigated. The QVT automates all post-processing steps required for cranial 4D flow MRI analysis except for vessel selection. This allowed us to automatically extract, compress, and store qualitative and quantitative hemodynamic information from a network of cranial vessels. By compressing 4D flow data, we have further reduced the memory and storage requirements needed for 4D flow MRI post-processing, allowing QVT to be

completed even on less powerful systems such as laptops which has not been previously possible. The development and implementation of the QVT have made the time required for accurate 4D flow post-processing primarily limited by the number of vessels desired for analysis. We found that with QVT, vessel selection, segmentation and flow assessment, and data saving required approximately 25 seconds to complete. This drastically reduces the amount of time and resources required to post-process a cranial 4D flow MRI, allowing for the possibility of larger studies to be conducted in the future.

5.4.1 Limitations

A major limitation of this study is that the QVT relies on accurate global angiogram generation to automatically place cross-sectional planes. If the V_{ENC} is incorrectly prescribed or vessels of interest include abnormal flow ranges, such as in the presence of stenosis, aneurysms, and arteriovenous malformations, then the global segmentation could miss vessels. Our post-processing includes a 4D phase unwrapping technique(119) to help reduce the errors presented from V_{ENC} underestimation and improve the global angiogram. The addition of dual V_{ENC} 4D flow MRI scans(131) or manually segmented angiograms could also be applied at the cost of longer scan and post-processing times. Another limitation of this study is that ground truth measurements for area and flow could not be concurrently performed in vivo. Due to the fact that multimodality reference standards for vessel area and flow was not feasible in vivo, we performed an in vitro study and utilized internal consistency measurements in vivo to help alleviate this limitation. The QVT was designed specifically for the analysis of cranial 4D flow scans and has yet to be adapted for other regions of the body. This technique could aid in the analysis of abdominal vasculature but would need additional studies to investigate the effects of larger fields of view and motion. Post-processing with the QVT is currently limited to data from our institution's research scan protocol and will need to be updated to accept clinically available 4D flow scans from multiple vendors to allow wide usage. In this case, the maintenance of QVT would require collaborations from multiple institutes and a centralized code repository.

5.5 Conclusion

In conclusion, we have developed and validated a fully-automated QVT that allows for 3D visualization and quantification of cranial blood flow for 4D flow MRI. This technique improved upon an established CPS, further reducing post-processing times through the addition of an interactive 3D GUI, allowing for quick vessel selection and verification of quantitative blood flow parameters. Global and local vascular segmentation was improved through the application of a novel sliding threshold segmentation technique. The completely automated post-processing pipeline reduced the QVT computer memory and storage requirements, allowing cranial 4D flow MRI analysis to be completed with minimal resources and will also increase the repeatability of 4D flow MRI studies by reducing user-dependent errors. The QVT provides a means to investigate the impact of blood flow parameters on neurovascular diseases such as vascular dementia, AVM, and stroke, which may lead to improved treatment and patient outcomes.

Chapter 6: Preoperative 4D Flow Analysis of Renal Cell Carcinoma

6.1 Introduction

6.1.1 Renal Cell Carcinoma

Renal cell carcinoma (RCC) is the most common kidney cancer in adults, accounting for 90-95% of all renal tumors(132,133) and approximately 4.1% of all malignancies. It is the 8th leading cause of death in relation to cancer(134). In the United States, approximately 73,750 new cases and 14,830 deaths occur annually(134) due to RCC, with majority of occurrence in patients aged 50-70 years old(135). With the increase of widespread imaging techniques including ultrasound, MRI, and CT, the detection rate of RCC incidence has increased(136) , allowing for RCC diagnoses at earlier stages and grades. This has led to an increase in 5 year survival rates for patients(137). Considering that RCC treatment has remained relatively unchanged, it is thought that this improvement in survival is directly related to the advancement of diagnostic imaging and earlier radiological diagnosis.

6.1.2 Treatment for RCC

The treatment method for RCC is determined by the likelihood of a cure, which is directly related to the extent of tumor at the time of diagnosis(138). As would be expected, the patient outcomes for early-stage RCC is more favorable than late stage disease. Some of the current treatment options include surgery, active surveillance, thermal ablation, radiation therapy, and immunotherapy, with surgical resection being the only definite curative treatment. Due to this, the mainstay of therapy for RCC treatment is surgery. Radical nephrectomy is the most commonly performed surgical procedure which consists of excision of the entire kidney and additional surrounding tissues (perirenal fat, lymph nodes, adrenal glands, etc.). With the advancement of non-invasive imaging modalities, improved surgical techniques, and better perioperative patient management, nephron sparing surgery (NSS) has become a new alternative for RCC

treatment. An example of NSS (i.e. partial nephrectomy) is presented in Figure 1. Partial nephrectomy can be performed in an imperative or elective manner, such as in the presence of a solitary kidney or a small localized peripheral tumor. Initially, NSS was associated with an excessive morbidity rate, but more recent studies demonstrated long-term functional advantages of preserving unaffected renal parenchyma(139,140). As a more technically challenging operation then a radical nephrectomy, NSS must take into account intrarenal structures such as vasculature and the collecting systems(141,142). This increase in procedural complexity can be mitigated with accurate preoperative imaging provided by ultrasound, CT, and MR imaging techniques.

6.1.3 Imaging for RCC

Preoperative imaging is important for correct staging of RCC and necessary in order to determine a sound surgical approach. For radical nephrectomy, following parameters are paramount: tumor size, venous or lymphatic invasion, and extent of disease, including metastases (Figure 2). With growing interest in NSS and considering its technical difficulty, it is critical to further interrogate the orientation of the kidney for surgical approach, renal arteries and veins as well as arterial supply and location of the tumor with its proximity to the collecting ducts. Contrast-enhanced renal CT is the most commonly used imaging method and is considered the gold standard for RCC imaging(143). It has an excellent specificity and sensitivity allowing it to detect, stage, and guide surgical planning from a single scan(144,145). Although CT has become the preferred method of diagnosis, staging, preoperative planning of RCC, concerns with ionizing radiation and nephrotoxic iodine contrast agents still exist. MRI is primarily used as a problem solver to help characterize indeterminate renal lesions that were previously scanned with ultrasound or CT techniques. The ability of MRI to provide superior soft tissue contrast without the use of ionizing radiation makes it a potential alternative to CT and could instead be used as a primary imaging method for renal tumor evaluation. Previous studies have shown that MRI and CT had comparable rates in the detection of RCCs(146). In addition to providing anatomical details with a variety of different contrast weighting, MRI offers the ability to provide functional information. New techniques utilizing diffusion

tensor imaging(147) and arterial spin labeling(148) have been applied to assess renal perfusion. Angiographic imaging techniques, either with CT or MR, can provide information which may aid in the detection of collateral vessels, minimization of perioperative bleeding, and guidance on the optimal surgical approach. RCCs are known to invade the venous vasculature with extension into the inferior vena cava (IVC) and even up to the right cardiac chambers(149). The level of occlusion in the IVC can have major implication on the surgical planning(150), baseline flow states, and other venous vasculature. MRI has the potential to provide quantitative macroscopic flow values using phase contrast imaging, but has yet to be applied in the context of RCC.

6.1.4 Study Motivation

The development of RCC often involves major changes in the vascular tree, resistance, and circulation patterns. The reaction of the body to adjust to the modified flow resistive network can be complicated to predict. A better characterization of the hemodynamics before a surgical procedure has the potential to improve patient outcome and broaden our understanding of RCC. This research will aid in the development, validation, and visualization of novel non-invasive angiography methods utilizing 4D Flow MRI in the presence of RCC. Specifically we will investigate 4D flow MRI's ability to 1) visualize angiogram generation and collateral localization, 2) quantify the distribution of flow between left and right renal arteries, 3) assess the RCC extension into the IVC, and 4) localize and quantify venous redistribution of flow due to RCC invasion. A thorough literature search did not reveal any relevant 4D flow applications in the context of cancer. This novel 4D Flow application could help to bridge the gap between interventional radiology and imaging while improving our understanding of RCC.

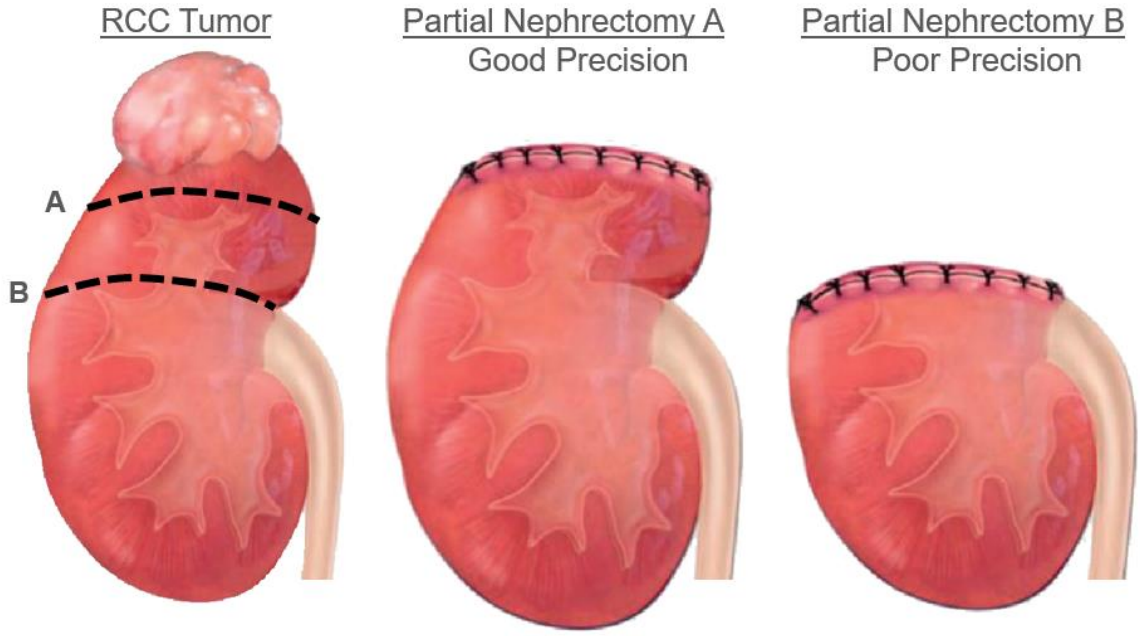

Figure 6-1: Example of a small localized peripheral RCC tumor treated with nephron sparing surgery. The goal of the procedure is to maximize the preservation of renal parenchyma while ensuring the complete removal of the tumorous region. Optimal resections are dependent on the preoperative evaluation of the medical imaging techniques. Region A shows a precise resection while region B includes more non tumors regions but ensures complete tumor removal. This figure was adapted from (151).

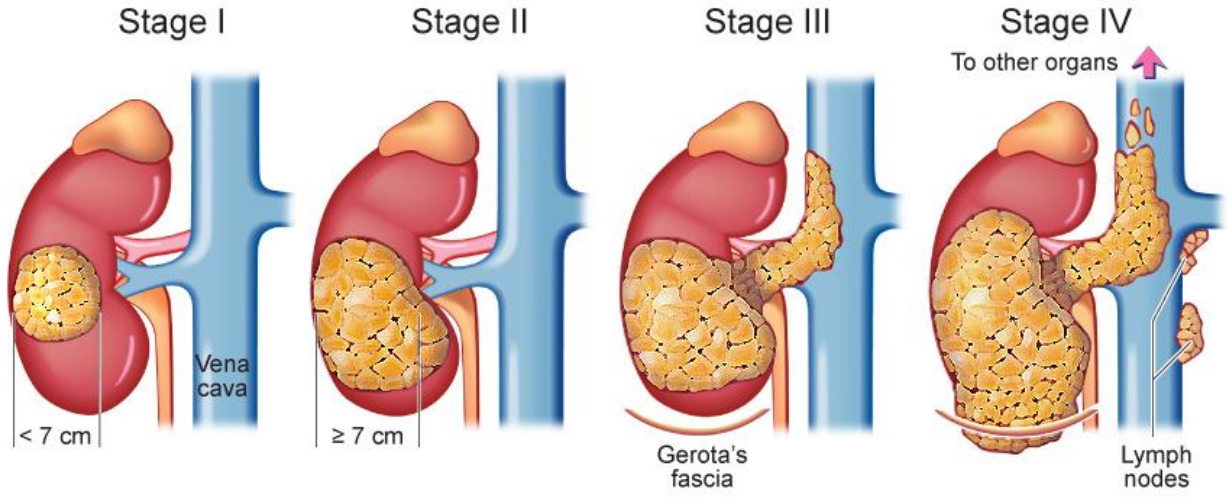

Figure 6-2: Shows the staging levels for renal cell carcinoma (RCC). RCC classification primarily relies on the tumor size (+/- 7 cm), level of invasion into venous vasculature (inferior vena cava), invasion into lymph nodes, and distant metastasis. Stage 1 and stage 2 are confined to the kidney and are based on a size that is greater or less than 7 cm. The Stage 3 RCC has invaded the venous vasculature and started to involve the renal vein or inferior vena cava. Stage 4 has spread to local or distant organs as well as invade the lymph nodes. Diagram cited from (152).

6.2 Methods

Eleven RCC patients (males: 9, mean age: 62.4 years, age range: 47-84 years) participated in the study after informed patient consent and Institutional Review Board (IRB) approval. 4D flow MRI was performed using a 3D radially-undersampled sequence (PC-VIPR (GU, Johnson)). Volumetric coverage of the abdomen, centered on the kidneys, was acquired with the following imaging parameters: reconstruction matrix= 256x256x256; acquired isotropic resolution = 1.25 mm^3; imaging volume = 32x32x32 cm^3; scan time = ~10 min; encoding scheme = 4-point referenced. Velocity encoding sensitivity (V_{ENC}) ranged from 60-120 cm/s. Additional scan information on repetition time, echo time, tip angle, and receiver coils are given in Table 6-1. Cardiac gating was recorded using the MRIs pulse oximeter. Fourteen cardiac time frames were binned retrospectively using our custom reconstruction pipeline based on the ECG signal. Respiratory gating was acquired during all scans and binned retrospectively using our custom reconstruction pipeline based on the acquired bellows respiratory waveforms. All MR scans were acquired on a clinical 1.5T or 3.0T scanner (GE Healthcare, Waukesha, WI, USA).

4D Flow Scan Parameters

TR	TE	Field Strength	Tip Angle	Coil (channels)
6.23	2.08	1.5	12	Body (24)
5.57	2.01	3	8	Body (24)
6.04	2.39	1.5	15	Cardiac (8)
6.08	2.33	1.5	8	Cardiac (8)
6.06	2.36	3	15	Body (24)
6.14	2.63	1.5	8	Body (24)
6.32	2.68	1.5	10	Cardiac (8)
6.51	2.38	3	12	Body (24)
6.01	2.12	3	15	Body (24)
6.14	2.63	1.5	8	Body (48)
6.30	2.15	1.5	8	Body (24)

Table 6-1: This table gives the scan parameters and coil information used for all the scans. The level of variabilty in parameters spurs from all cases coming from clinical referal and a variability of scanners and personel avialable to complete 4D flow scans. TR – repetition time, TE – echo time.

6.2.1 Qualitative Analysis

The initial post processing included a semi-automatic segmentation of the arterial and venous vasculatures. Complex difference images were generated from the acquired 4D Flow MRI and saved as a DICOM format. The DICOMs were loaded into a commercial segmentation software (Mimics 17.0 Materialize, Leuven, Belgium) where a three-step segmentation process was completed. First a global threshold is applied to segment majority of the vasculature from the background tissue. Next an adaptive region growing technique was applied throughout the vasculature to further remove any background tissues and help reduce noise affects. Lastly a manual 3D segmentation was completed to separate the venous and arterial vasculature while removing any additional noise. The arterial and venous segmentations were exported as text files containing the spatial and intensity information of the masks. Following the segmentation, time-resolved reconstructions were loaded into a custom-built MATLAB tool where 3rd order polynomial background phase correction was completed. The tool then generated Ensight (Ensight 10.0.3 CEI, Apex, NC) files for visualization and cross-sectional plane placement using the segmentation text files and background phase corrected 4D flow data. Visual assessment of arterial and venous angiograms was completed for collateral vessel development. Streamline generations were used to localize irregular flow and visual flow throughout the abdominal vasculature Figure 6-3. The level of IVC invasion and occlusion was visually determined from the semi automatically segmented venous angiograms. The level of IVC invasion was ranked as follows (-) no to minimal tumor occlusion in the IVC, (+) tumor is partially occluding the IVC with patent Infra IVC, (++) tumor invasion in the IVC with completely occluded Infra IVC.

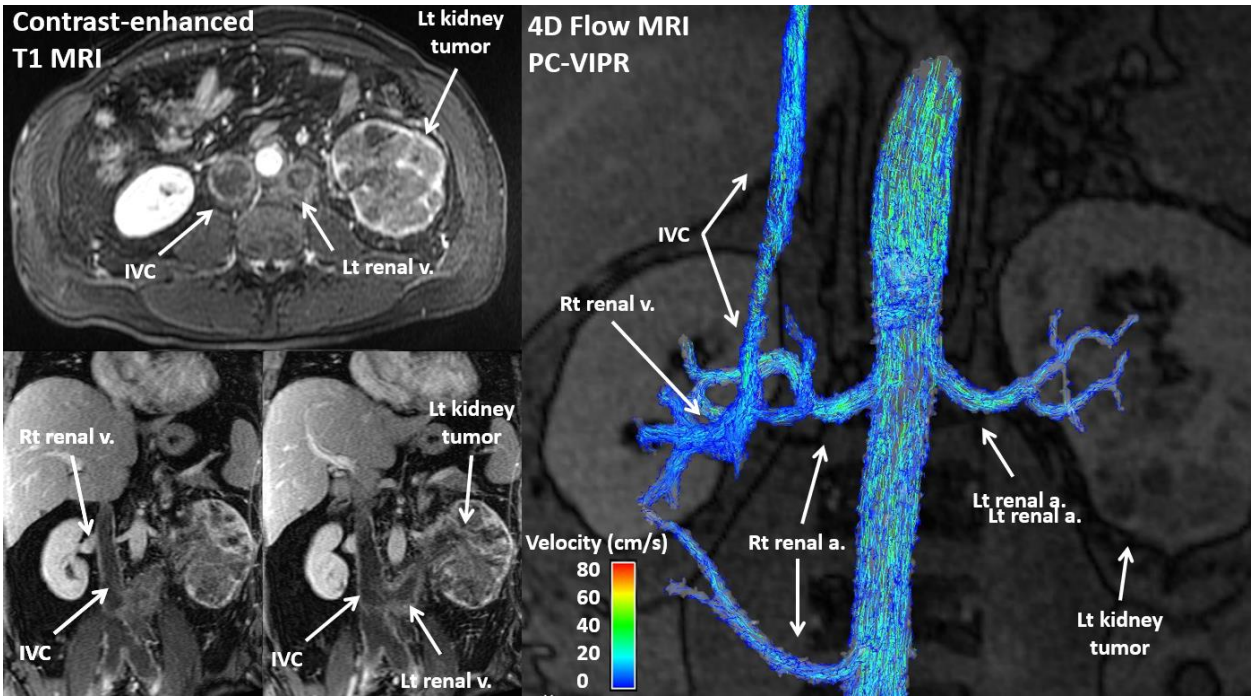

Figure 6-3: The contrast-enhanced T1 MRI clearly shows the renal cell carcinoma invasion in the kidney and venous vasculature. The RCC has extended into the inferior vena cava (IVC) but, from the T1 MRI alone, it is difficult to determine if the IVC has become fully occluded. 4D Flow MRI provides the ability to visualize the abdominal vasculature and provide quantitative velocity streamlines. With the addition of the 4D Flow imaging it can be concluded that the IVC has a small patent section for venous return, which is crucial information for treatment planning.

6.2.2 Quantitative Analysis

The arterial flow distribution between the left and right kidneys was compared between a group of seven healthy controls from a meal challenge (1) and nine RCC patient in this study. Flow analysis was completed by manually placing cross-sectional planes with Ensight (Ensight 10.0.3 CEI, Apex, NC) at the right and left renal arteries. Additional analysis planes were used to capture any collateral flow to either kidney and the additional flow was added to the kidney's total blood flow. To assess the flow distribution between two kidneys a percent flow distribution value was calculated as the absolute difference of flow between kidneys divided by the sum of flow from both kidneys (i.e. |Left renal flow – Right renal Flow|/(Left renal flow + Right renal Flow) *100). The asymmetry of renal flow in RCC patients was further assessed by comparing the percent flow distributions for cases that had majority of renal flow directed toward and away from the RCC kidney. The redistribution of venous flow was investigated by

quantifying flow from planes placed at the suprarenal aorta (ASR), suprarenal IVC (ISR), and lumbar veins (LV). An example of plane placement location can be viewed in Figure 6-4. Additional analysis planes were used in the presence either collateral arteries or veins and the additional flow was added to the vessels total flow. Venous to arterial flow ratios were computed with and without the inclusion of lumbar venous return as a measure of collateral flow. All the arterial and venous flow measurements were completed using exported Ensight planes to a customized software package that allowed for time resolved manual vessel cross-section segmentation.

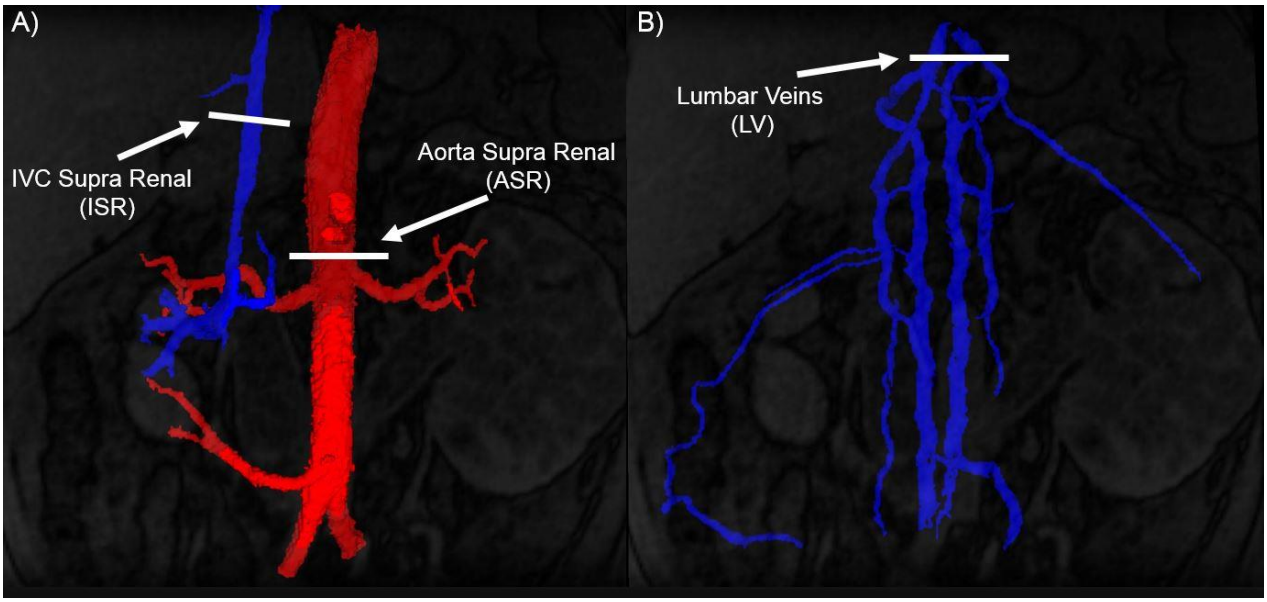

Figure 6-4: Approximate plane placement for flow quantification used in the venous flow redistribution study are shown by the white lines. A) Includes two planes measuring the arterial and venous blood supply from the aorta and inferior vena cava respectively. B) Shows an example plane for flow quantification in the lumbar veins when visible. In the presence of collateral vasculature additional planes were placed and the quantified values were added to the main arterial or venous return.

6.2.3 Statistical Analysis

To assess the percent flow distribution between kidneys in healthy controls and RCC patients a modified student's t-test known as the Welch's t-test(153) was used. In this case the variances are assumed to be unknown and unequal and the degree of freedom is given by the Satterthwaite's(154) approximation. To test the difference in degree of flow asymmetry when the majority of flow is director toward the RCC

kidney or toward the healthy kidney a student's t-test was applied. To assess the redistribution of venous flow, the average ASR to ISR ratios were reported for the three levels of IVC cancer invasion. An identical process was completed with the addition of LV flow. The range for each arterial to venous ratio was reported to show the variation within each cancer invasion grouping. All confidence intervals used in this study were calculated as a 95% confidence interval. For this study, a p-value < 0.05 was considered statistically significant. All statistical analyses were done using MATLAB 2018b (MathWorks, Natick, MA, USA).

6.3 Results

From the eleven RCC patients that participated in this study, two had a solitary kidney and were excluded from the renal flow asymmetry analysis. The variation in scan parameters, magnet field strength, and coils across patients was the result of all imaging request coming from clinical referrals. Due to this our imaging protocols needed to be completed in a timely manner and to meet our clinical needs that required us to utilize different scanners, technicians, receiver coils and protocols for 4D Flow imaging. 4D flow reconstructions, including the respiratory and cardiac gating, were completed automatically in approximately 1.5 hours. Inspection of the ECG gating files showed minimal variations in heart rates. Visual analysis of the cross-sectional planes used for flow quantification showed no visible aliasing or motion artifacts for vessels of interest.

6.3.1 Qualitative Analysis

Semi-automatic angiogram segmentation of the venous and arterial vasculature was completed successfully. Arterial collateral vessel development was highly variable between all patients. The arterial collaterals were not always directed toward the RCC kidney. Angiograms for cases with high and little to no arterial collateral development are presented in Figure 6-5. The lumbar veins were detectable and

large enough for flow analysis in 8 out of the eleven cases. Seven out of the eight lumbar vein enhanced cases had a partial to fully occluded IVC. Examples showing the level of RCC invasion into the IVC and the associated lumbar vein enhancement can be view in Figure 6-6. Discussion

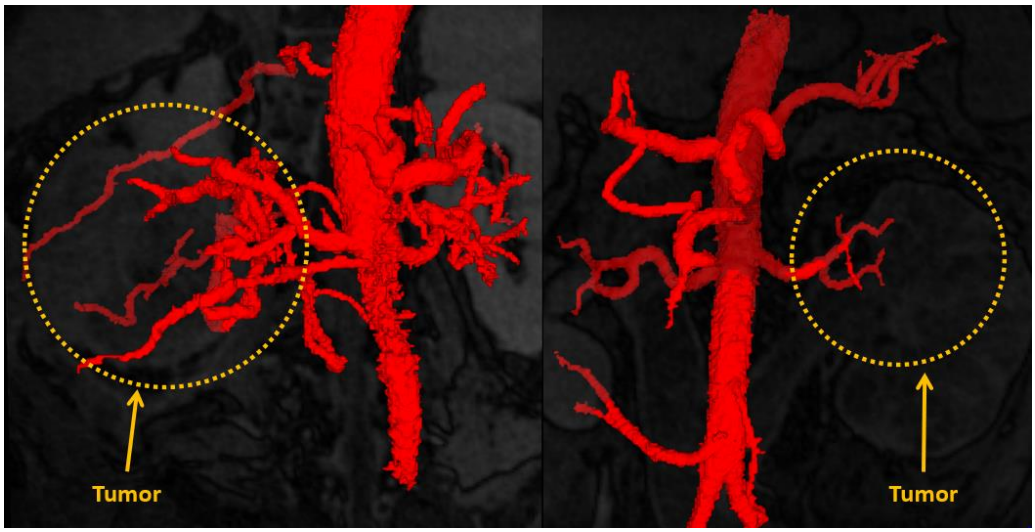

Figure 6-5: The level of collateral development was highly variable between patients. A) A large number of arterial collaterals have formed and are leading toward the tumorous kidney. B) The vasculature between the left and right kidney has little to know visible difference and no collaterals were detected. The variations in collateral develop adds an additional level of complexity when quantifying flow distributions between kidneys.

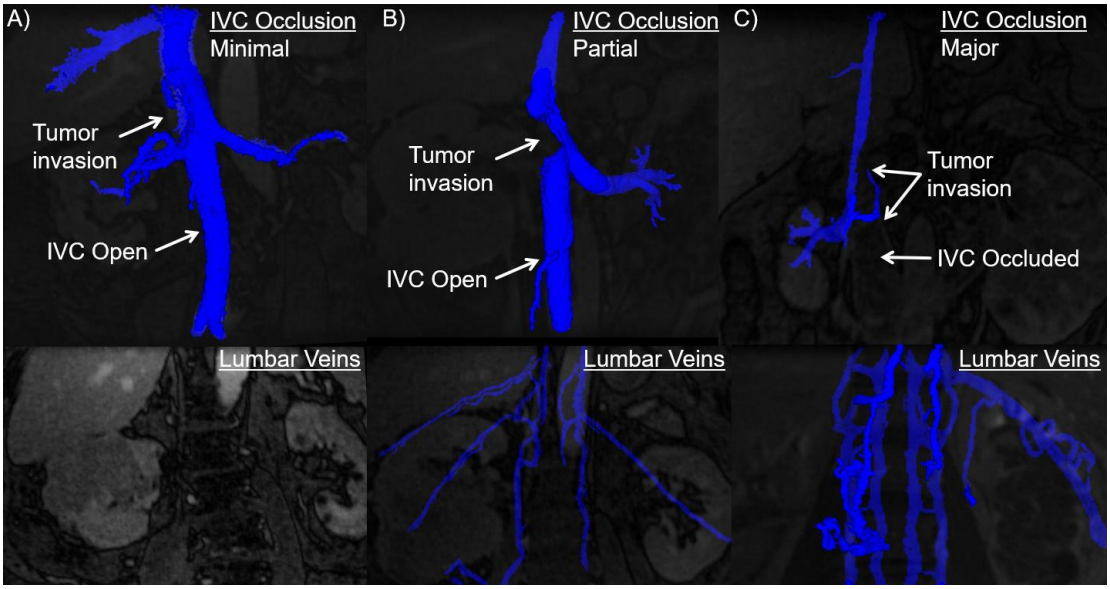

Figure 6-6: Different levels of renal cell carcinoma invasion into the inferior vena cava (IVC) can be viewed in A) Minimal to no cancer invasion '-', B) Partial cancer invasion with lower IVC patent '+', and C) Major cancer invasion with occluded lower IVC: '++'. These different levels of invasion were used to group patients for the venous return analysis. The lumbar enhancement associated with the increase in IVC occlusion is shown in the second row of images.

6.3.2 Quantitative Analysis

The arterial renal flow calculations and absolute percent flow distribution between kidneys are presented in Table 6-2. The renal flows for the healthy and RCC kidneys were plotted and grouped by IVC invasion as seen in Figure 6-7. The arterial flow plot did not show a clearly discernible trend based on renal flow or preferential flow direction for all cases or IVC groupings. The average absolute percent flow distribution between kidneys was higher in the RCC cohort (36.18 +/- 11.65 %) than the healthy control group (6.65 +/- 8.44 %) with an average increase in percent flow asymmetry of 29.53% (95% CI = [18.75, 40.31]). The increase in percent flow variation for RCC patients was found to be statistically significant ($p = 1.51e-4$). The magnitude of percent flow variation as a function of preferential flow direction toward the healthy or RCC kidney was tested. The average percent flow variation was larger when the flow was directed toward the RCC kidney (42.20 +/- 9.06) than compared to a flow directed toward the healthy kidney (28.66+/-10.81%) by 13.54% (95% CI = [-2.08,29.16]). This difference was not found to be statistically significant at the level of $p<0.05$. A summary of the asymmetry percentages can be found in Table 6-3. The average lumbar flow showed an increase with the level of IVC invasion category from (-) 0.958 ml/sec, (+) 8.44 ml/sec (++) 14.16 ml/sec. Three of the four pre-treatment (-) cases had an ISR/ASR value greater than 1 ranging from 1.28-1.34. Seven of the eight cases with detectible lumbar veins had an ISR/ASR ratio below 1 ranging from 0.34 – 0.85. The addition of LV to the ISR/ASR ratio resulted in average values closer to 1 for the partially occluded (+) 0.98 and majorly occluded (++) 0.85 IVC cases. Quantitative flow and venous to arterial blood flow ratios, with and without lumbar, are presented for all eleven cases in Table 6-4.

Renal Flow Distribution

Age (yrs.)	Sex	Tumor Side	Tumor IVC	Left Renal Flow (ml/s)	Right Renal Flow (ml/s)	% Flow Variation
70	M	L	-	12.02	5.87	34.38
58	M	L	-	3.13	4.88	21.84
84	M	R	-	2.82	7.45	45.08
58	M	L	-	17.48	N/A	N/A
47	F	L	+	8.83	4.1	36.58
63	M	R	+	8.38	18.75	38.22
50	M	R	+	N/A	6.01	N/A
73	F	R	+	3.63	2.56	17.28
63	M	L	++	1.25	2.63	39.93
52	M	L	++	4.4	10.25	56.73
68	M	R	++	2.12	7.68	35.67
Control*	N/A	N/A	N/A	6.44	6.11	6.65

Table 6-2: This table gives the measurements for flow distiribution between the left and right kidneys. The presented flow is the summation of the main arterial renal and visible collaterals. In 2 cases patients only had a solidary kidney and the missing kidney value is filled with a N/A. The percent flow varaiation is calculated as the absolute value of flow diference between kidneys divide by the sum of flow to both kidneys. Tumor invasion to the venous vasculature was catergorized by the following symbols: - No to minimal tumor in the IVC, + Tumor in the IVC with open infrarenal IVC, ++ Tumor in the IVC with occluded infrarenal IVC. * Average healthy control data was used from a 4D flow meal challenge and is comprised of the average of 7 patients (1).

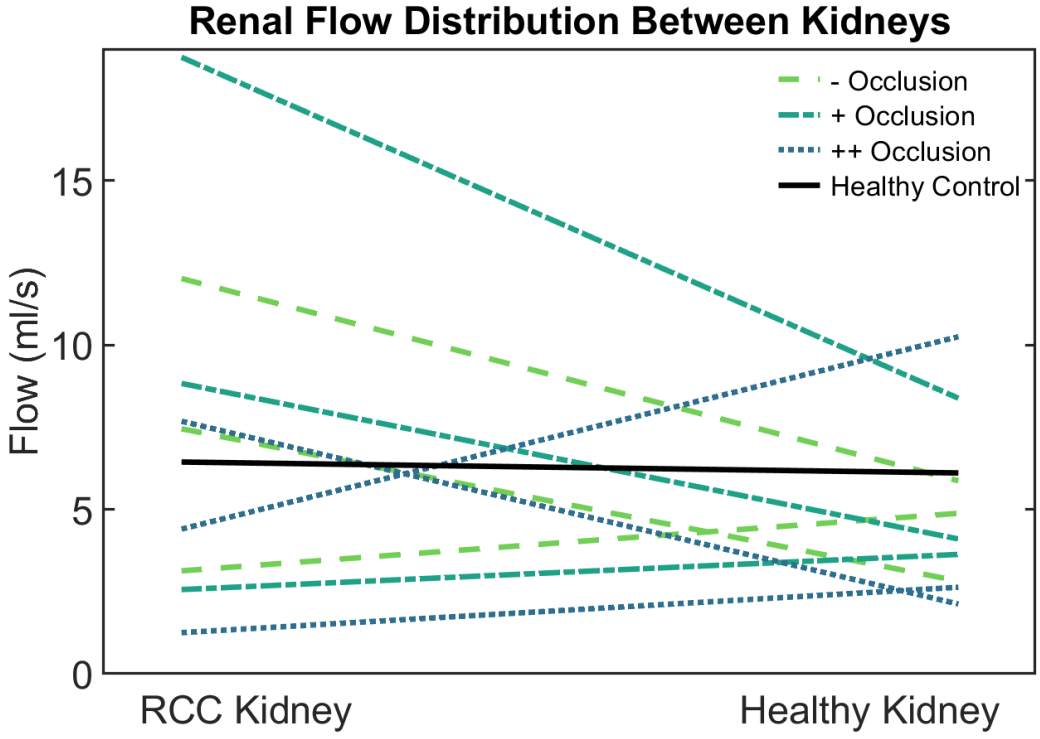

Figure 6-7: An asymmetry in renal flow distribution is present in all RCC cases analyzed. There does not seem to be a preferential direction of flow toward or away from the cancerous kidney. The level of cancer invasion into the IVC did not seem to impact the preferential direction of flow seen between kidneys.

Renal Flow Asymmetry: Healthy vs RCC		Asymmetry Directionality: Healthy vs RCC	
	% Flow Variation		% Flow Variation
Healthy Control*	6.65 ± 8.44	Toward Healthy Kidney	28.66 ± 10.81
RCC	36.18 ± 11.65	Toward RCC Kidney	42.20 ± 9.06
Mean Difference	29.53 CI:[18.75,40.31]	Mean Difference	13.54 CI:[-2.08,29.16]
p-value	1.51e-4	p-value	0.0795

Table 6-3: The asymmetry between renal artieres was investigated for a group of healthy controls and RCC patients. There was a statistically significant increase in asymetery of flow between kidney in the presence of RCC. The statistical test assumed unequal and unknown variances. The directionality of the flow was test for toward the healthy kideny and toward the cancerous kidney. When flow was directed toward the RCC kidney a higher degree of symetry was found but was limited by the small sample size.

Venous Flow Redistribution

ASR (ml/s)	ISR (ml/s)	LV (ml/s)	ISR/ASR	(ISR+LV)/ASR	Tumor IVC
39.52	50.66	4.79	1.28	1.40	-
28.70	36.60	ND	1.28	1.28	-
38.36	38.16	ND	0.99	0.99	-
45.22	60.75	ND	1.34	1.34	-
30.34	20.20	12.05	0.62	0.99	+
30.80	14.66	12.90	0.47	0.89	+
43.70	37.30	6.61	0.85	1.00	+
34.82	26.48	6.67	0.76	0.95	+
33.73	11.40	17.51	0.34	0.86	++
31.70	10.64	15.95	0.34	0.84	++
48.99	32.06	9.03	0.65	0.84	++

Table 6-4: This table gives the measurements for flow leaving and returning to the heart at cross-sectional planes placed directly above the arterial and venous renal branches. Redistributed flow to the lumbar veins was measured in cases of lumbar enhancement due to RCC extension into the inferior cava. The ratio of arterial flow in the aorta and venous flow in the inferior vena cava were computed. A second ratio was computed with the additon of lumbar venous flow to correct for missing collateral venous flow. ASR - Aorta Suprarenal ,ISR - Inferior Vena Cava Suprarenal, LV - Lumbar Vein Total, ND - Not Detectable Symbols: -- No to minimal tumor in the IVC, + Tumor in the IVC with open Infrarenal IVC, ++ Tumor in the IVC with Occluded Infrarenal IVC

6.4 Discussion

This work presents the application of 4D flow MRI in the presence of renal cell carcinoma, as an imaging technique that can provide both structural and functional preoperative information related to the kidneys. We investigated the ability to generate arterial and venous angiograms from a single 4D flow scan (PCVIPR(50,51)) in a cohort of patients with varying levels of RCC invasion. This technique allowed us to quantify blood flow from the arterial and venous vascular systems while clearly displaying cancer extension into the inferior vena cava. The flow distribution between the kidneys was assessed as a metric to distinguish RCC patients from healthy individuals and in all cases a clear asymmetry was found to develop in the RCC cohort. The large field of view provided by 4D flow MRI allowed for an investigation of venous redistribution as a function of RCC extension into the IVC to be completed. The redistribution of flow led to detectible lumbar vein enhancements as well as the visualization of both arterial and venous collateral vessels. We believe that the addition of both quantitative and qualitative information provided by this technique will lead to better informed treatment decisions and in turn result in positive patient outcomes.

Medical imaging techniques, primarily ultrasound, CT, and MRI, have become the mainstay of methods to provide preoperative information on RCC. Preoperative imaging typically focuses on providing structural information pertaining to the cancer location, size of the tumor, extent, and critical surrounding tissues. As surgical resection, radical or partial nephrectomy, is currently the only curative treatment for RCC(155), having a detailed vascular roadmap prior to surgery can be critical in reducing surgical times and patient bleeding. With the growing support of nephron sparing surgeries(156), which are more technically challenging than a radical nephrectomy, it is critical to not only provide a detailed angiogram of the kidney vasculature but additionally locate any collateral vessel development. We found 4D flow MRI could provide detailed angiograms of the arterial and venous renal vasculature from a single 10 min scan. These angiograms allowed for the localization of main feeding arteries to both kidneys, vascular detail of second order branches, arterial of venous collaterals, and RCC extension into the IVC.

The vascular information provided by 4D flow MRI would be similar to contrast enhanced CT angiograms but could be acquired without any additional ionizing radiation.

The surgical treatment decision for RCC cases depend upon the stage of the tumor as well as what is seen in preoperative imaging(157). The most common treatment method is a radical nephrectomy, but even these procedures can become more complex with extension of tumor thrombus into the IVC, which occurs in approximately 10% of cases(158). CT is typically the method of choice for preoperative imaging but in the presence of IVC invasion contrast enhanced MRI has become a recommended method to further investigate IVC occlusion(159). The invasion of RCC into the IVC wall causes an increase in surgical complexity, due to the possibility of segmental resection or prosthetic replacement(160), and reduction in patient 5-year survival outcomes(161). Typically wall invasion and treatments are determined intraoperatively with MRI providing potential options for preoperative wall invasion assessment techniques(162). In cases where tradition contrast enhanced MRI still have a level of ambiguity in the assessment of IVC occlusion or wall invasion, 4D flow MRI could help mitigate the uncertainty. A few cases presented in this study clearly showed a patent section of the IVC, while it was non diagnosable from the CE MRI alone. This minimal flow through the IVC, even in cases of extreme IVC thrombus, may be a predictor of IVC wall invasion and help inform surgeons of successful treatment options prior to intervention.

The clinical assessment of kidney function is commonly completed thought the use of glomerular filtration rate (GFR). In practice GFR cannot be directly measured easily, thus GFR estimations are made using a variety patient specific information such as sex, race, age, body size, and creatinine(163). GFR estimations remain as a relatively imprecise metric for kidney function(164) thus alternative approaches using PET(165) and MR perfusion techniques(166) are being investigated. 4D flow MRI could provide additional information related for kidney function by quantifying the distribution of flow between the kidneys. We did not see a preference in flow directionality in relation to the RCC kidney or healthy kidney but an asymmetry between the kidneys was consistently present. A potential reason for variation

in dominant flow could be due to the cancerous kidney's recruitment of collateral vessels and the healthy kidney's increase demand for blood filtration. The ability to assess kidney function individually, which GFR does not do, could allow for better informed treatment decision. For example, if 4D flow MRI showed a large asymmetry of flow between the kidneys the direction of flow could inform which surgical procedure may reduce patient risk while minimizing surgical complexity. In addition to this 4D flow may provide a simple metric to inform the surgeon of venous redistribution by computing venous to arterial ratios of major abdominal vessels.

We showed that 4D flow MRI could be used as a preoperative imaging tool in the assessment of structural and functional hemodynamic changes occurring due to the presence of RCC. Once the radical of partial nephrectomy is completed it is crucial to monitor the patient for recurrence and additional complications. Medical imaging has become important for patient monitoring with a wide variety of guidelines and strategies(167–169). Abdominal MRI, with or without contrast, is considered an adequate method for surveillance from all major guidelines(167–169) as it does not require ionizing radiation. Primarily structural MRI imaging, (T1, T2,PDW) is used for patient monitoring post RCC treatment. 4D flow MRI has the potential to provide functional information alongside the current monitoring standards. The two parameters assessed in this work, arterial flow asymmetry and venous to arterial ratio, could be utilized in the post treatment monitoring of a patient. In cases where partial nephrectomies are completed a decrease in flow asymmetry between kidneys could indicated the patient's level of recovery. The venous to arterial ratio could help aid in the monitoring of surgeries that required IVC resection or replacement.

6.4.1 Limitations

A limitation of this study was the variability of scan parameters and coils used to complete all the RCC 4D flow scans. For future scans, especially if patient follow-up or monitoring will be completed, we can develop a more standardized protocol for the renal 4D flow scans and try to minimize the variations in coil and scanner strength. An important parameter to accurately select for 4D flow examinations is the

Venc. Inaccurate selection of this variable can lead to phase wrapping if set too low or lead to a decrease in signal to noise if set too high. Dual Venc scans could be used to avoid this problem at the cost of an increase in scan time. For MRI body imaging, motion can be a big problem that degrades the image quality. Respiratory gating techniques, which we acquire with bellows, can be applied in order to help deal with motion artifacts. In addition to respiratory gating, the cross-sectional vessel planes were selected close to the aorta which saw less motion than distal renal arteries. The isotropic spatial resolution (1.25mm) of our current scans can detect a majority of the greater abdominal vessel. It is possible for smaller collaterals to be missed with the current scan parameters. We could try to increase the spatial resolution further, but to avoid the SNR drop we would need to increase the scan time. As this study was mainly focused on vessel sizes greater than 5mm we felt we were still able to capture majority of the import vascular territories. The sample size for flow distribution directionality analysis was based on groups of 5 and 4 patients. We are possibly seeing a trend related to flow direction develop but to improve the statistical power we would need to recruit more patients.

6.5 Conclusion

In conclusion, we investigated the application of 4D flow MRI as a feasible imaging technique that may allow for both the structural and functional preoperative analysis of RCC patients. This technique allowed for a single scan to be completed in approximately 10 minutes that could provide detailed arterial and venous angiograms. Visualizations of the angiograms could help in the surgical planning of RCC treatments by providing locations of collateral vessels, the main feeding arteries, and a clear visualization of IVC invasion, all of which are critical to surgical planning. 4D flow additionally provided a way to quantify arterial and venous blood flows over a large volume. The distribution of flow between renal arteries and the venous to arterial suprarenal ratios were both measured as ways to provide insight into kidney function and collateral venous flow redistribution as a function of IVC invasion, respectively. This work is the first step to provide information on macroscopic flow in relation to RCC. We believe that 4D flow MRI has the potential to become an invaluable tool for preoperative decision making of RCC cases.

Chapter 7: Summary and Recommendations

7.1 Summary of Research

Angiographic imaging techniques are routinely used to provide detailed vascular maps with x-ray, magnetic resonance, and ultrasound imaging modalities. 3D acquisitions, typically acquired with MRA or CTA methods, have become widely used as they can provide alternative visualizations, volumetric representation, and efficient interpretation (170). The majority of the angiographic imaging techniques provide structural vascular information, but lack in the ability to provide quantitative hemodynamic parameters. The techniques that can provide both quantitative and qualitative vascular information, typically require complex post-processing. This can lead to lengthy post-processing times, added costs, and variations across users and, hence, difficulty for clinical adaptation. This work focused on the development of automated and efficient post-processing tools, to allow for a streamlined and reproducible analysis of quantitative angiography data. A summary of the specific contributions of this work include:

- The results of a phantom and in vivo porcine study, demonstrating that arterial blood velocity can be quantified using a quantitative 2D-DSA (qDSA) technique. We investigated the effects of various imaging and injection parameters on velocity calculations utilizing qDSA. The proposed qDSA method allowed for accurate and precise calculation of blood velocities, in near real-time, from time resolved 2D DSAs.

- Functional hemodynamic changes occurring pre-, post-, and during treatment, were investigated as a means to improve the repeatability and effectiveness of transarterial embolization (TAE). Radiographic imaging (2D DSA) and 4D Flow MRI (PC VIPR) were applied and compared to alternative quantitative techniques, ultrasound doppler wire and color-coded DSA. qDSA was able to characterize intra-procedural changes in hepatic arterial blood velocity in response to TAE, while 4D flow MRI was able to capture blood velocity changes pre- and post- TAE treatment.

- The application of an in vitro and in vivo study demonstrating the validation of an automated post-processing tool for cranial 4D flow MRI was completed. We investigated the capabilities of a newly

developed quantitative velocity tool (QVT) to accurately segment and quantify flow in the carinal vasculature. The development of this cranial 4D flow MRI post processing tool makes blood velocity calculations feasible and more readily translatable to clinical workflow.

- The use of 4D flow MRI as a quantitative tool to add presurgical information to renal cell carcinoma cases. This technique was able to provide large abdominal anatomical coverage with qualitative and quantitative flow information. The distribution of flow between kidneys, arterial to venous flow ratios, collateral vessel development, and inferior vena cava cancer invasion were assessed. 4D flow MRI was able to provide additional preoperative information that could influence surgical decision making and improve patient outcomes.

7.2 Innovations

In the completion of this dissertation, many advances were made that built upon the foundations of angiographic imaging techniques. Some notable contributions include:

- The development and application of a quantitative DSA post-processing tool for abdominal 2D DSAs. A major advantage this tool offers is near real-time calculations for intraprocedural blood velocity calculations. This is the first post processing tool created for use in body interventions and makes quantitative DSA more readily translatable to the clinical(17,19).

- Application of quantitative techniques to assess the efficacy of transarterial liver embolization (TAE). The quantitative DSA tool allowed for objective metrics, related to blood velocity, to be acquired intro-procedurally. This is the first time the relationship between blood velocity reductions and degree of embolization have been captured during a TAE procedure. This work may be critical for determining optimal treatment endpoints and improving the standardization of TAE(20,22).

- A fully automated 4D flow cranial post processing tool that provides 3D visualization and quantification of cranial vasculature. The time required for post-processing a cranial case was reduced to approximately 30 seconds per vessel, allowing for large clinical studies to be completed. 3D visualizations, provided in this tool, allows for a color-coded vascular network to be utilized for the

detection of vascular anomalies, further increasing its potential benefits for cranial 4D flow post processing(24).

- The application of 4D flow MRI for preoperative geometric and hemodynamic vascular analysis of renal cell carcinoma. This is one of the first piece of work that utilizes 4D flow MRI in the realm of cancer. The additional information provided by 4D flow MRI, may enable improved treatment approaches and patient outcomes(26,28).

7.3 Future Recommendations

7.3.1 Quantitative Fluoroscopy

In its current form, qDSA can provide quantitative blood velocities, in near real time, from 2D DSA imaging sequences. A high frame rate in combination with DSA sequences, would cause an increase in radiation dose delivered to a patient. Our study focused on proving the feasibility of a technique and the next step would be to adapt the technique for clinical practice. Two areas that would need investigation include minimal frame rates and dose requirements that will maintain the tool's quantitative blood velocity capabilities. We have completed preliminary studies in phantoms that indicate qDSA may also be viable with non-subtracted fluoroscopic imaging techniques, which would significantly decrease the radiation exposure while keeping high frame rates. Alternatively, clinically available imaging modes used for device placement that provide high frame rates at doses in between fluoroscopy and DSA, could be utilized.

7.3.2 Contrast Distribution Maps

The quantitative 2D DSA techniques presented in this work have focused on the quantification of velocities in macroscopic vessel. The completion of a transarterial embolization (TAE) does cause changes in the macroscopic vasculature but the true target is at the tissue level. The 2D DSA acquisitions for this study did show visible changes at the tissue level. The tissue changes are currently used subjectively in the determination of embolization endpoints. There are a few tools that allow for the local

investigation of perfusion changes but are not widely used clinically. Extending the qDSA tool to quantify contrast changes globally on the tissue level, would further the accurate determination and localization of areas that were affected by TAE. We have completed some preliminary research in characterizing embolization related changes at the tissue level in the liver (171,172). The localization and quantitative parameters provided by the analysis of contrast tissue changes seem to be a promising addition to the qDSA technique. An example contrast map pre- and post- embolization can be view in Figure 7-1.

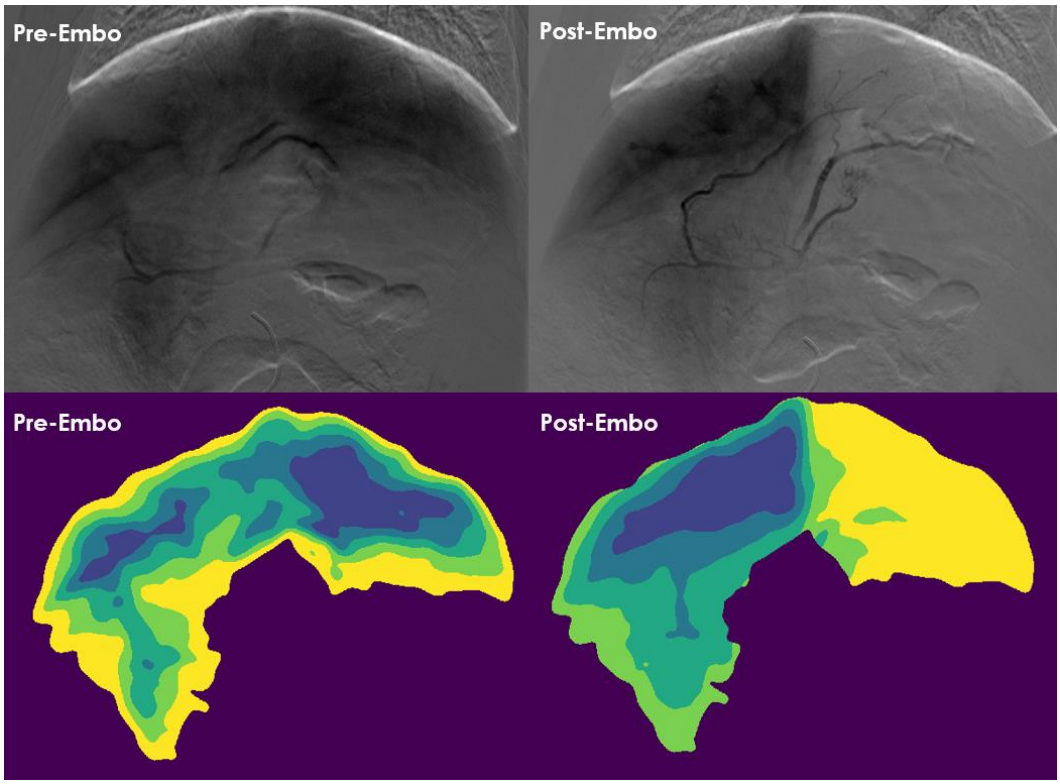

Figure 7-1: Regional hepatic contrast distribution maps that depict embolization related changes in perfusion pre- and post- transarterial embolization. The color encoded images are grouped into 5 different regions, with yellow being the lowest contrast and dark blue being the highest contrast.

7.3.3 Abdominal Quantitative Velocity Tool

The quantitative velocity tool (QVT) was designed and validated specifically for cranial analysis of 4D flow MRI datasets. It currently is optimized for the analysis of the 4D flow MRI PC-VIPR sequence acquisition, which is not clinically available. Adaptation of this tool to provide analysis for a variety of

clinically available 4d flow sequences would broaden the use of QVT. Additionally, QVT could be adapted for applications outside of the brain. The ability of 4D flow to capture large imaging volumes makes the potential abdominal applications a desirable next step. The abdominal vasculature in humans is highly diverse and can provide complex vascular networks that are difficult to analyze quantitatively. QVT may be able to provide a solution to the lengthy post-processing times required for quantitative abdominal 4D flow analysis. Limitations of the current tool that would need to be addressed for abdominal use include time-resolved cross-sectional segmentations, effects of motion, and global angiogram generation. Adapting the current version to accept manually segmented angiograms may be a quick alternative approach for initial abdominal investigations. The experimental procedures used to validate QVT in the brain could be replicated in the body to ensure consistent and accurate quantitative hemodynamic parameters.

7.3.4 Renal Cell Carcinoma Post-Operative

The macroscopic vascular changes due to the presence of renal cell carcinoma (RCC) were investigated pre-operatively with 4D flow MRI. The logical extension of this work would be to acquire post-operative 4D flow images for this cohort of patients. The quantitative variables used for analysis in this work, renal flow asymmetry and venous to arterial blood flow ratios, could be quantified over multiple time points following treatment. The changes in the quantitative values could then be compared to patient outcomes which would give insight into the ability of 4D flow MRI to predict patient outcomes. To extend the pre-operative analysis, additional patients could be added to the cohort to increase the statistical power of the findings. As there is a high variability between patients, this could necessitate a large-scale study. Lastly, the current pre-operative flow analysis procedures could be paired with functional kidney tests, such as glomerular filtration rate or PET, to analyze if kidney blood flow is a measure of kidney function.

References:

1. Sylvana García-Rodríguez Diurnal Variation of Renal Blood Flow using 4D flow MRI. In Proceedings of the 24th Annual Meeting of ISMRM, Singapore, 2016. 0709.

2. Abrams HL. Abram's Angiography. Boston: Little Brown , and Co.; 1996.

3. RONTGEN, W. C. ON A NEW KIND OF RAYS. *Science* **3,** 227–231 (1896).

4. Haschek E, Lindenthal O. Ein Beitrage zur praktischen Verwertung der Photographie nach Röntgen. Wiener Klin Wschr. 1896;9:63–64.

5. Sicard J, Forestier J. CR Soc Biol. Vol. 88. Paris: 1923. Injections intravasculaires d'huile iodée sous contrôle radiologique; pp. 1200–1202.

6. Kelcz, F., and C. A. Mistretta. 'Absorption-edge fluoroscopy using a three-spectrum technique.' Medical physics 3.3 (1976): 159-168.

7. Kruger, R. A. *et al.* A Digital Video Image Processor for Real-Time X-Ray Subtraction Imaging. *Opt Eng* **17,** 176652-176652- (1978).

8. Mistretta, Charles A., Andrew B. Crummy, and Charles M. Strother. 'Digital angiography: a perspective.' Radiology 139.2 (1981): 273-276.

9. Cavallo, A. U. *et al.* Noncontrast Magnetic Resonance Angiography for the Diagnosis of Peripheral Vascular Disease. *Circulation Cardiovasc Imaging* **12,** (2019).

10. Prokop, M. Multislice CT angiography. *Eur J Radiol* **36,** 86–96 (2000).

11. Nederkoorn, P. J., Graaf, Y. van der & Hunink, M. G. M. Duplex Ultrasound and Magnetic Resonance Angiography Compared With Digital Subtraction Angiography in Carotid Artery Stenosis. *Stroke J Am Hear Assoc* **34,** 1324–1332 (2003).

12. Carli, M. F. D. *et al.* Relationship between CT coronary angiography and stress perfusion imaging in patients with suspected ischemic heart disease assessed by integrated PET-CT imaging. *J Nucl Cardiol* **14,** 799–809 (2007).

13. Markl, M., Frydrychowicz, A., Kozerke, S., Hope, M. & Wieben, O. 4D flow MRI. *J Magn Reson Imaging* **36,** 1015–1036 (2012).

14. Shpilfoygel, S., Close, R., Valentino, D. & Duckwiler, G. X-ray videodensitometric methods for blood flow and velocity measurement: A critical review of literature. *Med Phys* **27,** 2008–2023 (2008).

15. Vannier MW. Digital imaging, image processing, and three-dimensional computer graphics for radiology. Curr Opin Radiol. 1992;4(5):1-10.

16. Rubin, G. D. & Rofsky, N. M. *CT and MR Angiography Comprehensive Vascular Assessment*. (2009).

17. Carson Hoffman, Sarvesh Periyasamy, Rafael Medero, Paul F. Laeseke. Angular Dependence of 2D DSA Velocity Quantification in a Carotid Artery Bifurcation Phantom. CIRSE, Barcelona.2019.

18. E Meram, C Hoffman, S Periyasamy, M Speidel, P Laeseke. Assessment of Flow in the Iliac Arteries Using a Quantitative Angiography Technique based on Time-Resolved 2D Digital Subtraction Angiography. SIR, Seattle; 2020.

19. Carson Hoffman, Sarvesh Periyasamy, Yijing Wu, Michael Speidel, Paul Laeseke. Quantitative 2D DSA: A Novel Method for Determining Treatment Endpoints during Transarterial Embolization. RSNA, Chicago; 2019.

20. Carson Hoffman, Ece Meram, Paul Laeseke, Oliver Wieben. 4D Flow MRI: APreliminary Analysis of Changes in Arterial Flow During Liver Embolization In Swine. ISMRM Annual Scientific Meeting Paris. 2018;4744.

21. S Periyasamy, C Hoffman, G Schefelker, M Speidel, O Ozkan, P Laeseke. A Quantitative Angiography Technique Using Time-Resolved 2D-DSA for Determining Treatment Endpoints During Partial Splenic Embolization. SIR, Seattle; 2020.

22. Carson A. Hoffman, Ece Meram , Sarvesh Periyasamy , Paul Laeseke, Oliver Wieben. 4D Flow MRI and Doppler Wire Arterial Flow Analysis Pre-/Post- Liver Embolization in Swine. Society of Magnetic Resonance Angiography, Nantes;2019.

23. Grant Roberts, Kevin Johnson, Carson Hoffman, Laura Eisenmenger, Oliver Wieben. Automating Background Phase Correction in Cranial 4D Flow MRI. Society of Magnetic Resonance Angiography, Nantes;2019.

24. Carson A. Hoffman, Grant Roberts, Sara Berman, Laura Eisenmenger, Oliver Wieben. Towards automated cranial 4D flow analysis. Society of Magnetic Resonance Angiography, Nantes;2019.

25. Carson A. Hoffman, Sylvana García-Rodríguez, Alejandro Roldán-Alzate, E. Jason Abel,Oliver Wieben, and Christopher J. Francois. 4D Flow Analysis of Renal Flow Changes due to Kidney Cancer. Gordon Research Conference: In Vivo Magnetic Resonance, Andover.2016.

26. Carson A. Hoffman, E Jason Abel, Oliver Wieben, Christopher J. Francois. Preoperative 4D Flow Analysis of Renal Cell Carcinoma. Gordon Research Conference: In Vivo Magnetic Resonance, Andover.2018.

27. Carson A. Hoffman, Sylvana García-Rodríguez, Alejandro Roldán-Alzate, E. Jason Abel,Oliver Wieben, and Christopher J. Francois. 4D Flow Analysis of Renal Flow Changes due to Kidney Cancer. Society of Magnetic Resonance Angiography,Chicago.2016.

28. Carson A. Hoffman, E Jason Abel, Oliver Wieben, Christopher J. Francois. Preoperative 4D Flow Analysis of Renal Cell Carcinoma. Society of Magnetic Resonance Angiography, Glasgow;2018.

29. Bushberg, J. T., Seibert, J. A., Leidholdt, E. M. & Boone, J. M. *The Essential Physics of Medical Imaging*. **3rd Edition,** (2012).

30. Haacke, E. M., Brown, R. W., Thompson, M. R. & Venkatesan, R. *Magnetic Resonance Imaging - Physical Principles and Sequence Design*. (1999).

31. Yim, P. J. *Vascular Hemodynamics: Bioengineering and Clinical Perspectives*. (2008).

32. McRobbie, D. W., Moore, E. A., Graves, M. J. & Prince, M. R. *MRI from Picture to Proton*. (2017).

33. Knoll, G. F. *Radiation Detection and Measurements*. **3rd Edition,** (2010).

34. Wright, G. A. Magnetic resonance imaging. *Ieee Signal Proc Mag* **14,** 56–66 (2020).

35. Botden P. Modern trends in diagnostic radiologic instrumentation. In: Moseley R, Rust J, eds. The reduction of patient dose by diagnostic instrumentation. Springfield, IL: Charles C Thomas, 1964: 15.

36. Hendee WR. Medical radiation physics, 2nd ed. Chicago: Year Book Medical Publishers, 1979.

37. Keller, P. J. *et al.* MR Angiography With Two-Dimensional Acquisition and Three-Dimensional Display. Work in Progress. *Radiology* 527–32 (2011). doi:10.1148/radiology.173.2.2798885

38. Prince, M. R., Yucel, E. K., Kaufman, J. A., Harrison, D. C. & Geller, S. C. Dynamic gadolinium-enhanced three-dimensional abdominal MR arteriography. *J Magn Reson Imaging* **3,** 877–881 (1993).

39. R.Moran, P. A flow velocity zeugmatographic interlace for NMR imaging in humans. *Magnetic Resonance Imaging* **1,** 197–203 (2004).

40. Dumoulin, C. L. & JR, H. R. H. Magnetic Resonance Angiography. *Radiology* 717–720 (2012). doi:10.1148/radiology.161.3.3786721

41. Contur, T. E. & Robinson, B. H. Analysis of encoding efficiency in MR imaging of velocity magnitude and direction. *Magnet Reson Med* **25,** 233–247 (1992).

42. Glover, G. H. & Pauly, J. M. Projection Reconstruction Techniques for Reduction of Motion Effects in MRI. *MRM* **28,** 275–289 (1992).

43. Mezrich, R. A perspective on K-space. *Radiology* 297–315 (2005). doi:10.1148/radiology.195.2.7724743

44. Dyverfeldt, P. *et al.* 4D flow cardiovascular magnetic resonance consensus statement. *J Cardiov Magn Reson* **17,** 72 (2015).

45. Johnson, K. & Markl, M. Improved SNR in phase contrast velocimetry with five-point balanced flow encoding. *Magnet Reson Med* **63,** 349–355 (2010).

46. Pelc, N. J., Bernstein, M. A., Shimakawa, A. & Glover, G. H. Encoding strategies for three-direction phase-contrast MR imaging of flow. *J Magn Reson Imaging* **1,** 405–413 (1991).

47. Griswold, M. A., Jakob, P. M., Nittka, M., Goldfarb, J. W. & Haase, A. Partially Parallel Imaging With Localized Sensitivities (PILS). *MRM* **44,** 602–609 (2000).

48. Lustig, M., Donoho, D. & Pauly, J. M. Sparse MRI: The application of compressed sensing for rapid MR imaging. *Magnet Reson Med* **58,** 1182–1195 (2007).

49. Markl, M. & Hennig, J. Phase contrast MRI with improved temporal resolution by view sharing: k-space related velocity mapping properties. *Magn Reson Imaging* **19,** 669–676 (2001).

50. Gu, T. *et al.* PC VIPR: A High-Speed 3D Phase-Contrast Method for Flow Quantification and HighResolution Angiography. *AJNR* **26 no. 4,** 743–749 (2005).

51. Johnson, K. M. *et al.* Improved 3D phase contrast MRI with off-resonance corrected dual echo VIPR. *Magnet Reson Med* **60,** 1329–1336 (2008).

52. Crummy, A. B. *et al.* Digital subtraction angiography: current status and use of intra-arterial injection. *Radiology* **145,** (1982).

53. Crummy, A. B., Strother, C. M. & Mistretta, C. A. The History of Digital Subtraction Angiography. *J Vasc Interv Radiol* **29,** 1138–1141 (2018).

54. Strijen, M. J. van *et al.* Evaluation of a Noise Reduction Imaging Technology in Iliac Digital Subtraction Angiography: Noninferior Clinical Image Quality with Lower Patient and Scatter Dose. *J Vasc Interv Radiol* **26,** 642-650.e1 (2015).

55. Meijering, E. H. W., Niessen, W. J. & Viegever, M. A. Retrospective motion correction in digital subtraction angiography: a review. *Ieee T Med Imaging* **18,** 2–21 (2020).

56. Buzug, T. M., Weese, J., Fassnacht, C. & Lorenz, C. Visualization in Biomedical Computing, 4th International Conference, VBC'96 Hamburg, Germamy, September 22–25, 1996 Proceedings. 235–240 (2006). doi:10.1007/bfb0046959

57. Davis, B. *et al.* 4D Digital Subtraction Angiography: Implementation and Demonstration of Feasibility. *Am J Neuroradiol* **34,** 1914–1921 (2013).

58. Shakur, S. F. *et al.* Validation of cerebral arteriovenous malformation hemodynamics assessed by DSA using quantitative magnetic resonance angiography: preliminary study. *J Neurointerv Surg* **10,** 156 (2018).

59. Strother, C. M. *et al.* Parametric Color Coding of Digital Subtraction Angiography. *Am J Neuroradiol* **31,** 919–924 (2010).

60. Murayama, Y., Massoud, T. F. & Viñuela, F. Transvenous Hemodynamic Assessment of Experimental Arteriovenous Malformations: Doppler Guidewire Monitoring of Embolotherapy in a Swine Model. *Stroke* **27,** 1365–1372 (1996).

61. Frydrychowicz, A., François, C. J. & Turski, P. A. Four-dimensional phase contrast magnetic resonance angiography: Potential clinical applications. *Eur J Radiol* **80,** 24–35 (2011).

62. Lo, E. H. A theoretical analysis of hemodynamic and biomechanical alterations in intracranial AVMs after radiosurgery. *Int J Radiat Oncol Biology Phys* **27,** 353–361 (1993).

63. Shaughnessy, G., Schafer, S., Speidel, M. A., Strother, C. M. & Mistretta, C. A. Measuring blood velocity using 4D-DSA: A feasibility study. *Med Phys* **45,** 4510–4518 (2018).

64. Wu, Y. *et al.* Quantification of Blood Velocity with 4D Digital Subtraction Angiography Using the Shifted Least-Squares Method. *Am J Neuroradiol* **39,** 1871–1877 (2018).

65. Hentschke, C. M., Serowy, S., Janiga, G., Rose, G. & Tönnies, K. D. Estimating blood flow velocity in angiographic image data. *SPIE International Society of Optical Engineering* 79640Y-79640Y–9 (2011). doi:10.1117/12.878019

66. Lee, C. S., Nagy, P. G., Weaver, S. J. & Newman-Toker, D. E. Cognitive and system factors contributing to diagnostic errors in radiology. *Am J Roentgenol* **201,** 611–617 (2013).

67. Koelemay, M. J. W. *et al.* Interobserver Variation in Interpretation of Arteriography and Management of Severe Lower Leg Arterial Disease. *Eur J Vasc Endovasc* **21,** 417–422 (2001).

68. Paul, J. F. *et al.* Interobserver variability in the interpretation of renal digital subtraction angiography. *Am J Roentgenol* **173,** 1285–1288 (1999).

69. Vries, A. R. de, Engels, P. H., Overtoom, T. T., Saltzherr, T. P. & Geyskes, B. G. Interobserver variability in assessing renal artery stenosis by digital subtraction angiography. *Diagn Imag Clin Med* **53,** 277–81 (1984).

70. Lewandowski, R. J. *et al.* A Comparison of Chemoembolization Endpoints Using Angiographic versus Transcatheter Intraarterial Perfusion/MR Imaging Monitoring. *J Vasc Interv Radiol* **18,** 1249–1257 (2007).

71. Gardiner, G. A. *et al.* Angiographic Assessment of Initial Balloon Angioplasty Results. *J Vasc Interv Radiol* **15,** 1081–1087 (2004).

72. Meram, E. *et al.* Quantitative 4D-Digital Subtraction Angiography to Assess Changes in Hepatic Arterial Flow during Transarterial Embolization: A Feasibility Study in a Swine Model. *J Vasc Interv Radiol* (2019). doi:10.1016/j.jvir.2019.01.018

73. Motoyama, D. *et al.* Four-dimensional phase-contrast vastly undersampled isotropic projection reconstruction (4D PC-VIPR) MR evaluation of the renal arteries in transplant recipients: Preliminary results. *J Magn Reson Imaging* **46,** 595–603 (2017).

74. Nett, E. J. *et al.* Four-dimensional phase contrast MRI With accelerated dual velocity encoding. *J Magn Reson Imaging* **35,** spcone-spcone (2012).

75. Frydrychowicz, A. *et al.* Four-dimensional velocity mapping of the hepatic and splanchnic vasculature with radial sampling at 3 tesla: A feasibility study in portal hypertension. *J Magn Reson Imaging* **34,** spcone-spcone (2011).

76. Wang, D. *et al.* Quantitative 4D transcatheter intraarterial perfusion MRI for monitoring chemoembolization of hepatocellular carcinoma. *J Magn Reson Imaging* **31,** 1106–1116 (2010).

77. Lin, E. Y. *et al.* Three-Dimensional Quantitative Color-Coding Analysis of Hepatic Arterial Flow Change during Chemoembolization of Hepatocellular Carcinoma. *J Vasc Interv Radiol* **29,** 1362–1368 (2018).

78. Iwakoshi, S. *et al.* Complex combination of femoropopliteal occlusive disease and arteriovenous fistula treated using color-coded digital subtraction angiography. *J Vasc Surg Cases Innovative Techniques* **5,** 264–268 (2019).

79. Ionita CN, et al. "Effect of injection technique on temporal parametric imaging derived from digital subtraction angiography in patient specific phantoms." Proc SPIE Int Soc Opt Eng. 2014;13(9038).90380L.

80. Kennedy, A. S., Kleinstreuer, C., Basciano, C. A. & Dezarn, W. A. Computer Modeling of Yttrium-90–Microsphere Transport in the Hepatic Arterial Tree to Improve Clinical Outcomes. *Int J Radiat Oncol Biology Phys* **76,** 631–637 (2010).

81. Nakamura, T. *et al.* Quantitative Measurement of Abdominal Arterial Blood Flow Using Image-Directed Doppler Ultrasonography: Superior Mesenteric, Splenic, and Common Hepatic Arterial Blood Flow in Normal Adults. *J Clin Ultrasound* **4,** 261–268 (1989).

82. Zhang, X. *et al.* Objective Assessment of Transcatheter Arterial Chemoembolization Angiographic Endpoints: Preliminary Study of Quantitative Digital Subtraction Angiography. *J Vasc Interv Radiol* **24,** 667–671 (2013).

83. Hinrichs, J. B. *et al.* Evaluation of a novel 2D perfusion angiography technique independent of pump injections for assessment of interventional treatment of peripheral vascular disease. *Int J Cardiovasc Imaging* **33,** 295–301 (2016).

84. Wang, J. *et al.* Quantitative assessment of angiographic perfusion reduction using color-coded digital subtraction angiography during transarterial chemoembolization. *Abdom Radiol* **41,** 545–552 (2016).

85. Yang, J. D. *et al.* A global view of hepatocellular carcinoma: trends, risk, prevention and management. *Nat Rev Gastroentero* **16,** 589–604 (2019).

86. Statistics adapted from the American Cancer Society's (ACS) publication, Cancer Facts & Figures 2020 and the ACS website (January 2020).

87. International Agency for Research on Cancer. Liver. World Health Organization. Accessed June 13 2020, https://gco.iarc.fr/today/data/factsheets/cancers/11-Liver-fact-sheet.pdf.

88. Marrero, J. A. *et al.* Diagnosis, Staging, and Management of Hepatocellular Carcinoma: 2018 Practice Guidance by the American Association for the Study of Liver Diseases. *Hepatology* **68,** 723–750 (2018).

89. Murata, S. *et al.* Interventional treatment for unresectable hepatocellular carcinoma. *World J Gastroentero* **20,** 13453–13465 (2014).

90. Llovet, J. M. *et al.* Arterial embolisation or chemoembolisation versus symptomatic treatment in patients with unresectable hepatocellular carcinoma: a randomised controlled trial. *Lancet* **359,** 1734–1739 (2002).

91. Lo, C. *et al.* Randomized controlled trial of transarterial lipiodol chemoembolization for unresectable hepatocellular carcinoma. *Hepatology* **35,** 1164–1171 (2002).

92. Manini, M. A. *et al.* Transarterial chemoembolization with drug-eluting beads is effective for the maintenance of the Milan-in status in patients with a small hepatocellular carcinoma. *Liver Transplant* **21,** 1259–1269 (2015).

93. Bouchard-Fortier, A., Lapointe, R., Perreault, P., Bouchard, L. & Pomier-Layrargues, G. Transcatheter Arterial Chemoembolization of Hepatocellular Carcinoma as a Bridge to Liver Transplantation: A Retrospective Study. *Int J Hepatology* **2011,** 974514 (2011).

94. Geschwind, J.-F. H. *et al.* Transcatheter Arterial Chemoembolization of Liver Tumors: Effects of Embolization Protocol on Injectable Volume of Chemotherapy and Subsequent Arterial Patency. *Cardiovasc Inter Rad* **26,** 111–117 (2003).

95. Rhee, T. K. *et al.* Effect of Transcatheter Arterial Embolization on Levels of Hypoxia-inducible Factor-1α in Rabbit VX2 Liver Tumors. *J Vasc Interv Radiol* **18,** 639–645 (2007).

96. Jin, B. *et al.* Chemoembolization Endpoints: Effect on Survival Among Patients With Hepatocellular Carcinoma. *Am J Roentgenol* **196,** 919–928 (2011).

97. Hennedige, T. & Venkatesh, S. K. Imaging of hepatocellular carcinoma: diagnosis, staging and treatment monitoring. *Cancer Imaging* **12,** 530–547 (2013).

98. Gaba, R. C. *et al.* Four-dimensional Transcatheter Intraarterial Perfusion MR Imaging for Monitoring Chemoembolization of Hepatocellular Carcinoma: Preliminary Results. *J Vasc Interv Radiol* **19,** 1589–1595 (2008).

99. Lin, Y.-Y. *et al.* Quantitative Real-Time Fluoroscopy Analysis on Measurement of the Hepatic Arterial Flow During Transcatheter Arterial Chemoembolization of Hepatocellular Carcinoma: Comparison with Quantitative Digital Subtraction Angiography Analysis. *Cardiovasc Inter Rad* **39,** 1557–1563 (2016).

100. Chen, C.-W. *et al.* Assessment of small hepatocellular carcinoma. *Medicine* **97,** e13392 (2018).

101. Hoffman C, Periyasamy S, Medero R, Laeseke P. Angular dependence of 2D DSA velocity quantification in a carotid artery bifurcation phantom. Poster session presented at: Cardiovascular and

Interventional Radiological Society of Europe CIRSE Annual Congress; 2019 Sep 9-11; Barcelona, Spain. 2019.

102. Hoffman C, Periyasamy S, Wu Y, Speidel M, Laeseke P. Quantitative 2D DSA: Metrics for determining treatment endpoints in TAE. Oral presentation at: Radiological Society of North America, RSNA Annual Meeting; 2019 Dec 1-6; Chicago, IL. 2019.

103. Periyasamy S, Hoffman C, Schefelker G, Speidel M, Laeseke P. A Quantitative 2D-DSA Method for Characterizing Changes in Hepatic Perfusion During Transarterial Embolization. Poster session presented at: Society of Interventional Oncology, SIO2020; 2020 Jan 30-Feb 3; New Orleans, LA. 2020.

104. Marquez, H. P. *et al.* Computed tomography perfusion imaging for monitoring transarterial chemoembolization of hepatocellular carcinoma. *Eur J Radiol* **91,** 160–167 (2017).

105. Taouli, B. *et al.* Hepatocellular Carcinoma: Perfusion Quantification With Dynamic Contrast-Enhanced MRI. *Am J Roentgenol* **201,** 795–800 (2013).

106. Futami, K. *et al.* Inflow Jet Patterns of Unruptured Cerebral Aneurysms Based on the Flow Velocity in the Parent Artery: Evaluation Using 4D Flow MRI. *Am J Neuroradiol* **37,** 1318–1323 (2016).

107. Schnell, S. *et al.* Three-dimensional hemodynamics in intracranial aneurysms: influence of size and morphology. *J Magn Reson Imaging* **39,** 120–131 (2014).

108. Ansari, S. A. *et al.* Intracranial 4D Flow MRI: Toward Individualized Assessment of Arteriovenous Malformation Hemodynamics and Treatment-Induced Changes. *Am J Neuroradiol* **34,** 1922–1928 (2013).

109. Edjlali, M. *et al.* MR Selective Flow-Tracking Cartography: A Postprocessing Procedure Applied to Four-dimensional Flow MR Imaging for Complete Characterization of Cranial Dural Arteriovenous Fistulas. *Radiology* **270,** 261–268 (2014).

110. Clark, L. R. *et al.* Association of Cardiovascular and Alzheimer's Disease Risk Factors with Intracranial Arterial Blood Flow in Whites and African Americans. *J Alzheimer's Dis* **72,** 919–929 (2019).

111. Schrauben, E. M. *et al.* Four-dimensional flow magnetic resonance imaging and ultrasound assessment of cerebrospinal venous flow in multiple sclerosis patients and controls. *J Cereb Blood Flow Metabolism* **37,** 1483–1493 (2016).

112. Kellawan, J. M., Harrell, J. W., Roldan-Alzate, A., Wieben, O. & Schrage, W. G. Regional hypoxic cerebral vasodilation facilitated by diameter changes primarily in anterior versus posterior circulation. *J Cereb Blood Flow Metabolism* **37,** 2025–2034 (2016).

113. Garcia, J., Barker, A. J. & Markl, M. The Role of Imaging of Flow Patterns by 4D Flow MRI in Aortic Stenosis. *Jacc Cardiovasc Imaging* **12,** 252–266 (2019).

114. Schrauben, E. M., Anderson, A. G., Johnson, K. M. & Wieben, O. Respiratory-induced venous blood flow effects using flexible retrospective double-gating. *J Magn Reson Imaging* **42,** 211–216 (2015).

115. Ma, L. E. *et al.* Aortic 4D flow MRI in 2 minutes using compressed sensing, respiratory controlled adaptive k-space reordering, and inline reconstruction. *Magnet Reson Med* **81,** 3675–3690 (2019).

116. Schrauben, E. *et al.* Fast 4D flow MRI intracranial segmentation and quantification in tortuous arteries. *J Magn Reson Imaging* **42,** 1458–1464 (2015).

117. Dunås, T., Holmgren, M., Wåhlin, A., Malm, J. & Eklund, A. Accuracy of blood flow assessment in cerebral arteries with 4D flow MRI: Evaluation with three segmentation methods. *J Magn Reson Imaging* **50,** 511–518 (2019).

118. Bernstein, M. A. *et al.* Concomitant gradient terms in phase contrast MR: analysis and correction. Magn Reson Med 1998;39(2):300-308. *MRM* **39,** 300.

119. Loecher, M., Schrauben, E., Johnson, K. M. & Wieben, O. Phase unwrapping in 4D MR flow with a 4D single-step laplacian algorithm. *J Magn Reson Imaging* **43,** 833–842 (2016).

120. G, R., K, J., C, H., L, E. & O., W. Automating Background Phase Correction in Cranial 4D Flow MRI. *SMRA* 88–89 (2019).

121. PG, W., GB, C., MB, S., G, W. & GM, P. Semiautomated method for noise reduction and background phase error correction in MR phase velocity data. **3,** 521 (1993).

122. Bernstein, M. A. & Ikezaki, Y. Comparison of phase-difference and complex-difference processing in phase-contrast MR angiography. *JMRI* **1,** 725 (1991).

123. C., L. T., L., K. R. & N., C. C. Building Skeleton Models via 3-D Medial Surface Axis Thinning Algorithms. *CVGIP* **56,** 462–478 (1994).

124. Nelson, T. R. & Pretorius, D. H. The Doppler signal: where does it come from and what does it mean? *AJR* **151,** 439–447 (1988).

125. E., T. M., Bude, R. O. & Platt, J. F. The Resistive Index in Renal Doppler Sonography: Where Do We Stand? *AJR* **180,** 885–892 (2003).

126. Hartigan, J. A. & Wong, M. A. A K-Means Clustering Algorithm. *Applied Statistics* **28,** 100–108 (n.d.).

127. Altman, D. G. & Bland, J. M. Measurement in Medicine: The Analysis of Method Comparison Studies. *The Statistician* **32,** 307–317 (1983).

128. Dunås, T. *et al.* A Stereotactic Probabilistic Atlas for the Major Cerebral Arteries. *Neuroinformatics* **15,** 101–110 (2017).

129. Rivera-Rivera, L. A. *et al.* 4D flow MRI for intracranial hemodynamics assessment in Alzheimer's disease. *J Cereb Blood Flow Metabolism* **36,** 1718–1730 (2015).

130. Turski, P. *et al.* Neurovascular 4DFlow MRI (Phase Contrast MRA): emerging clinical applications. *Neurovascular Imaging* **2,** 8 (2016).

131. Schnell, S., Wu, C. & Ansari, S. A. 4D MRI flow examinations in cerebral and extracerebral vessels. Ready for clinical routine? *Curr Opin Neurol* **29,** 419–428 (2017).

132. Landis, S. H., Murray, T., Bolden, S. & Wingo, P. A. Cancer statistics, 1999. *Ca Cancer J Clin* **49,** 8–31 (1999).

133. Cancer Facts & Figures 2019. American Cancer Society. Available at https://www.cancer.org/content/dam/cancer-org/research/cancer-facts-and-statistics/annual-cancer-facts-and-figures/2019/cancer-facts-and-figures-2019.pdf. Accessed: February 19, 2019.

134. Cancer of the Kidney and Renal Pelvis - Cancer Stat Facts. SEER. https://seer.cancer.gov/statfacts/html/kidrp.html. Published 2020. Accessed June 6, 2020.

135. Siegel, R. L., Miller, K. D. & Jemal, A. Cancer statistics, 2018. *Ca Cancer J Clin* **68,** 7–30 (2018).

136. Leslie, J. A., Prihoda, T. & Thompson, I. M. Serendipitous renal cell carcinoma in the post-CT era: continued evidence in improved outcomes. *Urologic Oncol Seminars Orig Investigations* **21,** 39–44 (2003).

137. Greenlee, R. T., Hill-Harmon, M. B., Murray, T. & Thun, M. Cancer Statistics, 2001. *Ca Cancer J Clin* **51,** 15–36 (2001).

138. Kantarjian, H., Koller, C. A. & Wolff, R. A. *The MD Anderson manual of medical oncology*. (2011).

139. Filipas, D. *et al.* Nephron-sparing surgery of renal cell carcinoma with a normal opposite kidney: long-term outcome in 180 patients. *Urology* **56,** 387–392 (2000).

140. Delakas, D. *et al.* Nephron-sparing surgery for localized renal cell carcinoma with a normal contralateral kidney: a European three-center experience. *Urology* **60,** 998–1002 (2002).

141. Nieder, A. M. & Taneja, S. S. The role of partial nephrectomy for renal cell carcinoma in contemporary practice. *The Urologic Clinics of North America* **3,** 529–542 (2007).

142. Uzzo, R. G. & Novick, A. C. NEPHRON SPARING SURGERY FOR RENAL TUMORS: INDICATIONS, TECHNIQUES AND OUTCOMES. *Journal of Urology* (2007). doi:https://doi.org/10.1016/S0022-5347(05)66066-1

143. Ljungberg, B. *et al.* EAU Guidelines on Renal Cell Carcinoma: 2014 Update. *Eur Urol* **67,** 913–924 (2015).

144. Guzzo, T. J., Pierorazio, P. M., Schaeffer, E. M., Fishman, E. K. & Allaf, M. E. The Accuracy of Multidetector Computerized Tomography for Evaluating Tumor Thrombus in Patients With Renal Cell Carcinoma. *J Urology* **181,** 486–491 (2009).

145. Gabr, A. H., Gdor, Y., Roberts, W. W. & Jr, J. S. W. Radiographic surveillance of minimally and moderately complex renal cysts. *Bju Int* **103,** 1116–1119 (2009).

146. Beer, A. J. *et al.* Comparison of 16-MDCT and MRI for Characterization of Kidney Lesions. *Am J Roentgenol* **186,** 1639–1650 (2006).

147. Feng, Q. *et al.* Renal clear cell carcinoma: diffusion tensor imaging diagnostic accuracy and correlations with clinical and histopathological factors. *Clin Radiol* **72,** 560–564 (2017).

148. Nery, F., Gordon, I. & Thomas, D. L. Non-Invasive Renal Perfusion Imaging Using Arterial Spin Labeling MRI: Challenges and Opportunities. *Diagnostics* **8,** 2 (2018).

149. Chiappini, B. *et al.* Cavoatrial tumor thrombus: Single-stage surgical approach with profound hypothermia and circulatory arrest, including a review of the literature. *J Thorac Cardiovasc Surg* **124,** 684–688 (2002).

150. Sweeney, P. *et al.* Surgical management of renal cell carcinoma associated with complex inferior vena caval thrombi. *Urologic Oncol Seminars Orig Investigations* **21,** 327–333 (2003).

151. Mir, M. C. *et al.* Decline in Renal Function after Partial Nephrectomy: Etiology and Prevention. *J Urology* **193,** 1889–1898 (2015).

152. Sundaram B. 'Kidney Cancer Stages, Diagnosis and Treatment' http://drbalauro.com/kidney-cancer.html Visited: June 2020.

153. Welch, B. L. The Generalization of `Student's' Problem when Several Different Population Variances are Involved. *Oxford Journals* **1,** 28–35 (2001).

154. Satterthwaite, F. E. An Approximate Distribution of Estimates of Variance Components. *Biometrics Bulletin* **2,** 110–114.

155. Krabbe, L.-M., Bagrodia, A., Margulis, V. & Wood, C. Surgical Management of Renal Cell Carcinoma. *Semin Intervent Rad* **31,** 027–032 (2014).

156. Tsui, K. H., Ophoven, A. van, Shvarts, O. & Belldegrun, A. Nephron-sparing surgery for renal cell carcinoma. *Rev Urology* **1,** 216–25 (1999).

157. Psutka, S. P. & Leibovich, B. C. Management of inferior vena cava tumor thrombus in locally advanced renal cell carcinoma. *Ther Adv Urology* **7,** 216–229 (2015).

158. Slaton, J. W. *et al.* Nephrectomy and vena caval thrombectomy in patients with metastatic renal cell carcinoma. *Urology* **50,** 673–677 (1997).

159. Woodruff, D. Y. *et al.* The perioperative management of an inferior vena caval tumor thrombus in patients with renal cell carcinoma. *Urologic Oncol Seminars Orig Investigations* **31,** 517–521 (2013).

160. SOHAIB, S. A. A. *et al.* ASSESSMENT OF TUMOR INVASION OF THE VENA CAVAL WALL IN RENAL CELL CARCINOMA CASES BY MAGNETIC RESONANCE IMAGING. *J Urology* **167,** 1271–1275 (2002).

161. Manassero, F. *et al.* Renal cell carcinoma with caval involvement: Contemporary strategies of surgical treatment. *Urologic Oncol Seminars Orig Investigations* **29,** 745–750 (2011).

162. Adams, L. C. *et al.* Renal cell carcinoma with venous extension: prediction of inferior vena cava wall invasion by MRI. *Cancer Imaging* **18,** 17 (2018).

163. Stevens, L. A., Coresh, J., Greene, T. & Levey, A. S. Assessing Kidney Function — Measured and Estimated Glomerular Filtration Rate. *New Engl J Med* **354,** 2473–2483 (2006).

164. Levey, A. S. *et al.* A New Equation to Estimate Glomerular Filtration Rate. *Ann Intern Med* **150,** 604 (2009).

165. Kumar, R. *et al.* Role of FDG PET-CT in recurrent renal cell carcinoma. *Nucl Med Commun* **31,** 844–850 (2010).

166. Cutajar, M. *et al.* Comparison of ASL and DCE MRI for the non-invasive measurement of renal blood flow: quantification and reproducibility. *Eur Radiol* **24,** 1300–1308 (2014).

167. Motzer RJ, Jonasch E, Agarwal N, et al. Kidney Cancer, Version 2.2017, NCCN Clinical Practice Guidelines in Oncology. J Natl Compr Canc Netw 2017;15:804-34.

168. Donat SM, Diaz M, Bishoff JT, et al. Follow-up for Clinically Localized Renal Neoplasms: AUA Guideline. J Urol 2013;190:407-16.

169. Williamson TJ, Pearson JR, Ischia J, Bolton DM, Lawrentschuk N. Guideline of guidelines: follow-up after nephrectomy for renal cell carcinoma. BJU Int 2016;117:555-62.

170. Salgado R, Mulkens T, Ozsarlak O, De Schepper AM, Parizel PA. CT angiography: basic principles and post-processing applications. JBR-BTR. 2003;86(6):336-340.

171. Carson A. Hoffman, Ece Meram, Oliver Wieben, Paul Laeseke. Motion-correction algorithms for 2D-DSA based regional hepatic perfusion mapping. CIRSE, Barcelona.2019.

172. Carson A. Hoffman, Ece Meram, Oliver Wieben, Paul Laeseke. Regional hepatic 2D DSA perfusion mapping pre and post transarterial embolization. CIRSE Barcelona.2019.